

**MEASUREMENT OF THE ANTIQUARK FLAVOR
ASYMMETRY IN THE NUCLEON SEA**

by

RUSTY SHANE TOWELL, B.S.

DISSERTATION

Presented to the Faculty of the Graduate School of

The University of Texas at Austin

in Partial Fulfillment

of the Requirements

for the Degree of

DOCTOR OF PHILOSOPHY

THE UNIVERSITY OF TEXAS AT AUSTIN

December 2018

Copyright
by
Rusty Shane Towell
2018

**MEASUREMENT OF THE ANTIQUARK FLAVOR
ASYMMETRY IN THE NUCLEON SEA**

APPROVED BY
DISSERTATION COMMITTEE:

Supervisor: _____

Supervisor: _____

To my wife Amy,
my children Ramsey, Marshall, Cecily, Ensley, and Travis,
and my parents Delbert and Helen.

Acknowledgements

This dissertation would not have been possible without the efforts of the FNAL E866/NuSea collaboration. I have been blessed to be a member of this talented, hard working, and fun collaboration. I thank each of you for your contribution to the experiment, my education, and this dissertation. I hope I have the opportunity to work with each of you again.

The FNAL E866/NuSea Collaboration

T.C. Awes, M.E. Beddo, C.N. Brown, J.D. Bush, T.A. Carey,
T.H. Chang, W.E. Cooper, C.A. Gagliardi, G.T. Garvey, D.F. Geesaman,
E.A. Hawker, X.C. He, L.D. Isenhower, S.B. Kaufman, D.M. Kaplan,
P.N. Kirk, D.D. Koetke, G. Kyle, D.M. Lee, W.M. Lee, M.J. Leitch,
N. Makins, P.L. McGaughey, J.M. Moss, B.A. Mueller, P.M. Nord,
B.K. Park, V. Papavassiliou, J.C. Peng, G. Petitt, P.E. Reimer,
M.E. Sadler, J. Selden, P.W. Stankus, W.E. Sondheim, T.N. Thompson,
R.S. Towell, R.E. Tribble, M.A. Vasiliev, Y.C. Wang, Z.F. Wang,
J.C. Webb, J.L. Willis, D.K. Wise, and G.R. Young

Many members of this collaboration have gone above and beyond what could reasonably be expected of them. For this they deserve many special thanks.

Mike Sadler and Donald Isenhower have been teaching me about physics and life for over twelve years. Thank you for everything you have taught me from basic physics to how to exchange money in Russia to how to be a friend to thermodynamics (I still can't believe you gave me a B) to how to finish graduate school. I know you have more to teach me, I hope you don't stop.

Gerry Garvey, Pat McGaughey, and Mike Leitch have each done any excellent job as spokesman for E866. They have not only over seen the success of the experiment, but the success of the graduate students. Thank you for the time you have spend working with me.

Carl Gagliardi has been an incredible support to me throughout the analysis of the data and the writing of this dissertation. Thank you for watching what I did, correcting me when I was wrong, complimenting me when I was right, and always encouraging me to finish.

Eric, Bill, Ting, and Jason have been wonderful fellow graduate students. Thanks for helping to keep the physics fun. For four summers I worked with Derek. I could not have asked for a better friend. Thanks for being my fellow 'science guy'.

Finally, I must thank Paul Reimer. I can't imagine going through the past three years without his help and friendship. He has help me and taught me so much. Thank you for answering all my dumb questions. Thank you for your hard work to help me finish this dissertation.

In addition to the support I received from the members of this collaboration, I have also been blessed by the support of many friends and family.

For the past ten years I have enjoyed the constant support of my wife. Thank you Amy for supporting my decision to go back to graduate school. Thank you for your patience, love, and encouragement. I could not have done this without you.

For more years than anyone else, my parents have blessed my life. Thank you for teaching me the important things. Thank you for helping me through twenty years of school. I'm finally done.

**MEASUREMENT OF THE ANTIQUARK FLAVOR
ASYMMETRY IN THE NUCLEON SEA**

Publication No. _____

Rusty Shane Towell, Ph.D.
The University of Texas at Austin, 2018

Supervisors: L. Donald Isenhower
Peter J. Riley

A precise measurement of the ratio of Drell-Yan yields from an 800 GeV/c proton beam incident on liquid hydrogen and deuterium targets is reported. Over 370,000 Drell-Yan muon pairs were recorded. From these data, the ratio of anti-down (\bar{d}) to anti-up (\bar{u}) quark distributions in the proton sea is determined over a wide range in Bjorken- x . A strong x dependence is observed in the ratio \bar{d}/\bar{u} . From this result, the integral of $(\bar{d} - \bar{u})$ is evaluated for $0.015 < x < 0.35$ and compared with deep inelastic scattering results. The origin of this asymmetry is probably due to non-perturbative effects such as those contained in pion cloud models. This measurement has instigated new global fits since previous parameterizations of the proton could not accommodate this large asymmetry.

Table of Contents

Acknowledgements	v
Abstract	viii
List of Tables	xi
List of Figures	xiii
Chapter 1. Introduction	1
Chapter 2. Theory and Motivation	4
2.1 Muon Induced Deep Inelastic Scattering	4
2.2 Drell-Yan	10
2.3 Global Fits	15
Chapter 3. Experimental Setup	18
3.1 Beamline and Beam Monitors	19
3.2 Targets	20
3.3 E866 Spectrometer	22
3.4 Data Acquisition System	28
3.4.1 Trigger	32
3.4.2 Readout System	33
Chapter 4. Experimental Procedures	34
4.1 Recommissioning the Spectrometer	34
4.2 Commissioning the New Parts of the Spectrometer	35
4.3 Spectrometer Tune-up with Beam	36
4.4 Standard Data Taking Procedures	37
4.5 Special Data Taking Procedures	38

Chapter 5. Analysis	39
5.1 Data Sets	39
5.2 First Pass	42
5.3 Second Pass	44
5.4 Ntuple Cuts	45
5.5 Randoms Correction	47
5.6 Rate Dependence Correction	49
5.6.1 Functional Form of the Rate Dependence	52
5.6.2 Relation Between the Rate Dependence in the Two Targets	55
5.6.3 Determination of F	59
5.7 Target Composition, Density, and Attenuation	61
5.8 Calculation of $\sigma^{pd}/2\sigma^{pp}$	68
5.9 Systematic Uncertainty in $\sigma^{pd}/2\sigma^{pp}$	73
5.10 Extraction of $\bar{d}(x)/\bar{u}(x)$	79
Chapter 6. Results and Conclusions	88
6.1 E866 Results	88
6.2 Comparison to Other Experiments	94
6.3 Possible Origins of the Nucleon Sea	97
6.3.1 Perturbative Origins	99
6.3.2 Nonperturbative Origins	100
6.4 Future Experiment	105
6.5 Conclusion	105
Bibliography	107
Vita	111

List of Tables

3.1	Information on the drift chambers. Drift cell and aperture sizes are in inches.	28
3.2	Information on hodoscopes. The counter width, aperture sizes, and the center gap size are in inches.	29
3.3	Information on proportional tubes. Drift cell and aperture sizes are in inches.	29
3.4	Drift chamber efficiency in percent.	30
3.5	Typical Hodoscope efficiencies in percent. The Y planes are divided at $y = 0$ and L (R) denotes the left (right) half plane. The X planes are divided at $x = 0$ and U (D) denotes the upper (lower) half plane.	31
5.1	Summary of the data sets. The size of each data set is shown as the number of Drell-Yan events that passed all data cuts rounded to the nearest thousand. All magnet currents are in amperes. The deuterium fill refers to the quality of the deuterium in the target as described in Section 5.7.	41
5.2	Summary of all ntuple cuts.	48
5.3	Size of the randoms correction for each mass setting.	50
5.4	Calculated F values for each station and each mass setting.	60
5.5	Calculated F values for each mass setting obtained by taking a weighted average over all three stations.	60
5.6	Correction to $\sigma^{pd}/2\sigma^{pp}$ due to the rate dependence.	61
5.7	Results of the gas analyses of the second fill of the deuterium target. The results shown are in percent volume.	65
5.8	Best estimate of the composition of the second fill deuterium. The results shown are in percent volume.	66
5.9	Average pressure in psi of each liquid target for each data set.	66
5.10	Density in g/cm^3 for each liquid target and for each data set.	67
5.11	The cross section ratio calculated for each data set of the high mass setting and the final high mass result for each x_2 bin. The uncertainty shown here is the statistical uncertainty.	70

5.12	The cross section ratio calculated for each data set of the intermediate mass setting and the final intermediate mass result for each x_2 bin. The uncertainty shown here is the statistical uncertainty.	71
5.13	The cross section ratio calculated from the low mass setting data for each x_2 bin. The uncertainty shown here is the statistical uncertainty. The average values for kinematic variables is also shown.	71
5.14	The average values for kinematic variables in the high mass data for each x_2 bin. The uncertainty shown here for the cross section ratio is the statistical uncertainty.	72
5.15	The average values for kinematic variables in the intermediate mass data for each x_2 bin. The uncertainty shown here for the cross section ratio is the statistical uncertainty.	72
5.16	The cross section ratio calculated from all data sets for each x_2 bin. The uncertainty shown here is the statistical uncertainty. The average values for kinematic variables is also shown.	76
5.17	Systematic uncertainties in measurement of $\sigma^{pd}/2\sigma^{pp}$	78
5.18	The value of $\bar{d}(x)/\bar{u}(x)$ and $\bar{d}(x) - \bar{u}(x)$ as determined from all data sets for each x_2 bin. The statistical uncertainty is listed first followed by the systematic uncertainty.	82
6.1	$\int(\bar{d}(x) - \bar{u}(x))dx$ evaluated over different x ranges based on three different parameterizations and as measured by E866.	99
6.2	$\int(\bar{d}(x) - \bar{u}(x))dx$ as determined by three experiments. The range of the measurement is shown along with the value of the integral over all x	99

List of Figures

1.1	A simple picture of the proton according to the Parton Model. The proton contains 2 valence up quarks (u), one valence down quark (d), gluons (helix), and the sea of any number of quark antiquark pairs (q and \bar{q}).	3
2.1	Muon induced deep inelastic scattering. In this process the high energy muon scatters off a single quark in the nucleon by exchanging a high energy virtual photon.	5
2.2	The NMC measured ratio F_2^n/F_2^p at $Q^2 = 4 \text{ GeV}^2$. Only the statistical uncertainty is shown.	7
2.3	The difference $F_2^p - F_2^n$ (solid symbols and the scale to the right) and $\int_x^1 (F_2^p - F_2^n) dx/x$ (open symbols and the scale to the left) at $Q^2 = 4 \text{ GeV}^2$ as a function of x . The extrapolated integral result, S_G is indicated by the bar. The traditional Gottfried Sum Rule result, GSR is also shown.	8
2.4	The leading order Drell-Yan process.	11
2.5	An old parameterization of the proton by MRS assuming a symmetric sea [17]. These parton distribution functions are shown for $Q^2 = 54 \text{ GeV}^2$	16
2.6	An old parameterization of the proton published by CTEQ [15] prior to FNAL E866/NuSea. These parton distribution functions are shown for $Q^2 = 54 \text{ GeV}^2$	17
3.1	One of the three identical E866 target flasks.	21
3.2	The FNAL E866/NuSea Spectrometer	22
3.3	The beam dump and absorber wall inside the aperture of SM12. The beam dump is not shown in the plan view.	24
5.1	The dimuon mass distributions for the three different mass settings. The inset figures are the same spectra shown on a linear scale.	40
5.2	The rate dependence problem shown here for the low mass data. The yield of Drell-Yan events per unit of beam intensity is shown versus the beam intensity for both the hydrogen and deuterium events.	51

5.3	Monte Carlo study of the rate dependence. The horizontal error bars indicate where the data were divided into bins of beam intensity. These points are plotted at the average beam intensity within the bin. The highest and lowest points in beam intensity do not have horizontal error bars because there were no data at these beam intensities.	53
5.4	Number of deuterium (left) and hydrogen (right) events per unit of beam intensity as a function of the beam intensity. Both the deuterium and hydrogen data for all three of the intermediate mass data sets are shown here. The hydrogen data are offset by 90,000 units of beam intensity. Within the deuterium and hydrogen data, data sets three, four and nine are offset by 0, 30,000 and 60,000 units of beam intensity respectively.	56
5.5	Number of deuterium (left) and hydrogen (right) events per unit of beam intensity as a function of the beam intensity. Both the deuterium and hydrogen data for all three of the high mass data sets are shown here. The hydrogen data are offset by 105,000 units of beam intensity. Within the deuterium and hydrogen data, data sets three, four and nine are offset by 0, 35,000 and 70,000 units of beam intensity respectively.	62
5.6	Number of deuterium (left) and hydrogen (right) events per unit of beam intensity as a function of the beam intensity. Both the deuterium and hydrogen data for all three of the intermediate mass data sets are shown here. The hydrogen data are offset by 90,000 units of beam intensity. Within the deuterium and hydrogen data, data sets three, four and nine are offset by 0, 30,000 and 60,000 units of beam intensity respectively.	63
5.7	Number of deuterium (left) and hydrogen (right) events per unit of beam intensity as a function of the beam intensity. Both the deuterium and hydrogen data from the low mass data set are shown here. The hydrogen data are offset by 10,000 units of beam intensity.	64
5.8	The Drell-Yan cross section ratio versus x of the target parton. The results from all three mass settings are shown. The error bars represent the statistical uncertainty. An additional one percent systematic uncertainty is common to all points within a mass setting.	74
5.9	The Drell-Yan cross section ratio versus x of the target parton. The combined result from all data sets is shown. The error bars represent the statistical uncertainty. There is a less than one percent systematic uncertainty common to all points.	75
5.10	The Drell-Yan cross section ratio versus p_T . The combined result from all data sets is shown. The error bars represent the statistical uncertainty. There is a one percent systematic uncertainty common to all points.	77

5.11	\bar{d}/\bar{u} versus x . The results from all three mass settings are shown. The error bars represent the statistical uncertainty. The systematic uncertainty, which varies from about 2% at low x to a maximum of 3.5% at high x , is not shown.	80
5.12	\bar{d}/\bar{u} versus x . The combined result from all three mass settings is shown.	81
5.13	$\bar{d} - \bar{u}$ versus x . The results from all three mass settings are shown. The systematic uncertainty is shown for the high mass data. The systematic uncertainty for the other data sets are very similar.	85
5.14	$\bar{d} - \bar{u}$ versus x . The combined result from all three mass settings is shown.	86
5.15	$\int_x^{0.35} (\bar{d}(x) - \bar{u}(x)) dx'$ in the proton versus x	87
6.1	The Drell-Yan cross section ratio versus x of the target parton. The results from all three mass settings have been combined. The curves are the calculated cross section ratio using CTEQ4M [15], MRS(R2) [16], and MRST [28]. The bottom curve is calculated using CTEQ4M where $\bar{d} - \bar{u}$ has been set to zero.	90
6.2	$\bar{d}(x)/\bar{u}(x)$ versus x . The combined result from all three mass settings is shown along with three parameterizations. The NA51 data point is also shown.	91
6.3	$\bar{d}(x) - \bar{u}(x)$ versus x . The combined result from all three mass settings is shown along with three parameterizations.	92
6.4	$\int_x^{0.35} (\bar{d}(x) - \bar{u}(x)) dx'$ versus x . The curves are from three different parameterizations.	93
6.5	$F_2^p - F_2^n$ as measured by NMC at $Q = 2$ GeV compared with predictions based on the MRS(R2) parameterization. Also shown are the E866 high mass results, evolved to $Q = 2$ GeV, for the sea contribution to $F_2^p - F_2^n$. The top (bottom) curve is the valence (sea) contribution and the middle curve is the sum of the two.	95
6.6	$F_2^p - F_2^n$ as measured by NMC at $Q = 2$ GeV compared with predictions based on the MRS(R2) (solid) and MRST (dashed) parameterizations. Also shown are the E866 high mass results, evolved to $Q = 2$ GeV, for the sea contribution to $F_2^p - F_2^n$. For each prediction, the top (bottom) curve is the valence (sea) contribution and the middle curve is the sum of the two.	96

6.7	$\bar{d} - \bar{u}$ as a function of x . The E866 (HERMES) results are shown as round (square) data points. The error bars on the E866 data points represent the statistical uncertainty. The inner error bars on the HERMES data points represent the statistical uncertainty while the outer error bars represent the statistical and systematic uncertainty added in quadrature.	98
6.8	$\bar{d} - \bar{u}$ as a function of x . The E866 results are shown along with predictions of meson and chiral models. Both are shown for $Q = 6.38$ GeV.	102
6.9	\bar{d}/\bar{u} as a function of x . The E866 results are shown along with predictions of meson models. Both are shown for $Q = 6.38$ GeV.	104

Chapter 1

Introduction

In the beginning God created the heavens and the earth. Ever since that time, man has striven to understand the composition of matter. The history of the study of the building blocks of matter is a series of discoveries. With each new discovery the number and size of building blocks has decreased while the strength of the bond holding the constituents together has increased. The starting point could be considered to be the discovery of molecules. All compounds are composed of weakly bound molecules, of which there are a plethora of types. Next came the discovery that molecules are composed of atoms. It was then discovered that the atoms were made of a dense nucleus surrounded by orbiting electrons. As machines were invented that could probe matter at higher energies and correspondingly smaller sizes, it became known that nuclei had internal structure and were composed of protons and neutrons which are collectively referred to as nucleons. This series of discoveries continues as the structure of the nucleon is probed.

The discovery of large numbers of new particles, such as mesons, heavier hadrons, and antiparticles, implied there were some smaller, more basic building blocks yet to be discovered. These smallest, most tightly bound, and relatively few building blocks are described by the Standard Model. This model

has been extremely successful explaining the composition of all matter and the forces that bind them¹. The Standard Model has accomplished this using only six quarks (u, d, s, \dots), six leptons, their antiparticles ($\bar{u}, \bar{d}, \bar{s}, \dots$), and five force carriers. In fact, most of the matter we interact with every day is made of only two types, or flavors, of quarks and a single lepton.

The bulk of the matter around us is composed of nucleons and electrons. Electrons are currently believed to be fundamental particles with no discernible internal structure. Nucleons, on the other hand, do have internal structure. The Parton Model describes the nucleon as a bound state of three quarks that give the nucleon its electrical charge and other basic properties. For example, a nucleon composed of two up quarks and one down quark (uud) is a proton, while a nucleon composed of one up quark and two down quarks (udd) is a neutron. These three quarks, called valence quarks, are held together by the strong force which is mediated, or carried, by gluons (g). In addition to valence quarks and gluons, there is a background of virtual quark-antiquark pairs which come and go without affecting the basic characteristics of the nucleon, since any effect of the quark is canceled by the opposite effect of the antiquark. These components of the nucleon, shown in Fig. 1.1, are collectively referred to as partons.

One source of these quark-antiquark pairs, commonly called the sea quarks, is gluon splitting. According to a theoretical description of the strong force, Quantum Chromodynamics (QCD), a gluon can split into a quark-antiquark pair and exist for a short time before recombining into a gluon.

¹The Standard Model does not address the weakest fundamental force, which is gravity.

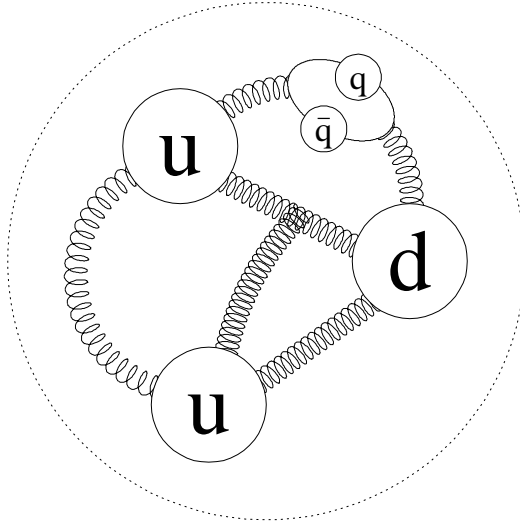


Figure 1.1: A simple picture of the proton according to the Parton Model. The proton contains 2 valence up quarks (u), one valence down quark (d), gluons (helix), and the sea of any number of quark antiquark pairs (q and \bar{q}).

This simple production mechanism implies that the sea of antiquarks in a nucleon would be flavor symmetric with respect to the up and down antiquarks. Therefore, it was initially assumed that there were as many anti-up quarks in a nucleon as there were anti-down quarks.

Over the past decade evidence has accumulated that indicates there are more anti-down quarks in a proton than anti-up quarks. The primary motivation for Experiment 866 at Fermi National Accelerator Laboratory (FNAL E866/NuSea) was to measure the ratio of anti-down quarks to anti-up quarks in the nucleon. This experiment has measured the antiquark content of the nucleon sea more precisely and extensively than any previous measurement. This dissertation will describe the NuSea experiment, including its motivation, apparatus, procedures, analysis, and conclusions.

Chapter 2

Theory and Motivation

The structure of the nucleon is difficult to study because of its small size and the large binding energy of its constituents. Nevertheless, with the aid of particle accelerators, much has been learned about the structure of the nucleon in recent years. Two electromagnetic interactions that can be produced by modern accelerators and studied at high energies are muon induced deep inelastic scattering ¹ and the Drell-Yan process. These two methods of probing the nucleon have revealed much about the nucleon sea.

2.1 Muon Induced Deep Inelastic Scattering

Deep inelastic scattering (DIS) is the process of inelastically scattering a high energy lepton off a target nucleon. In the case of muon induced DIS, shown in Fig. 2.1, the muon scatters off a single quark in the nucleon by exchanging a high energy virtual photon. The differential cross section for this interaction can be measured experimentally and expressed in terms of the two structure functions $F_1(x, Q^2)$ and $F_2(x, Q^2)$. These structure functions are functions of Bjorken- x (x), which is a dimensionless scaling variable that at high energies

¹Deep inelastic scattering induced by leptons, other than muons, will not be discussed in this dissertation.

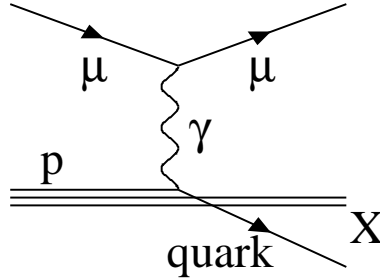


Figure 2.1: Muon induced deep inelastic scattering. In this process the high energy muon scatters off a single quark in the nucleon by exchanging a high energy virtual photon.

represents the fraction of the nucleon's longitudinal momentum carried by a parton, and Q^2 , which is the four momentum squared of the virtual photon exchanged in the process.

These two structure functions can be expressed as linear combinations of parton functions, $f_i(x, Q^2)$, which are commonly called parton distribution functions (PDF's). These PDF's are the probability of finding a parton in the nucleon that carries some fraction (x) of the nucleon's total longitudinal momentum. The relationship between the structure functions and the PDF's is:²

$$F_1(x) = \frac{1}{2} \sum_i e_i^2 f_i(x) \quad (2.1)$$

$$F_2(x) = \sum_i e_i^2 x f_i(x), \quad (2.2)$$

where the sum is over all the partons ($i = u, d, s, \dots, \bar{u}, \bar{d}, \bar{s}, \dots, g$) and e_i is the electric charge of the i -th parton. So by measuring the cross section for DIS, the internal structure of the nucleon can be studied.

²Since the Q^2 dependence is small, it will be dropped from the PDF notation for the remainder of this dissertation.

An experiment performed by the New Muon Collaboration (NMC) measured the cross section ratio for deep inelastic scattering of muons from hydrogen and deuterium [1]. Their measurement³ of F_2^n/F_2^p over the kinematic range of $0.004 < x < 0.8$ is shown in Fig. 2.2. These data points are the result of combining both the 90 GeV and 280 GeV incident muon energy measurements and adjusting the data for the small Q^2 dependence to a fixed Q^2 of 4 GeV².

The NMC measurement was used with a parameterization of the absolute deuteron structure function, F_2^d , to obtain

$$F_2^p - F_2^n = 2F_2^d \frac{1 - F_2^n/F_2^p}{1 + F_2^n/F_2^p}. \quad (2.3)$$

The solid points in Fig. 2.3 show the derived values of $F_2^p - F_2^n$ as a function of x . Also shown in this figure is $\int_x^1 (F_2^p - F_2^n) dx/x$ for the same x range of the data as well as the extrapolated result (S_G) over all values of x ($0 \leq x \leq 1$). This extrapolated result is

$$S_G \equiv \int_0^1 [F_2^p - F_2^n] \frac{dx}{x} = 0.235 \pm 0.026. \quad (2.4)$$

This result by NMC can be compared to the traditional Gottfried Sum Rule [2] (*GSR*) result of 1/3. To understand this discrepancy between the NMC measurement and the traditional result of the Gottfried Sum Rule, it is important to look at the assumptions that lead to the traditional result. Begin with the Gottfried sum as written in equation 2.4 and then use equation 2.2 to get

$$S_G = \int_0^1 \sum_i e_i^2 [q_i^p(x) + \bar{q}_i^p(x) - q_i^n(x) - \bar{q}_i^n(x)] dx. \quad (2.5)$$

³NMC actually measured $F_2^d/F_2^p \equiv 0.5(1 + F_2^n/F_2^p)$ where their convention of normalizing F_2^d per nucleon has been used here.

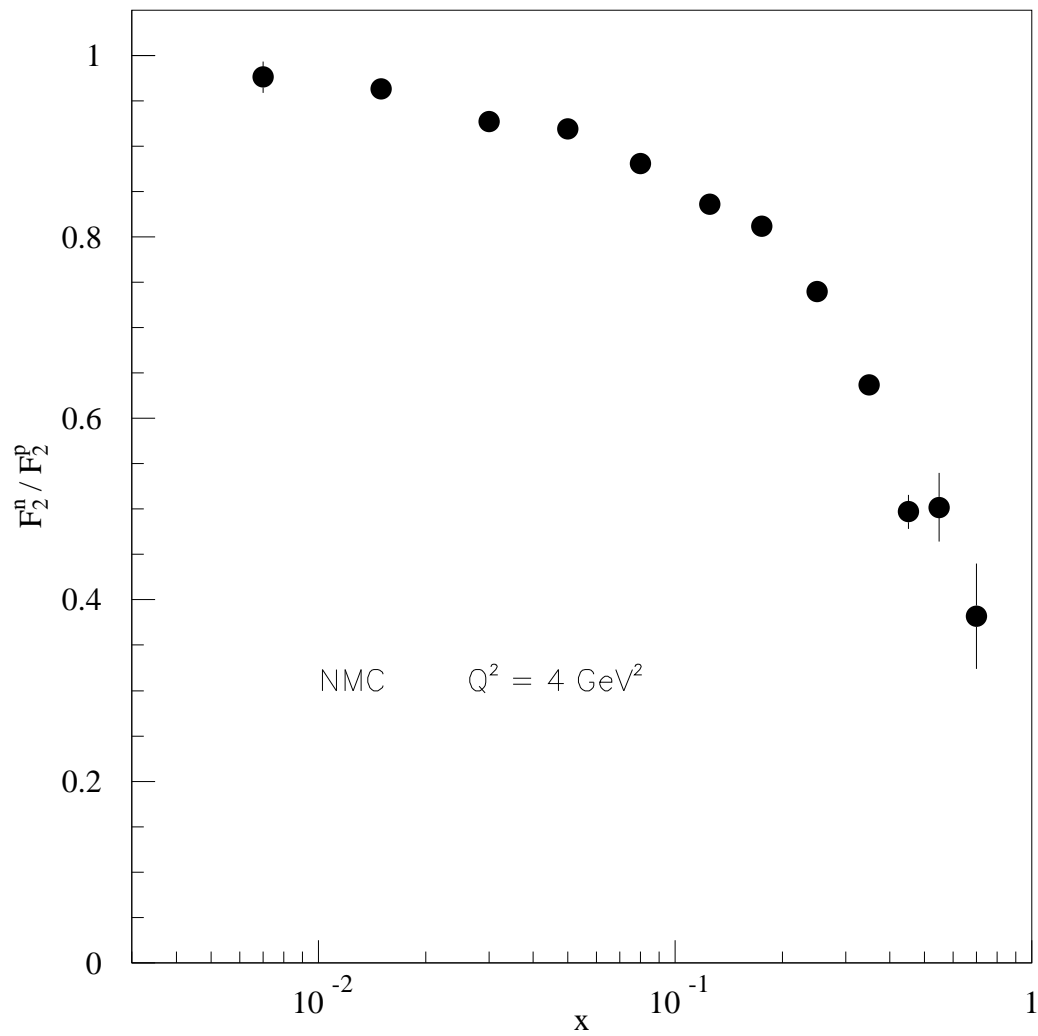


Figure 2.2: The NMC measured ratio F_2^n / F_2^p at $Q^2 = 4 \text{ GeV}^2$. Only the statistical uncertainty is shown.

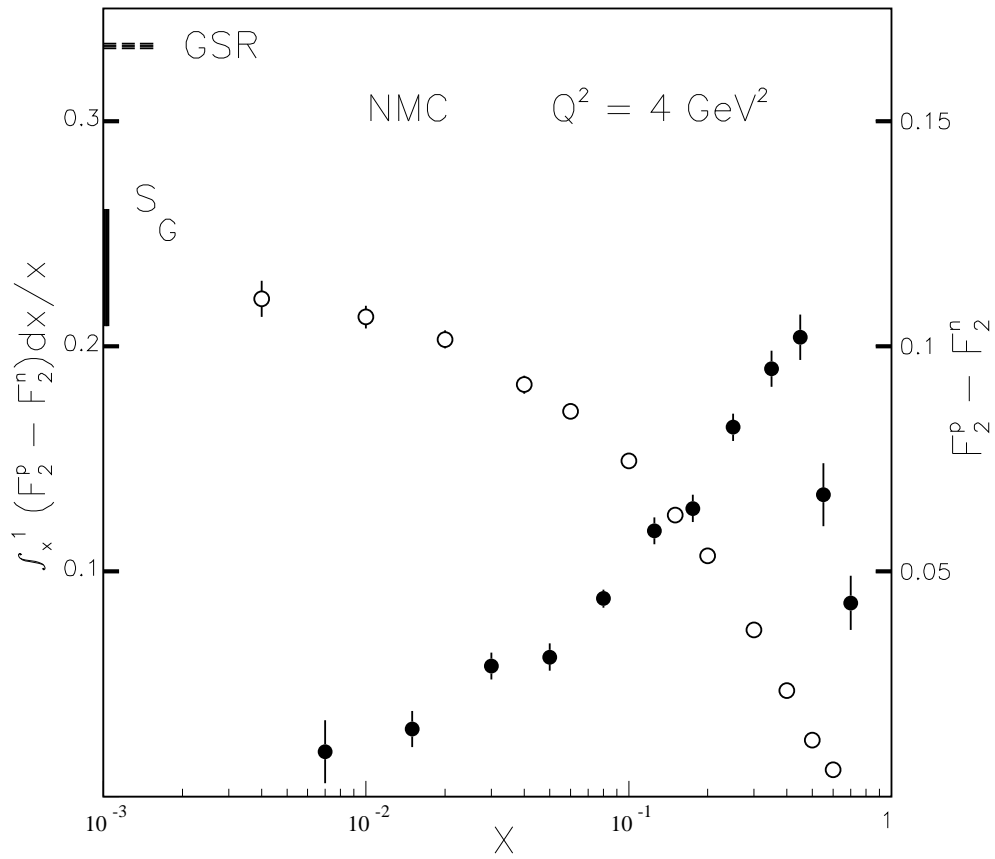


Figure 2.3: The difference $F_2^p - F_2^n$ (solid symbols and the scale to the right) and $\int_x^1 (F_2^p - F_2^n) dx/x$ (open symbols and the scale to the left) at $Q^2 = 4 \text{ GeV}^2$ as a function of x . The extrapolated integral result, S_G is indicated by the bar. The traditional Gottfried Sum Rule result, GSR is also shown.

Next assume charge symmetry⁴ to express the neutron PDF's as proton PDF's and ignore the heavier quark (e.g. s, \bar{s}, \dots) terms to get

$$S_G = \int_0^1 \frac{1}{3} [u + \bar{u} - d - \bar{d}] dx, \quad (2.6)$$

which can be rewritten as

$$S_G = \int_0^1 \frac{1}{3} [u - \bar{u}] dx - \int_0^1 \frac{1}{3} [d - \bar{d}] dx + \int_0^1 \frac{2}{3} [\bar{u} - \bar{d}] dx. \quad (2.7)$$

The first two integrals are the definition of the valence quarks, which for a proton is two up valence quarks and one down valence quark. Thus equation 2.7 is reduced to

$$S_G = \frac{1}{3} + \int_0^1 \frac{2}{3} [\bar{u} - \bar{d}] dx. \quad (2.8)$$

If it is also assumed that $\bar{d}(x) = \bar{u}(x)$, then one arrives at the traditional result of 1/3.

To reconcile the NMC measurement and the traditional Gottfried Sum result, one of the three assumptions made above must be incorrect: first is the assumption that the NMC measurement was correctly extrapolated to zero; second, that charge symmetry is valid; and third, that $\bar{d}(x) = \bar{u}(x)$.

The small x extrapolation was checked by Fermilab E665 [3], which made the same measurement as NMC except they measured the ratio for $10^{-6} \leq x \leq 0.3$. Over the kinematic range where NMC and E665 overlapped, their measurements agree. However, E665 determined that for $x \leq 0.01$ the value of $2F_2^d/F_2^p - 1$ was a constant $0.935 \pm 0.008 \pm 0.034$. While this could be interpreted as a difference between F_2^n and F_2^p , it is usually thought

⁴Charge symmetry implies that $u_p(x) = d_n(x)$, $\bar{d}_p(x) = \bar{u}_n(x)$, etc.

to be the effect of nuclear shadowing in deuterium [4], which means that $F_2^n/F_2^p \neq 2F_2^d/F_2^p - 1$. Therefore it is not possible to measure F_2^n/F_2^p in a model independent way at low x , although the same calculations confirm $F_2^n/F_2^p = 2F_2^d/F_2^p - 1$ at higher x values to a good approximation. While E665 seems to support the NMC extrapolation, it also highlights the difficulty of making and interpreting DIS measurements at small x values.

Charge symmetry is generally assumed to be well respected in strong interactions. Extensive experimental searches for charge symmetry violation effects have shown that charge symmetry holds to the order of the proton-neutron mass difference [5, 6].⁵ Therefore, charge symmetry can not explain the discrepancy between the NMC measurement and the traditional Gottfried Sum result.

The only remaining assumption is $\bar{d}(x) = \bar{u}(x)$. If this assumption is solely responsible for the discrepancy between the NMC measurement and the traditional Gottfried Sum result, it would imply

$$\int_0^1 [\bar{d}(x) - \bar{u}(x)] dx = 0.148 \pm 0.039. \quad (2.9)$$

The NMC measurement and the above analysis were the first indications that there were more anti-down quarks in the proton than anti-up quarks.

2.2 Drell-Yan

Following the publication of the NMC result, it was suggested [9] that the Drell-Yan process [10] could provide a more direct probe of the light antiquark

⁵ While it has been recently suggested that charge symmetry violation could explain the discrepancy between muon and neutrino DIS [7] data, it can not fully explain the measurement reported here [8].

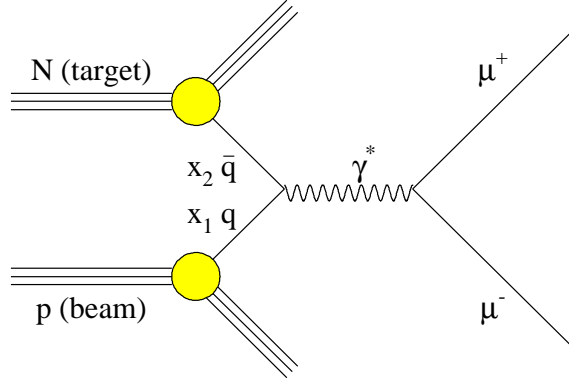


Figure 2.4: The leading order Drell-Yan process.

asymmetry of the nucleon. In its simplest form, shown in Fig. 2.4, the Drell-Yan process is the production of a lepton-antilepton pair from a virtual photon produced in a quark-antiquark annihilation. Since there are no valence antiquarks in a nucleon-nucleon interaction, the Drell-Yan process is a direct probe of the sea antiquarks.

The proton-nucleon cross section for the Drell-Yan process to lowest order in the electromagnetic fine structure constant (α), as a function of x of the initial quark and antiquark, is

$$\frac{d^2\sigma}{dx_1 dx_2} = \frac{4\pi\alpha^2}{9M^2} \sum_i e_i^2 \left[f_i(x_1) \bar{f}_i(x_2) + \bar{f}_i(x_1) f_i(x_2) \right], \quad (2.10)$$

where the sum is over all quark flavors and M is the virtual photon or dilepton mass [11]. Here the subscripts 1 and 2 denote a parton from the beam and target respectively. It is important to note that the PDF's in equation 2.10 are the same functions used in equation 2.2. This means that the DIS process and the Drell-Yan process are sensitive to the same antiquark structure of the nucleon.

Some kinematic quantities commonly used to describe Drell-Yan events are the x Feynman (x_F) and the dilepton mass (M), which are defined ⁶ as

$$x_F = \frac{p_{\parallel}^{\gamma}}{p^{\gamma,max}} \approx \frac{p_{\parallel}^{\gamma}}{\sqrt{s}/2} = x_1 - x_2 \quad (2.11)$$

and

$$M^2 = Q^2 \approx x_1 x_2 s \quad (2.12)$$

where p_{\parallel}^{γ} is the center of mass longitudinal momentum of the virtual photon, $p^{\gamma,max}$ is its maximum possible value, and s is the total four momentum squared of the initial nucleons. The momentum transverse to the beam direction (p_T) of the dileptons is used to complete ⁷ the description of the event.

The cross section for producing a Drell-Yan event in a proton-proton interaction, σ^{pp} , or proton-neutron interaction, σ^{pn} is

$$\sigma^{pp} \propto \frac{8}{9}u(x)\bar{u}(x) + \frac{2}{9}d(x)\bar{d}(x) \quad (2.13)$$

$$\sigma^{pn} \propto \frac{5}{9}u(x)\bar{d}(x) + \frac{5}{9}d(x)\bar{u}(x), \quad (2.14)$$

where the heavier quark terms have been ignored, charge symmetry has been invoked so that all the PDF's can be expressed as proton PDF's, and x_F is zero⁸. Since there is presently no way of making a free neutron target, a deuterium target is commonly used as the best approximation to a free neutron target. Making the approximation that the proton-deuterium cross section (σ^{pd}) can

⁶The approximations in these equations become exact in the infinite momentum frame. The infinite momentum frame is a boosted frame of reference where momentum transverse to the beam direction is negligible and the quarks can be considered to be massless.

⁷The complete event description includes production and decay angles but these will not be discussed in this dissertation.

⁸The reason for this simplification is so that this discussion can be compared to the NA51 measurement. This simplification is not applicable to E866.

be written as

$$\sigma^{pd} \approx \sigma^{pp} + \sigma^{pn} \quad (2.15)$$

ignores the small ⁹ nuclear effects inside the deuterium nucleus. Using this approximation the measured cross section ratio can be written as,

$$\left. \frac{\sigma^{pd}}{\sigma^{pp}} \right|_{x_1=x_2} = \frac{8 + 5\frac{\bar{d}}{u} + 5\frac{d}{u} + 2\frac{\bar{d}}{u}\frac{d}{u}}{8 + 2\frac{\bar{d}}{u}\frac{d}{u}} \quad (2.16)$$

where, for simplicity, the notation showing the x dependence has been dropped.

From this measurable quantity, one can solve for \bar{d}/\bar{u} ,

$$\frac{\bar{d}}{\bar{u}} = \frac{8\left(1 - \frac{\sigma^{pd}}{\sigma^{pp}}\right) + 5\frac{d}{u}}{2\frac{d}{u}\left(\frac{\sigma^{pd}}{\sigma^{pp}} - 1\right) - 5}. \quad (2.17)$$

Therefore by measuring the hydrogen and deuterium Drell-Yan cross sections, the nucleon antiquark sea can be measured.

The first experiment ¹⁰ to follow up this idea was NA51 at CERN [12]. It used the primary proton beam from the CERN-SPS to supply 450 GeV/c protons, which interacted in one of three identical vessels that contained either liquid hydrogen, liquid deuterium or a vacuum. From the almost six thousand reconstructed Drell-Yan events with a mass above 4.3 GeV it was determined that

$$\frac{\sigma^{pp} - \sigma^{pn}}{\sigma^{pp} + \sigma^{pn}} = -0.09 \pm 0.02 \pm 0.025. \quad (2.18)$$

⁹FNAL E772 [13] searched for nuclear effects in Drell-Yan production and found none except for shadowing at small values of x .

¹⁰FNAL E772 [14] was the first Drell-Yan experiment to look for flavor asymmetry in the nucleon sea, but they measured cross sections from isoscalar targets and W, which has a large neutron excess. This measurement was not as sensitive to \bar{d}/\bar{u} as measurements using deuterium and hydrogen targets.

These events were centered at $x_F = 0$ with both x_1 and x_2 between 0.08 and 0.53. Since the acceptance of the NA51 spectrometer was narrow and statistics were limited, the measurement was not reported as a function of x , but only at the average of $x_2 = 0.18$.

From the measured cross section asymmetry, it was determined that

$$\left. \frac{\bar{u}_p}{\bar{d}_p} \right|_{\langle x \rangle = 0.18} = 0.51 \pm 0.04 \pm 0.05. \quad (2.19)$$

This was the first direct determination of the ratio of \bar{d} to \bar{u} , but the limited statistics of this measurement restricted it to a single x value.

One of the main limitations of the NA51 experiment was the limited kinematic coverage that was sharply peaked near $x_F = 0$. A better measurement of \bar{d}/\bar{u} could have been made if the acceptance was largest for $x_F > 0$, since the Drell-Yan cross section ratio is more sensitive to the antiquark distribution in this kinematic regime. The increased sensitivity results because in this kinematic regime the Drell-Yan cross section is dominated by the annihilation of a beam quark with a target antiquark. Using the same assumptions that led to equations 2.13 and 2.14, except assuming that $x_1 \gg x_2$ instead of $x_1 = x_2$, results in the relations

$$\sigma^{pp} \propto \frac{4}{9}u(x_1)\bar{u}(x_2) + \frac{1}{9}d(x_1)\bar{d}(x_2) \quad (2.20)$$

and

$$\sigma^{pn} \propto \frac{4}{9}u(x_1)\bar{d}(x_2) + \frac{1}{9}d(x_1)\bar{u}(x_2). \quad (2.21)$$

From these two equations it is a simple matter to derive

$$\left. \frac{\sigma^{pd}}{2\sigma^{pp}} \right|_{x_1 \gg x_2} \approx \frac{1}{2} \frac{\left(1 + \frac{1}{4} \frac{d(x_1)}{u(x_1)}\right)}{\left(1 + \frac{1}{4} \frac{d(x_1)}{u(x_1)} \frac{\bar{d}(x_2)}{\bar{u}(x_2)}\right)} \left(1 + \frac{\bar{d}(x_2)}{\bar{u}(x_2)}\right). \quad (2.22)$$

This expression can be further simplified by making the additional assumption that $d(x) \ll 4u(x)$ which yields

$$\frac{\sigma^{pd}}{2\sigma^{pp}} \Big|_{x_1 \gg x_2} \approx \frac{1}{2} \left(1 + \frac{\bar{d}(x_2)}{\bar{u}(x_2)} \right). \quad (2.23)$$

This equation illustrates the sensitivity of the Drell-Yan cross section ratio to \bar{d}/\bar{u} but is valid only for $x_1 \gg x_2$.

2.3 Global Fits

Several groups have applied phenomenological models to the results from DIS, Drell-Yan, and other methods ¹¹ of probing the nucleon to generate complete sets of PDF's. This method of fitting all the relevant data is called a global fit. Two groups that have generated global fits parameterizing the nucleon sea are CTEQ [15] and MRS [16]. Prior to the measurements by NMC and NA51, the usual assumption was that $\bar{d}(x) = \bar{u}(x)$. A typical parameterization of the proton with this assumption is shown in Fig. 2.5.

Prior to FNAL E866/NuSea, the main constraints on the global fits of $\bar{d}(x)$ and $\bar{u}(x)$ were the NMC and NA51 results. While these measurements were important to show that $\bar{d} \neq \bar{u}$, neither imposed rigid constraints on the global fits of $\bar{d}(x)$ and $\bar{u}(x)$. The NA51 measurement only constrained the ratio of $\bar{d}(x)$ to $\bar{u}(x)$ at $x = 0.18$, while the NMC measurement only constrained the integral of the difference between $\bar{d}(x)$ and $\bar{u}(x)$, which primarily constrains the PDF's at small values of x . This poorly constrained parameterization, shown

¹¹These 'other methods', which will not be discussed in this dissertation, include neutrino induced DIS, W production asymmetry, and Semi-inclusive DIS.

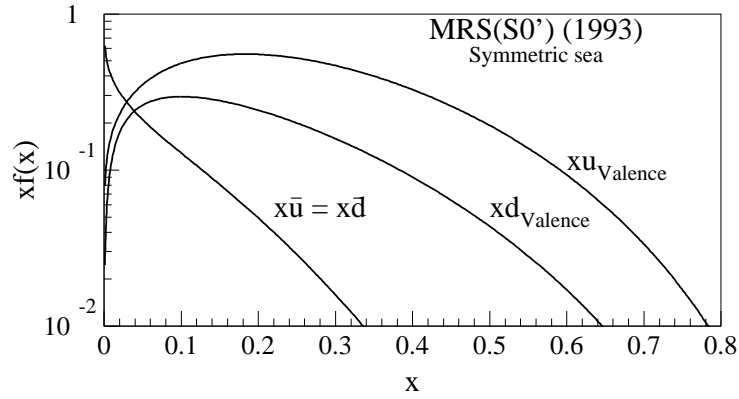


Figure 2.5: An old parameterization of the proton by MRS assuming a symmetric sea [17]. These parton distribution functions are shown for $Q^2 = 54 \text{ GeV}^2$.

in Fig. 2.6, constituted the world's best guess at the structure of the nucleon sea prior to the measurement reported here.

The goal of FNAL E866/NuSea was to measure the ratio of the Drell-Yan cross section for proton-deuteron interactions to proton-proton interactions over the kinematic range of $0.04 \leq x \leq 0.3$ with a systematic uncertainty of less than 1.5%. This measurement would provide stringent constraints on the ratio of $\bar{d}(x)$ to $\bar{u}(x)$ over the same x region.

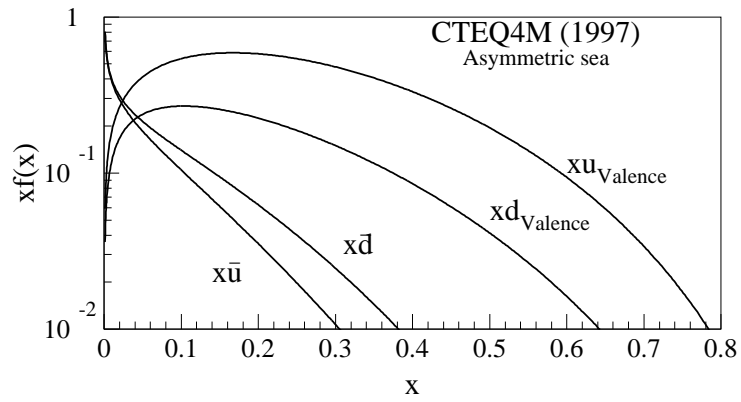


Figure 2.6: An old parameterization of the proton published by CTEQ [15] prior to FNAL E866/NuSea. These parton distribution functions are shown for $Q^2 = 54 \text{ GeV}^2$.

Chapter 3

Experimental Setup

The goal of this experiment was to measure the ratio of Drell-Yan events from proton-proton interactions to proton-deuteron interactions. To count the number of Drell-Yan events it was necessary to detect pairs of high energy oppositely charged muons. The kinematics of the interaction were determined from the four momentum of each muon produced in the Drell-Yan process. This was accomplished for each muon in a pair of oppositely charged muons (called a dimuon event) by reconstructing the path of each muon through a series of tracking stations and dipole magnets.

This chapter will describe the experimental apparatus used to make this measurement. The equipment will be described in the order through which a particle would traverse the setup, starting with a description of the beam, then the targets, and finally the spectrometer. The coordinate system used throughout this experiment has the positive z-axis in the direction of the incoming beam, the y-axis oriented with the positive direction pointing up, and the x-axis is chosen to complete a right-handed coordinate system.

3.1 Beamline and Beam Monitors

The beam used in this experiment was an 800 GeV/c proton beam extracted from the Fermilab Tevatron accelerator. The beam was extracted slowly over a twenty second time period, once per minute. This slow extraction is referred to as a spill. Within each spill, the beam arrived in small bunches, called "buckets", every 19ns. The frequency of the buckets was determined by the radio frequency (RF) of the accelerator, which was 53 MHz.

As the beam was transported down the east beamline in the Meson experimental hall, its size, position, and intensity were monitored with several different detectors. The beam position and size were measured using RF cavities and segmented wire ion chambers (SWIC's). The last check of the beam, about 70 inches upstream of the targets, was performed by a movable SWIC. This SWIC had wire spacing of 2mm in the horizontal direction and 0.5mm in the vertical direction. The size of the beam at the SWIC was typically about 6mm wide and 1mm high (full-width at half-maximum).

The beam intensity was also monitored by several different detectors. The primary monitor was a secondary emission monitor (SEM) located about 100m upstream of the targets. In addition to the SEM, the beam intensity was monitored with a quarter-wave RF cavity and an ion chamber (IC3). The SEM calibration was determined to be $7.9 \pm 0.6 \times 10^7$ protons per SEM count[19] using the methods described in Section 4.5. The nominal maximum beam intensity ¹ was 2×10^{12} protons per spill.

¹ The nominal maximum beam intensity for the low mass data (see section 5.1) was 5×10^{11} protons per spill.

Approximately 85° from the beam direction in the x-z plane were a pair of four-element scintillator telescopes called AMON and WMON. These scintillator telescopes viewed the target through a hole in the heavy shielding enclosing the targets. The purpose of these detectors was to monitor the luminosity of the beam hitting the target, which was then used to determine the beam duty factor, data acquisition livetime and the target position.

3.2 Targets

The 800 GeV/c extracted proton beam passed through one of three target flasks. Figure 3.1 shows one of the three identical twenty inch long flasks which were cylindrical in shape with hemispherical ends. The flasks were constructed of thin stainless steel with an insulated vacuum jacket around each flask. One flask was filled with liquid deuterium, another was filled with liquid hydrogen, and the third was evacuated. The hydrogen target was 7% of an interaction length and 6% of a radiation length. The deuterium target was 15% of an interaction length and 7% of a radiation length. The evacuated target was less than 0.2% of an interaction length and 1.4% of a radiation length. Both the temperature and the vapor pressure of the filled flasks were monitored.

All three flasks were mounted on a movable table so that the target could be changed between spills. The normal target cycle was twelve spills long with five spills on the deuterium target, one spill on the empty flask, five spills on the hydrogen target and another spill on the empty flask. The electronics that automatically cycled the targets checked that the spill had at least 4×10^{10} protons before it counted the spill. This prevented the target from cycling while the accelerator was off. This frequent cycling of the targets

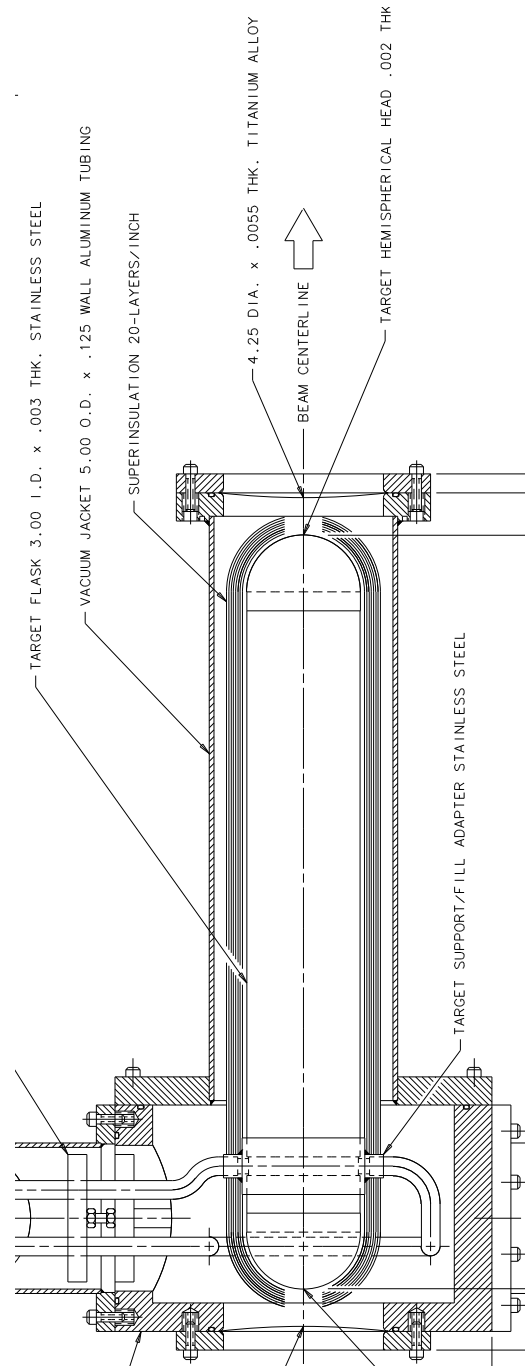


Figure 3.1: One of the three identical E866 target flasks.

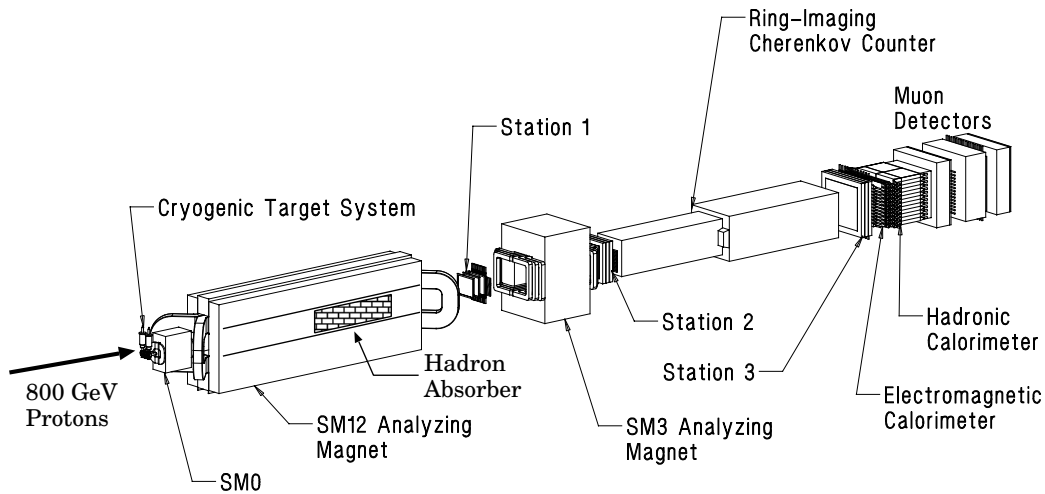


Figure 3.2: The FNAL E866/NuSea Spectrometer

minimized many of the systematic uncertainties between the targets when the cross section ratio was determined.

3.3 E866 Spectrometer

The primary apparatus used in this experiment was the dimuon spectrometer [18] shown in Fig. 3.2. This was the fourth experiment to use this spectrometer that was located on the east side of the Meson experimental building at Fermilab. While changes have been made to the spectrometer for each experiment, the basic design has remained the same since the spectrometer was first used for E605 in the early 1980's.

Downstream of the targets the particles encountered the first of three magnets. All three magnets used in this spectrometer were dipole magnets with the magnetic field aligned in the x direction so that they caused charged particles moving in the z direction to bend in the plus or minus y direction.

The first dipole magnet (SM0) was the smallest, measuring 72 inches long. It provided a transverse momentum deflection of $0.94 \text{ GeV}/c$ when operated at a maximum current of 2100 amps. This magnet was used to increase the opening angle of dimuon pairs when taking data with the magnets configured to have the lowest mass acceptance. The aperture of this magnet was filled with a helium bag. The purpose of this and all other helium bags was to minimize the material that the muons traversed in order to minimize their multiple scattering.

Following the first magnet was the largest magnet (SM12), measuring over 47 feet long. When operated at a maximum current of 4000 amps, it provided a transverse momentum deflection of $7 \text{ GeV}/c$. This magnet focused the dimuons through the remainder of the spectrometer. Sixty-eight inches into the aperture of this magnet was a beam dump. The protons that did not interact in the target interacted in the 129 inch long copper beam dump. The beam dump was about 22 interaction lengths or 230 radiation lengths. The dump prevented the beam from passing through the active elements of the spectrometer. The beam dump filled the aperture in the x direction for most of its length, but was a maximum of ten inches thick in the y direction. This allowed many of the dimuons of interest to travel above and below the beam dump.

At the downstream end of the beam dump was an absorber wall that completely filled the aperture of the magnet in both the x and y directions. This wall, shown in Fig. 3.3, was built in seven layers. The first layer was 24 inches of copper, followed by four layers of carbon that were each 27 inches thick. The last two layers were each composed of 36 inches of borated polyethylene. The

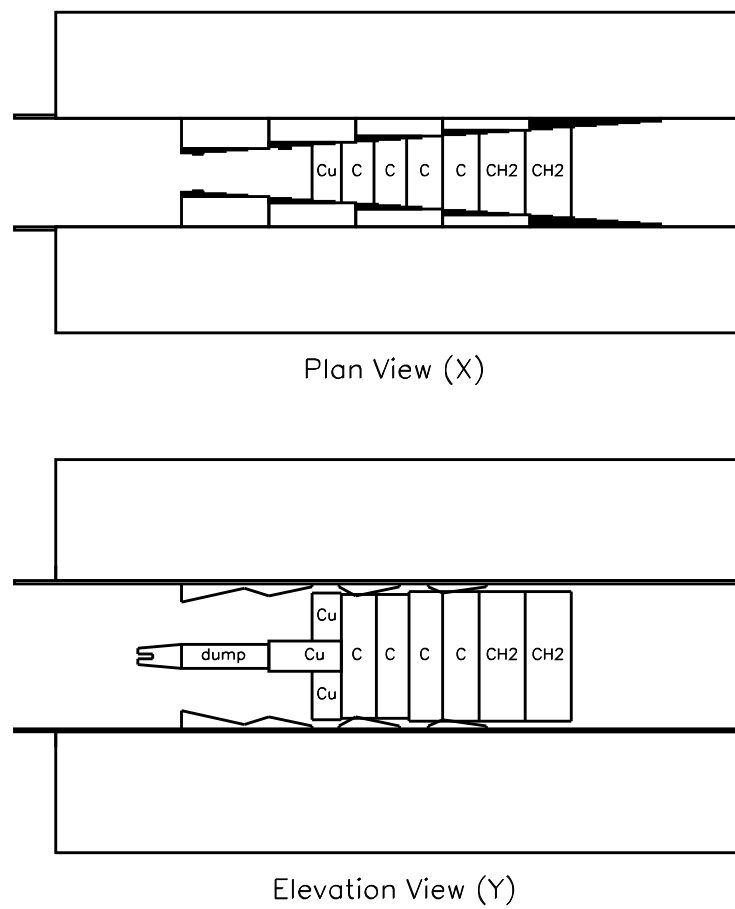


Figure 3.3: The beam dump and absorber wall inside the aperture of SM12. The beam dump is not shown in the plan view.

effect of this wall, which was over thirteen interaction lengths and sixty radiation lengths long, was to absorb most of the hadrons, electrons, and gammas that were produced in the target or the beam dump. Essentially, only muons were allowed to traverse the active elements of the spectrometer, allowing a higher beam intensity to be used while still keeping the instantaneous number of hits in each drift chamber at acceptable levels. Following the absorber wall and still inside the aperture of SM12 was another helium bag.

Downstream of SM12 was the first of three similar tracking stations (station one). Station one consisted of three pairs of drift chambers. The first pair of planes, called U1 and U1', had sense wires which were oriented at approximately $+14^\circ$ ($\tan \theta = 0.25$) in the x-y plane. The second pair of planes, called Y1 and Y1', were horizontal so that they measured the position of the particle in the y direction. The third pair of planes, called V and V', were oriented at approximately -14° in the x-y plane. The primed planes were offset in the direction perpendicular to the wires by half a drift cell to help resolve the ambiguity of the drift direction. These six drift chambers were used to track particles accurately and had enough redundancy to continue adequate performance even if some of the channels were inoperative.

While the drift chambers had excellent position resolution, they could not distinguish between beam buckets within a spill and were too slow to use as input to a trigger. Therefore, in addition to the drift chambers, planes of scintillators called hodoscopes were used. The two hodoscope planes at station one were made of counters which were oriented perpendicular to one another. The plane with horizontal paddles measured the y position of the muons and therefore was called the Y1 hodoscope. The paddles in this plane were split at

x equal to zero leaving a 0.47 inch gap. The other plane measured the position of the muons in the x direction and was called the X1 hodoscope. The paddles in X1 were split at y equal to zero leaving a 0.38 inch gap.

Following station one was the final dipole magnet (SM3). This magnet had a large aperture, measuring about six feet high and five feet wide, which was filled with another helium bag. This magnet was always operated at a current of 4230 Amps, which provided a transverse momentum deflection of 0.91 GeV/c. Unlike the first two magnets whose primary purpose was to focus the dimuons into the active elements of the spectrometer, this magnet primarily was a momentum analyzing magnet. The bend in the muon tracks as they passed through this magnet was used to determine the momentum and the sign of the electric charge of the muon.

The second tracking station, which followed SM3, was a slightly larger version of the first tracking station. Like the first station it also had three pairs of drift chambers (called U2, U2', Y2, Y2', V2, and V2') but, unlike the first station, the second station had only one hodoscope (Y2) that measured the y position of the muons.

As shown in Fig. 3.2, the second tracking station was followed by a ring imaging Cherenkov counter (RICH). In previous experiments the RICH was used for particle identification, but it was not needed for this experiment. Therefore, it was filled with helium to reduce multiple scattering of the muons.

Downstream of the RICH was the third tracking station. Except for being larger in size, station three was identical to station one. It contained

three pairs of drift chamber planes (U3, U3', Y3, Y3', V3, and V3') and two planes of hodoscopes (Y3 and X3).

Like the RICH, the calorimeters that followed station three were not used for this experiment. The calorimeter served only as additional shielding before the station four detectors. Upstream of and between some of the planes in station four were large amounts of concrete and zinc shielding. This shielding served as a final barrier to all particles except muons (and of course neutrinos), so station four was also known as the muon detectors.

Since station four was so large and because the additional shielding upstream of station four caused multiple scattering of the muons, the precise position resolution of drift chambers was not practical or necessary. Therefore, poorer resolution proportional tubes were used in place of drift chambers in station four. There were three planes of proportional tubes. Two planes measured the y position (PTY1 and PTY2) and one plane measured the x position (PTX). Station four also had two hodoscope planes (Y4 and X4).

The drift chambers and proportional tubes used the same gas mixture. The mixture was 50% argon and 50% ethane with a small amount of ethanol added by bubbling the mixture through ethanol, maintained at a constant 25° F. The ethanol was added to prevent the buildup of deposits on the wires in the drift chambers and to act as a quencher to minimize sparking.

A summary of the physical construction of the drift chambers, hodoscopes, and proportional tubes can be found in Tables 3.1, 3.2, and 3.3 respectively. Also included in these tables are the operating high voltages for each plane. Average drift chamber efficiencies are listed in Table 3.4 for each

Table 3.1: Information on the drift chambers. Drift cell and aperture sizes are in inches.

detector	number of wires	drift cell size	aperture (x × y)	operating voltage
Y1	160	0.25 in.	48 in. × 40 in.	+1700 V
Y1'	160	0.25 in.	48 in. × 40 in.	+1700 V
U1	200	0.25 in.	48 in. × 40 in.	+1700 V
U1'	200	0.25 in.	48 in. × 40 in.	+1700 V
V1	200	0.25 in.	48 in. × 40 in.	+1700 V
V1'	200	0.25 in.	48 in. × 40 in.	+1700 V
Y2	128	0.40 in.	66 in. × 51.2 in.	-2000 V
Y2'	128	0.40 in.	66 in. × 51.2 in.	-2000 V
U2	160	0.388 in.	66 in. × 51.2 in.	-1950 V
U2'	160	0.388 in.	66 in. × 51.2 in.	-1975 V
V2	160	0.388 in.	66 in. × 51.2 in.	-2000 V
V2'	160	0.388 in.	66 in. × 51.2 in.	-2000 V
Y3	112	0.82 in.	106 in. × 91.8 in.	-2200 V
Y3'	112	0.82 in.	106 in. × 91.8 in.	-2200 V
U3	144	0.796 in.	106 in. × 95.5 in.	-2200 V
U3'	144	0.796 in.	106 in. × 95.5 in.	-2200 V
V3	144	0.796 in.	106 in. × 95.5 in.	-2200 V
V3'	144	0.796 in.	106 in. × 95.5 in.	-2150 V

data set. Typical hodoscope efficiencies are listed in Table 3.5 for each mass setting.

3.4 Data Acquisition System

Although much of the data acquisition system (DAQ) was several years old, it was a very fast system. When the trigger was satisfied, the DAQ would record information from the spectrometer. Additionally, the DAQ would also record to tape information about each beam spill. The following subsections will describe when, how, and what information was recorded to data tapes.

Table 3.2: Information on hodoscopes. The counter width, aperture sizes, and the center gap size are in inches.

detector	number of counters	counter width	aperture (x×y)	center gap width
Y1	2×16	2.50 in.	47.50 in.×40.75 in.	0.47 in.
X1	12×2	4.00 in.	47.53 in.×40.78 in.	0.38 in.
Y2	2×16	3.00 in.	64.63 in.×48.63 in.	0.66 in.
X3	12×2	8.68 in.	105.2 in.×92.00 in.	1.00 in.
Y3	2×13	7.50 in.	104.0 in.×92.00 in.	0.00 in.
Y4	2×14	8.00 in.	116.0 in.×100.0 in.	0.00 in.
X4	16×2	7.125 in.	126.0 in.×114.0 in.	0.00 in.

Table 3.3: Information on proportional tubes. Drift cell and aperture sizes are in inches.

detector	number of wires	drift cell size	aperture (x × y)	operating voltage
PT-Y1	120	1.00 in.	117 in. ×120 in.	+2500 V
PT-X	135	1.00 in.	135.4 in.×121.5 in.	+2500 V
PT-Y2	143	1.00 in.	141.5 in.×143 in.	+2500 V

Table 3.4: Drift chamber efficiency in percent.

detector	data set					
	3	4	5	7	8	11
Y1	93.0	92.4	92.0	93.0	94.6	89.0
Y1'	94.5	93.2	97.2	94.2	94.3	93.9
U1	97.7	97.0	97.9	98.4	98.3	98.2
U1'	96.5	94.4	95.9	96.0	95.9	95.9
V1	97.7	96.5	96.6	98.4	98.4	95.9
V1'	98.1	97.2	98.6	99.0	99.0	98.7
Y2	95.8	95.1	95.0	95.9	96.2	95.8
Y2'	96.1	95.7	96.0	96.6	96.3	95.8
U2	96.2	95.8	95.9	96.5	96.6	96.5
U2'	96.0	95.6	96.1	96.3	96.6	96.9
V2	96.8	96.7	96.6	97.2	97.1	97.2
V2'	96.7	96.6	96.6	97.0	96.5	96.8
Y3	94.6	94.5	93.5	96.6	94.9	94.5
Y3'	95.6	95.2	95.2	97.0	96.9	96.7
U3	95.8	95.2	95.5	97.1	97.1	96.9
U3'	96.4	96.0	95.9	97.8	97.7	97.5
V3	95.7	95.3	95.2	97.1	97.1	96.7
V3'	95.1	94.7	94.3	96.2	95.8	95.0

Table 3.5: Typical Hodoscope efficiencies in percent. The Y planes are divided at $y = 0$ and L (R) denotes the left (right) half plane. The X planes are divided at $x = 0$ and U (D) denotes the upper (lower) half plane.

detector	mass setting		
	low	int.	high
Y1L	99.9	99.1	99.6
Y1R	99.8	99.8	99.7
X1U	100.0	99.8	99.7
X1D	99.5	100.0	100.0
Y2L	97.0	97.5	97.8
Y2R	98.2	99.4	98.8
Y3L	100.0	99.9	99.9
Y3R	100.0	99.9	100.0
X3U	99.5	99.8	99.5
X3D	99.5	96.8	98.7
Y4L	100.0	100.0	100.0
Y4R	100.0	100.0	100.0
X4U	99.9	99.1	100.0
X4D	100.0	99.7	100.0

3.4.1 Trigger

Events were only written to tape when the trigger was satisfied and only if the DAQ was not already busy reading out a previous event. The trigger was optimized to detect events that consisted of two muons originating from the target. A new trigger system was implemented for E866 that used only the signals from the hodoscopes to determine if the event should be written to tape [20, 21].

The signals from the Y1, Y2, and Y4 hodoscopes were compared with the contents of a three dimensional look-up table. This table was generated by Monte Carlo studies of dimuon events from the target. If the hits in the scintillators matched one of the possible dimuon trajectories through the spectrometer according to the look-up table, the trigger was satisfied. Once the trigger was satisfied, the readout busy signal was set until the event was completely recorded in the VME system memory.

In addition to the standard physics triggers that were optimized to detect oppositely charged dimuon events from the targets, other triggers were prescaled to record a limited number of study events. These study events included single muon events, events that relied only on the x hodoscope planes and other diagnostic triggers. One of the most important study triggers was the trigger that was satisfied by two like-sign muons from the target area that traveled down opposite sides of $x = 0$ in the spectrometer. The importance of some of these specialty triggers will be discussed in section 5.5.

3.4.2 Readout System

Once the trigger was satisfied, it was the responsibility of the readout system to record to tape all of the needed information to properly reconstruct the event. The readout system was composed of Nevis Transport electronics [22], VME modules, and CAMAC modules. All detector subsystems fed data onto the Transport 16-bit bus. Transport read out the coincidence registers (CR) from the hodoscopes and proportional tubes, time-to-digital converters (TDC) from the drift chambers, and a variety of information about the trigger condition from the trigger bit latches. All of the data fed onto the Transport bus were then transferred to a VME-based memory buffer. The VME system would then format the data and write it to 8mm data tapes without increasing the detector deadtime by taking advantage of the forty seconds each minute when there was no beam in the spectrometer [23].

In addition to the information from the spectrometer recorded for each event, the readout system also recorded information necessary to the analysis from each beam spill. This information included the beam intensity, position, size and duty factor, the pressure, temperature, and position of the targets, magnet voltages and currents, and various monitors used for calculating the readout deadtime. The inclusion of these data with the event data was one of the major improvements in the DAQ VME system originally built for E789.

Chapter 4

Experimental Procedures

This chapter focuses on the procedures used in this experiment. Preparation for this experiment started years before the first data were taken, and work continued throughout the year of data collecting. This chapter is a description of this work, in which the author played a significant role. The first two sections detail what was done to recommission the spectrometer before the accelerator was turned on. The third section will describe the work that was done to tune up the spectrometer after receiving beam, but before data could be taken. Section four will explain the standard data taking procedures, and the last section will describe special procedures that were required periodically.

4.1 Recommissioning the Spectrometer

Many of the detectors, cables, and readout electronics were unchanged from previous experiments that used this spectrometer. However, this equipment lay idle for five years in a dirty environment that was subject to extreme temperature and humidity fluctuations. Therefore, many months of work were necessary to restore the spectrometer to operating conditions.

The cables that carried the signals from the drift chambers to the TDC's were 100 wire ribbon cables that were several hundred feet long called Ansley

cables. These cables were extra long so that the signals from the drift chambers would be delayed while the trigger information was being processed. The connectors at the ends of these cables were large paddles with exposed wires. The rough treatment these cables experienced since they were last used damaged many of them. Each cable was untangled, each wire was tested, and many repairs were necessary. Finally the cables were reattached to the detectors and the readout electronics.

The station three and four hodoscopes were all checked for light leaks. The station two hodoscope paddles had become severely misaligned during the past five years and had to be remounted. The signal and high voltage cables were checked, repaired if necessary, and reattached. All of the electronics from the preamplifiers all the way to the tape drives were tested and repaired as necessary.

4.2 Commissioning the New Parts of the Spectrometer

The spectrometer was upgraded in many areas for this experiment. The station one hodoscopes and drift chambers were replaced with larger detectors in the y-direction, to almost double the acceptance of the spectrometer. The drift chambers had to be designed, built, mounted, aligned, and tested. The hodoscopes were expanded by adding eight new scintillator paddles to Y1 and by replacing all of the scintillators in X1 with longer scintillators. The scintillating material used in stations one and two was 3 mm thick BC-408. The new dimensions of the station one detectors are shown in Tables 3.1 and 3.2.

The trigger was also completely replaced. The old trigger processor was removed and several new trigger modules were designed, built, installed,

and tested [20, 21]. The new trigger, described in Section 3.4.1, performed extremely well.

The DAQ underwent a serious overhaul from its previous configuration. The previous experiments used a PDP-11 to control parts of the DAQ. The VME part of the system was enhanced to replace these functions and to handle much higher data rates.

Another dipole magnet (SM0) was added to the front of the spectrometer. Because of the coupling of the two magnets, the magnetic fields in SM0 and the upstream end of SM12 had to be measured. This was done by measuring the magnetic fields on a three dimensional grid throughout the aperture of the magnets.

4.3 Spectrometer Tune-up with Beam

Once the accelerator was turned on and beam was delivered to the Meson Center beam dump, tuning of the spectrometer commenced. The proton beam hitting this beam dump, which was about 1400 ft upstream of the spectrometer, produced enough muons that some were detected. This low flux of muons coming through the spectrometer allowed for the alignment of the hodoscopes and drift chambers as well as a test of the new trigger and DAQ systems.

When the proton beam finally came down the Meson east beamline, the high voltage settings for the hodoscopes and drift chambers were rechecked. These voltages were optimized to perform at the maximum efficiency without causing excessive noise or damaging the detectors. The timing of each hodoscope channel was also checked and adjusted to ensure that all of the ho-

doscope signals were in coincidence with each other to within approximately one nanosecond. This provided one beam bucket resolution and was critical to ensure that the trigger worked properly.

4.4 Standard Data Taking Procedures

Throughout the year of data-taking the spectrometer, DAQ, beam, targets, magnets, and the gas systems were constantly monitored. Twice a day a shift check was performed. This checked the target pressure and temperature, the drift chamber and proportional tubes gas flow, gas pressure, and high voltages, beam duty factor, and magnet settings.

To better monitor the spectrometer performance and data quality during data-taking, a portion of the data was analyzed in real time. A fraction of the data events that were recorded to tape were routed across the network to a Silicon Graphics workstation. The on-line analysis of these events provided an excellent means of monitoring the spectrometer performance.

Among the many means of evaluating the spectrometer performance provided by the on-line analysis, were hit distributions in the hodoscopes, drift chambers, and proportional tubes. These distributions would quickly show any channels that suffered from the two most common modes of failure, which were not ever showing a hit or showing a hit for every event. The performance of the readout system was monitored by the on-line analysis. If the format of a data event was improper, then the analysis generated an error. The on-line analysis also gave some indication about the data quality. Even though only a fraction of the events were analyzed, the reconstructed events were sufficient to produce a simple J/ψ or Υ peak in the mass spectrum.

4.5 Special Data Taking Procedures

In addition to the normal daily activities required to take data, some special measurements were taken periodically. The SEM counter calibration was checked using a single beam measurement. Instead of splitting the beam into several separate channels and sending it to different experimental areas at the same time, as was the usual practice, the beam was delivered only to the Meson east beam line. This allowed the SEM counter in this beamline to be calibrated against the beam intensity monitors in the Tevatron.

Another type of special measurement was the hodoscope efficiency studies. Since the normal trigger relied on signals from the hodoscopes, it was not very effective at monitoring the hodoscope efficiency. Therefore, dedicated data taking with a different trigger was necessary. These runs were performed for each data set.

Chapter 5

Analysis

This chapter will explain the process that was used to analyze the data. First, the data will be described. Then, the first pass analysis of all of the data will be discussed. Next, the analysis of the data summary tapes (DST), also referred to as the second pass analysis, will be explained. The final set of cuts implemented on the output of the second pass analysis and their justification will be reviewed. After the corrections for randoms, rate dependence, and target composition have been explained, then the Drell-Yan cross section ratio will be calculated. Finally, the ratio of $\bar{d}(x)$ to $\bar{u}(x)$ will be determined.

5.1 Data Sets

The data recorded to tape were categorized according to the dimuon mass that had the maximum acceptance. The spectrometer acceptance was varied by changing the current and polarities in the first two magnets in the spectrometer. These three categories were referred to as high, intermediate, and low mass settings. The motivation for these names can easily be understood by referring to Fig. 5.1, which shows the dimuon mass distributions for the three mass settings.

The data were further divided into data sets based on the magnet po-

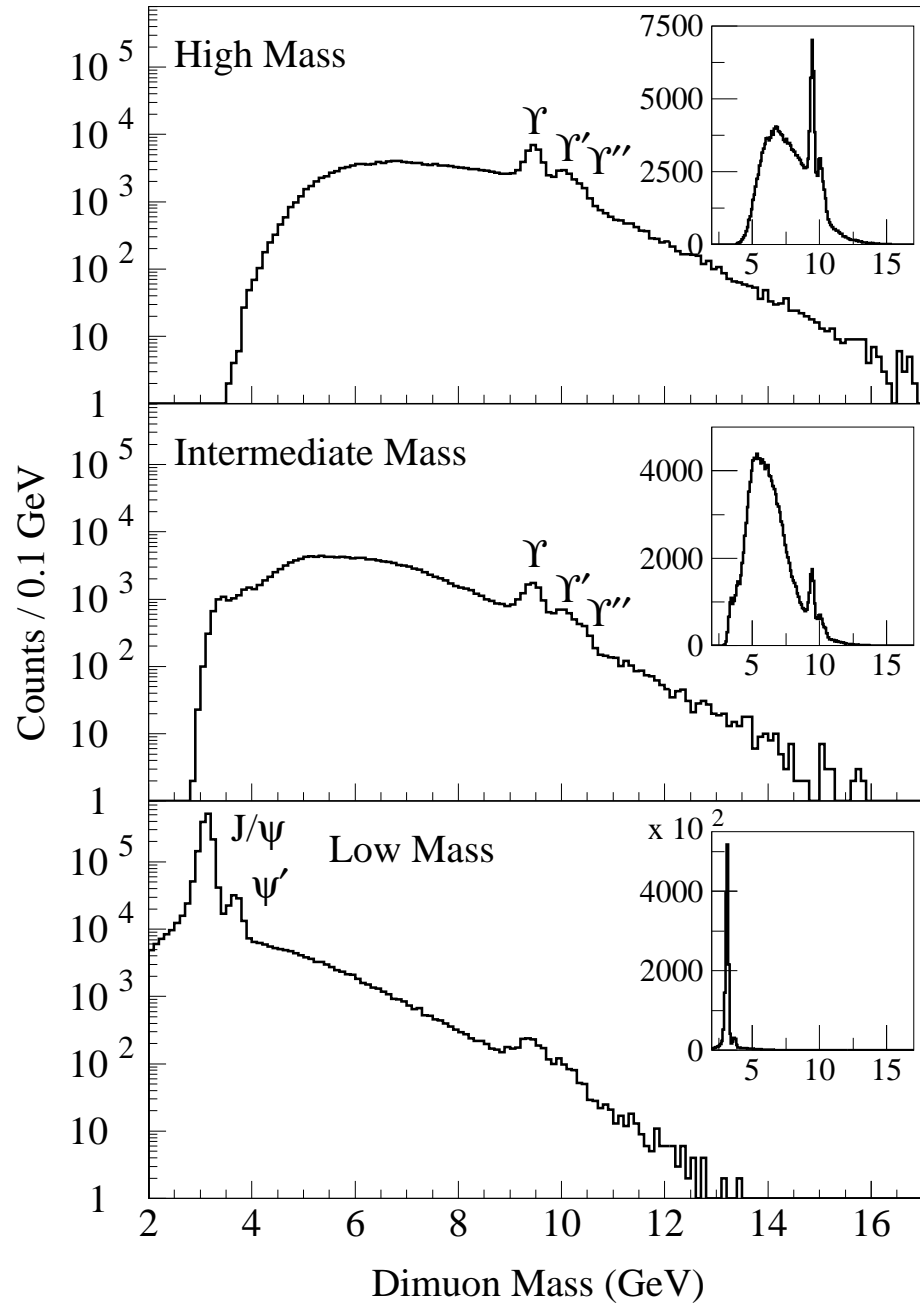


Figure 5.1: The dimuon mass distributions for the three different mass settings. The inset figures are the same spectra shown on a linear scale.

Table 5.1: Summary of the data sets. The size of each data set is shown as the number of Drell-Yan events that passed all data cuts rounded to the nearest thousand. All magnet currents are in amperes. The deuterium fill refers to the quality of the deuterium in the target as described in Section 5.7.

mass setting	data set	Drell-Yan events	SM0 current	SM12 current	deuterium fill
	3	78 K	0	2800 A	first
int.	4	50 K	0	-2800 A	first
	9	17 K	0	2800 A	second
low	5	89 K	-2100 A	2800 A	first
	7	37 K	0	4000 A	first
high	8	80 K	0	4000 A	second
	11	24 K	0	-4000 A	second

larity, beam duty factor, and target purity. Of the eleven data sets recorded, seven contained data that were useful to this analysis. These seven data sets constituted over 90% of all the data based on luminosity and are summarized in Table 5.1.

The four data sets that were not used in the analysis described here were either poor quality data or were not useful to this measurement. Data sets one and two were the first data taken and the beam duty factor was extremely poor. Data sets six and ten are good quality data, but are not useful to this analysis. Data set six was a fourth mass setting that focused the spectrometer acceptance below the J/ψ where other production mechanisms besides Drell-Yan contribute significantly to the continuum. Data set ten was a small data set taken in the low mass setting, but used the deuterium mixture with the slight hydrogen contamination. The decrease in statistical uncertainty gained by including the events from data set ten would be insignificant, while the

hydrogen contamination would increase the systematic uncertainty. Therefore, only the data sets listed in Table 5.1 were used in this analysis.

5.2 First Pass

The first pass analysis of all the data was done on Fermilab's IBM parallel computing UNIX farms. The main analysis code used for both the first and second pass analysis was originally written and used for the E605 experiment. Since then many changes have been made to the code, but the basic algorithm has remained unchanged. Since only about one percent of all the events written to tape reconstructed to form a dimuon event from the target, the purpose of the first pass analysis was to reduce the raw data tapes to DST's.

The analysis code started by running initialization and setup routines for each data run. This ensured that the proper spectrometer settings, such as trigger and magnet maps, were used for the analysis of each run. Each event was then translated from the output format of the DAQ system to a format more suitable for analysis. Once all of these preliminary tasks were completed, the code reconstructed the event. Reconstructing an event is the task of converting a list of drift chamber, hodoscope, and proportional tube hits in the spectrometer to tracks of particles responsible for the hits and finally combining pairs of tracks to form a dimuon event.

The reconstruction process began by looking at the hits in the station two and station three drift chambers. If at least four of the six planes in a station all had a hit which could have been produced by a single particle, this position was considered to be a possible track reconstruction point. Some of these points were eliminated by requiring that the location of the point be

consistent with hits in the hodoscopes that satisfied the trigger. Once all of these points were determined, an iterative process paired a reconstruction point in station two with another point from station three and determined if the track segment generated by connecting the two points could have been produced by a single charged particle originating at the target.

Once all of the possible track segments between stations two and three were determined, they were compared with hits in stations one and four to further reduce the number of tracks. The station two to station three track segment was extended upstream to the SM3 bend plane. Since at this point in the reconstruction process the sign of the electric charge and the momentum of the particle are still unknown, a region of possible station one positions are searched for a possible track reconstruction point. If at least four of the six planes had a hit that could have been produced by a single charged particle in the region identified by extending the station two to station three track segment to station one, then station four hits were checked.

The final check that the candidate track was produced by a muon used the hits at station four. At this point in the reconstruction process, the track extends from station one through SM3 to stations two and three. Since the track went through the magnetic field produced by SM3, the charge and momentum of the particle were determined. The track was extended downstream to station four. The absorbing material between station three and station four ensured that only muons would be detected in the station four detectors. To validate a track, at least three of the five detector planes in station four must have had a hit at the position predicted by the candidate track.

Once the position, charge, and momentum of the particle were known

at station one, the track was extended upstream to the target. Between station one and the target were two dipole magnets, the absorber wall, and the beam dump. The track was reconstructed in a series of small variable length steps, which were typically a few inches long. At each step the particle's trajectory was bent by the magnetic field, and when traveling through the absorber wall or the beam dump, energy was added back to the particle to correct for the energy that was lost while traversing the material. To correct for the multiple scattering that occurred in the material, a single bend plane approximation was used. This correction slightly modified the particle angle at the effective multiple scattering plane to force the track to originate at the average interaction point inside the target.

After the individual tracks were fully reconstructed, they were paired ¹ to reconstruct the dimuon event. From the charge and momentum of the individual tracks, the kinematics of the event were determined.

5.3 Second Pass

Once the data had been reduced by almost two orders of magnitude from the raw data tapes to the data summary tapes, the analysis code was optimized by repeated analysis of the DST's. This second pass analysis was completed on Hewlett Packard workstations. While the basic analysis code was not changed for the second pass analysis, many small changes were made to improve mass resolution and to study systematic effects.

One of the changes that was made to the second pass analysis was the

¹Less than 0.08% of all the good events contained more than 2 tracks.

addition of a small magnetic field in the y-direction inside the aperture of SM12. This was added because the data showed a slight focusing in the x-direction. Another improvement to the second pass analysis was the placement of the effective multiple scattering plane. Previous analyses had used a fixed position, but it was determined that the optimal position depended on how much of the copper beam dump the muon traversed. If the muon passed through the entire beam dump, then the effective multiple scattering plane should be closer to the front of the beam dump. If the muon traveled above or below the beam dump, then the effective multiple scattering plane should be closer to the absorber wall. Therefore, the analysis was improved to track the muon to the front of the dump, and then the position for the effective multiple scattering plane was determined and the muon was retraced using the effective multiple scattering plane. These improvements to the event reconstruction improved the mass resolution.

After the second pass analysis was completed, the final results, along with many intermediate quantities, were stored in large arrays called ntuples [24]. An ntuple is a two dimensional array where one dimension is equal to the number of events and the other dimension contains information from each event. In addition to the event information stored in these ntuples, information was recorded about each beam spill.

5.4 Ntuple Cuts

Once the second pass analysis was completed and ntuples were produced, the data were subjected to a final set of necessary conditions known as ntuple cuts. These cuts were carefully studied to remove bad events from the data,

leaving only good Drell-Yan events. While the reason for these cuts is consistent between data sets, some of the actual values changed between sets of data. This section describes these cuts.

Before actual event cuts were made, the beam spill was required to meet certain criteria. The beam duty factor, the readout live time, and the beam intensity were all required to exceed some minimum value or all of the events from that spill, were cut. These cuts were made primarily to remove events that came from spills with poor beam quality which could introduce additional systematic uncertainties.

Some cuts were made to ensure that the reconstructed individual tracks were good. One cut ensured that the tracks stayed inside of the x aperture of SM12 by making cuts on the track angle at the target in the x direction. Another cut on the y angle of the track at the target prevented tracks with a very small y angle from going on the wrong side of the dump. The last cut on tracks ensured that the reconstructed x and y position at the interaction point was near the center of the target.

The next group of cuts was applied to the reconstructed event. If the sign of the electric charge of the two tracks was not different, the event could not be a Drell-Yan event, so the event was cut. The z value of the uniterated reconstructed interaction point ² of the pair of tracks was required to be near the center of the target. Also the reconstructed event must satisfy the trigger that fired. So if the trigger bits that should have been fired by the reconstructed

²This point was the z position of the closest approach of the two tracks in the y-z plane before the multiple scattering correction was made.

event were not present, the event was cut. Events with too many total hits were cut to put an upper limit on the allowable background noise in an event.

Finally, three cuts were made on the kinematic quantities of the pair. The reconstructed momentum of the dimuon pair must not be greater than the momentum of the incident proton to conserve momentum. Any event that appears to violate the conservation of momentum was cut. Another cut limited the maximum transverse momentum (p_T) of the pair. The final kinematic cut was on the reconstructed dimuon mass. This cut was used to remove the J/ψ and Υ resonance families from the Drell-Yan continuum ³.

In addition to all of the above ntuple cuts, which were made on all three groups of data and summarized in Table 5.2, each data set had some unique ntuple cuts. Most of these cuts removed data not useful for this analysis. The low and high mass data required AMON to have at least one count, and the intermediate mass data required the ratio of the beam intensity as measured by IC3 and SEM to be less than eight.

5.5 Randoms Correction

A background that must be corrected for was the random coincidence of two unrelated oppositely charged muons produced in the target by different protons during the same beam bucket. Since the production mechanism for these dimuons is not the Drell-Yan process, but the random coincidence of two single muons, these events are called randoms. To determine the number and kine-

³The typical mass resolution at the J/ψ was 100 MeV.

Table 5.2: Summary of all ntuple cuts.

ntuple cut	high	int.	low
min beam duty factor	25%	50%	25%
min DAQ livetime	0.9	0.9	0.9
min beam intensity measured by IC3	5000	10000	5000
max magnitude x angle at target	0.026	0.026	0.026
min magnitude y angle at target	0.001	0.001	0.0023
max radial distance from center of target	2.45 in.	2.45 in.	2.45 in.
min z of the uniterated interaction point	-70 in.	-60 in.	-55 in. ^a
max z of the uniterated interaction point	90 in.	75 in.	80 in.
max noise ^b	1300	1400	1400
max dimuon momentum (GeV/c)	800	800	800
max dimuon p_T (GeV/c)	7.0	6.0	6.0
min dimuon mass (GeV)	4.5	4.3	4.0
max mass allowed below Υ (GeV)	9.0	8.8	8.8
min mass allowed above Υ (GeV)	10.7	10.8	none ^c

^aThis value was raised to -50 inches if the dimuon mass was less than 4.5 GeV.

^bThis quantity is twelve times the number of hodoscope hits plus the total event length, measured by the number of six digit octal words in the raw event.

^cNo events above the Υ are included in the low mass data.

matic distribution of these events, two of the specialty triggers described in Section 3.4.1 were used.

The first of these specialty triggers recorded a fraction of the events that appeared to be a single muon from the target. These single muon events were analyzed just like a single track in a dimuon event. Then these single tracks were randomly combined to form a dimuon event. To check the kinematic distribution of these combined singles events and to normalize them so that they could be used to remove random events from the data required the second specialty trigger.

The second specialty trigger was satisfied by two muons from the target area that were of the same sign electric charge and traveled down opposite sides of $x = 0$ in the spectrometer. These events were analyzed like all of the oppositely charged dimuon events once one of the tracks was reflected around $y = 0$. These events, which are a subset of all the random events, provided a standard by which the combined singles events could be normalized.

The data were corrected for random dimuons by subtracting the normalized combined singles events from the dimuon events. Since most of the combined singles events reconstructed to a low effective dimuon mass, the randoms correction was largest in the low mass data and smallest in the high mass data. The average correction for each mass setting is shown in Table 5.3.

5.6 Rate Dependence Correction

The rate dependence correction is made to remove the effect of any inefficiency in our ability to detect and reconstruct events that occurs as a function of

Table 5.3: Size of the randoms correction for each mass setting.

mass setting	percent of random events	average mass of randoms
low	4.1%	4.5 GeV
intermediate	2.9%	5.1 GeV
high	0.2%	5.4 GeV

beam intensity. The primary source of this inefficiency is believed to be lost drift chamber hits due to the single hit TDC's that were used. In simple terms,

$$N_m(s) = N_t(s) \times e(s) \quad (5.1)$$

where s is the beam intensity for the spill, $N_m(s)$ is the number of events that are reconstructed at a given beam intensity, and $N_t(s)$ is the number of true events that actually occurred and would have been accepted at that beam intensity. ($N_t(s)/s$ is actually a constant, independent of beam intensity.) Finally, $e(s)$ is the efficiency for detection and reconstruction as a function of beam intensity.

The drop in reconstruction efficiency as the beam intensity increases can clearly be seen in the low mass data shown in Fig. 5.2. This figure shows that the yield of Drell-Yan events per unit beam intensity decreases as the beam intensity increases. But of even more importance to the measurement of the cross section ratio is the fact that the deuterium events suffer from a larger inefficiency than do the hydrogen events.

In order to correct the data, the reconstruction efficiency as a function of the beam intensity ($e(s)$) must be determined. To determine $e(s)$, fits were made to $N_m(s)/s$ as a function of beam intensity. So that no unfounded as-

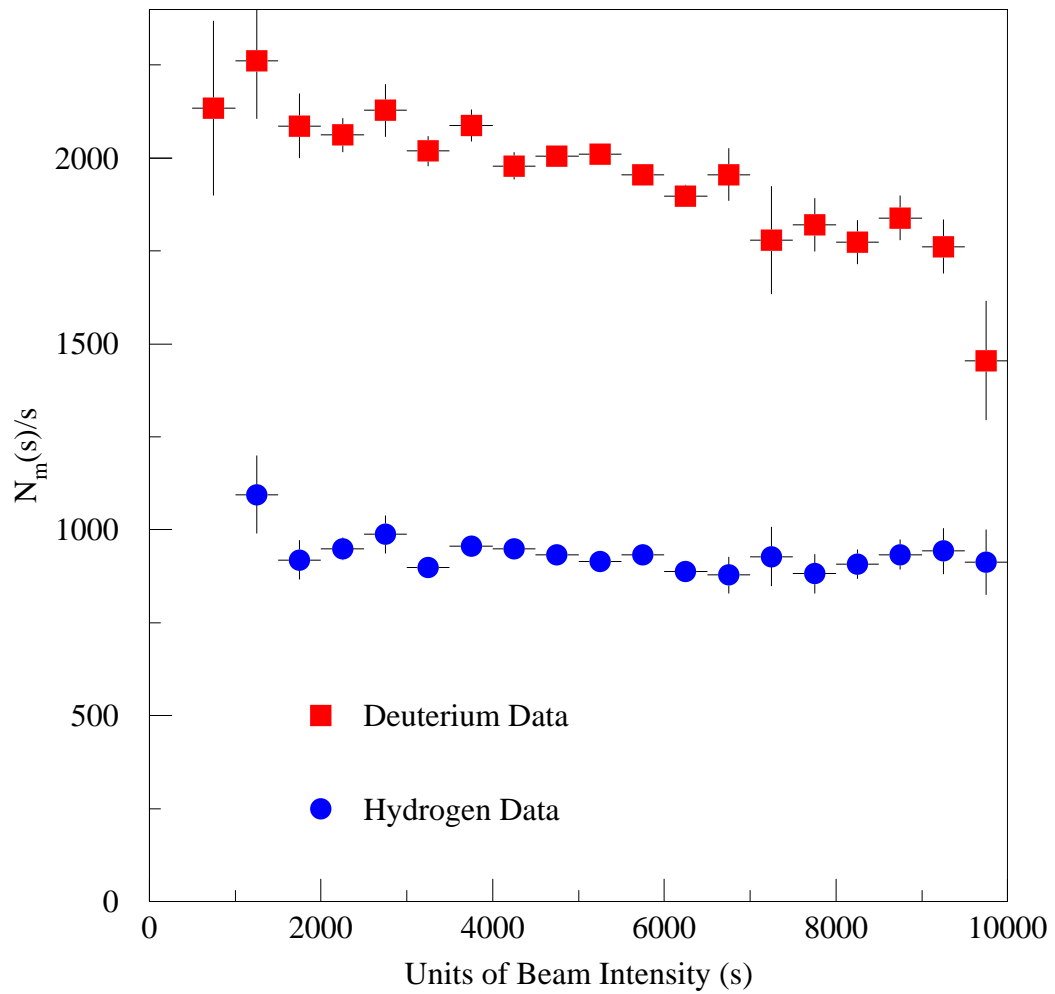


Figure 5.2: The rate dependence problem shown here for the low mass data. The yield of Drell-Yan events per unit of beam intensity is shown versus the beam intensity for both the hydrogen and deuterium events.

sumptions would be made, the functional form of the rate dependence was studied at length.

5.6.1 Functional Form of the Rate Dependence

The data suggest that the reconstruction efficiency drops in a linear manner and this basic assumption was justified by extensive Monte Carlo simulations. The reason that Monte Carlo simulations were necessary is because of the lack of sufficient statistics in the data for this study as well as the need to verify that the functional form was not changing at the limits of our data.

The data were broken into different bins based on beam intensity so that Monte Carlo events could be generated for different beam intensities. For each bin, the noise in the drift chambers was carefully studied. Specifically, the number, position, correlation between planes within a station, and the correlation between stations of the noise hits in the drift chambers were determined. This allowed Monte Carlo events to be generated with the proper background of chamber noise hits for each different bin in beam intensity. In addition to generating Monte Carlo events over the entire range of beam intensity covered by the data, the chamber noise was extrapolated to both higher and lower beam intensities. This ensured that the functional form was valid over the entire range of the data. These Monte Carlo events were then analyzed using the same analysis methods and cuts as the data. The results showed that the reconstruction efficiency did decrease linearly with increasing beam intensity as shown in Fig. 5.3. This Monte Carlo study was performed for both J/ψ and Drell-Yan events with consistent results.

Another concern was that the rate dependence might also be a func-

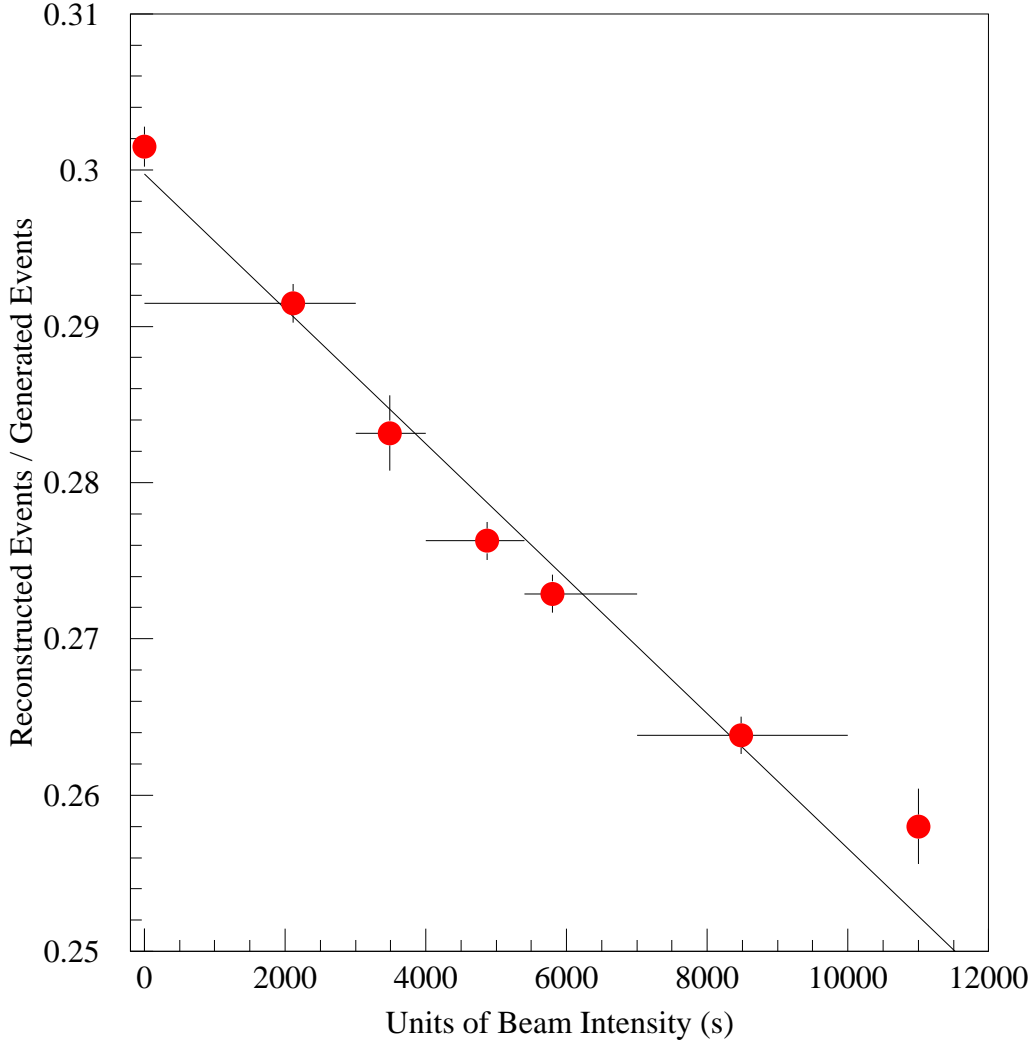


Figure 5.3: Monte Carlo study of the rate dependence. The horizontal error bars indicate where the data were divided into bins of beam intensity. These points are plotted at the average beam intensity within the bin. The highest and lowest points in beam intensity do not have horizontal error bars because there were no data at these beam intensities.

tion of the kinematics of the dimuon event. This potential dependence was searched for in both the data and Monte Carlo events by breaking the events into two or three bins based on the kinematic variable being studied. The rate dependence was then calculated for each bin. These studies were performed for Monte Carlo Drell-Yan events broken into x_2 and mass bins, Monte Carlo J/ψ events broken into p_T and x_F bins, data Drell-Yan events broken into x_2 bins, data J/ψ events broken into x_F bins, and data events broken into mass bins. Despite this extensive search for some kinematical dependence to the rate correction, no dependence was found within the limits of the statistical uncertainty. Therefore, the rate dependence correction was determined to be a linear function dependent only on the beam intensity.

If each data set were treated independently, there would be 28 parameters (a slope and an intercept for each target and for each of seven data sets). However, these parameters are not independent and therefore the number of parameters can be reduced to 16.

The reconstruction efficiency function was determined for each mass setting: high, intermediate, and low. Within each of these mass settings, the intercept of the deuterium data (D_i) and the hydrogen data for each data set (i) was related by a single factor common to all data sets (E). Additionally the relative slopes of the deuterium data from all data sets within a mass setting are the same (R_d). Likewise the hydrogen data share a common relative slope (R_h). This means that for each data set i within a mass setting, the deuterium data can be fit to

$$\frac{N_m^d(s)}{s} = D_i \times (1 + R_d s) \quad (5.2)$$

and the hydrogen to

$$\frac{N_m^h(s)}{s} = D_i E \times (1 + R_h s). \quad (5.3)$$

From these equations and equation 5.1, it is easy to identify the efficiency functions as

$$e_d(s) = 1 + R_d s \quad (5.4)$$

and

$$e_h(s) = 1 + R_h s. \quad (5.5)$$

Figure 5.4 shows the intermediate mass data fit with equations 5.2 and 5.3. The hydrogen data are offset by 90,000 units of beam intensity. Within the hydrogen and deuterium data, data sets three, four, and nine are offset by 0, 30,000 and 60,000 units of beam intensity respectively. This figure shows how the twelve parameters for the intermediate mass data have been reduced to only six. However there remains one more constraint that should be imposed on this fit. The slopes R_d and R_h are correlated. The explanation of this correlation will be discussed in detail in the following subsection.

5.6.2 Relation Between the Rate Dependence in the Two Targets

The unwanted tracks through the spectrometer, which caused us to lose the tracks we want, came from the target or the dump. Obviously when we change the target, the dump does not change. The only change in the events from the dump when we change the target is due to the different fraction of the beam that makes it through the target. When the target is hydrogen, 93% of the incident beam reaches the dump, while only 85% makes it to the dump when

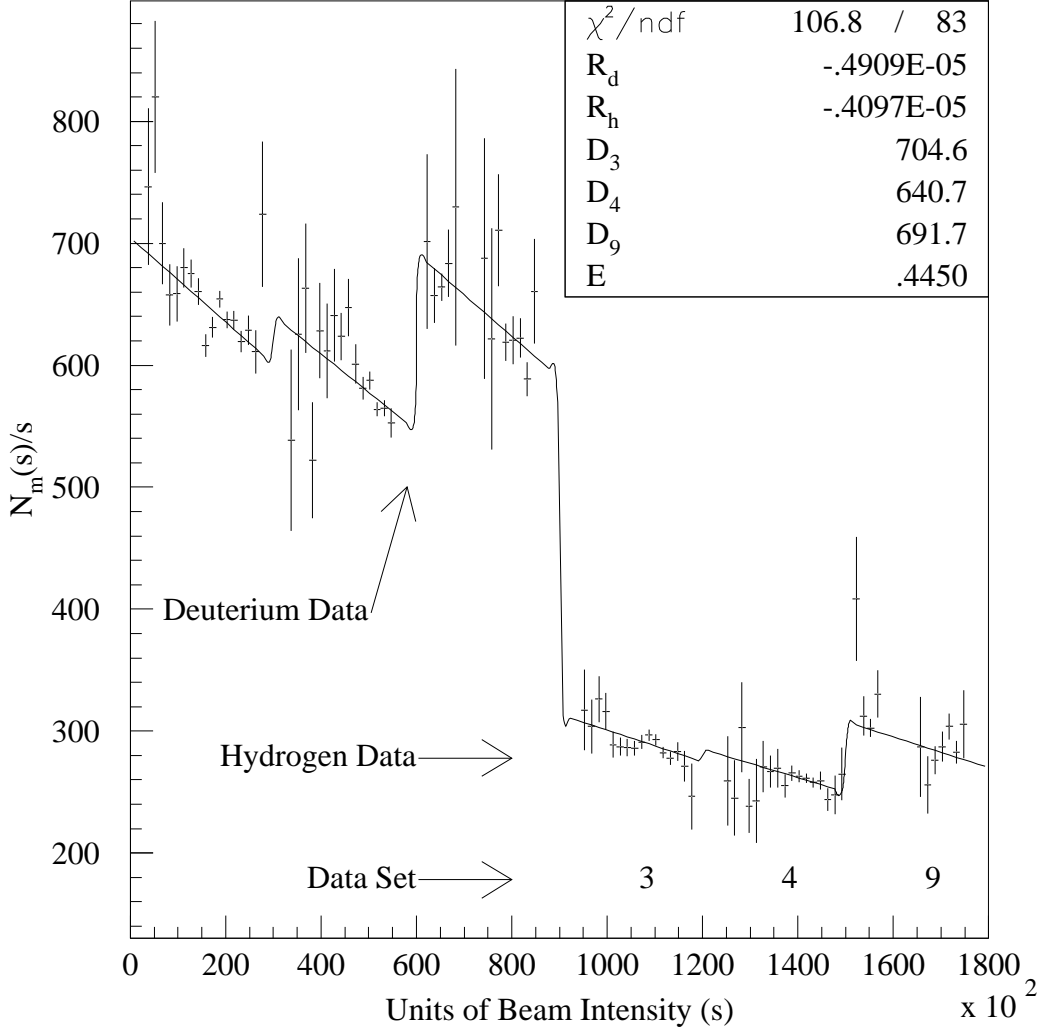


Figure 5.4: Number of deuterium (left) and hydrogen (right) events per unit of beam intensity as a function of the beam intensity. Both the deuterium and hydrogen data for all three of the intermediate mass data sets are shown here. The hydrogen data are offset by 90,000 units of beam intensity. Within the deuterium and hydrogen data, data sets three, four and nine are offset by 0, 30,000 and 60,000 units of beam intensity respectively.

the target is deuterium. Let

$$N_t(s) = A \times s, \quad (5.6)$$

$$e_d(s) = 1 - (0.85B_{\text{dump}} + B_d)s, \quad (5.7)$$

and

$$e_h(s) = 1 - (0.93B_{\text{dump}} + B_h)s. \quad (5.8)$$

Here A is the yield per beam intensity with no rate dependence and B_{dump} , B_d , and B_h are the beam intensity dependent backgrounds that cause us to lose events and originate in the dump, deuterium, and hydrogen respectively.

Then using equation 5.1 yields

$$\frac{N_m^d(s)}{s} = A_d [1 - (0.85B_{\text{dump}} + B_d)s] \quad (5.9)$$

and

$$\frac{N_m^h(s)}{s} = A_h [1 - (0.93B_{\text{dump}} + B_h)s], \quad (5.10)$$

so the relative rate dependence is

$$\frac{N_m^d(s)/s}{2N_m^h(s)/s} = \frac{A_d [1 - (0.85B_{\text{dump}} + B_d)s]}{2A_h [1 - (0.93B_{\text{dump}} + B_h)s]}. \quad (5.11)$$

In the limit that the inefficiency is small (so that $1/(1-x) \approx 1+x$) this reduces to

$$\frac{N_m^d(s)/s}{2N_m^h(s)/s} = \frac{A_d}{2A_h} [1 + (0.08B_{\text{dump}} + B_h - B_d)s]. \quad (5.12)$$

Since the acceptance is approximately the same for both hydrogen and deuterium, $B_d = 2.13 \times B_h$, where the factor of 2.13 is the ratio of interaction lengths for the deuterium and hydrogen targets. If the acceptance for dump events was the same as for target events, then $B_d = 2.13 \times B_h = .15 \times B_{\text{dump}}$

and the rate dependence vanishes as it should. However, since the acceptance is not the same for target and dump events, there is a rate dependence that must be corrected.

It should be noted that the important quantity is not the absolute rate dependence inefficiency, but rather the difference between the inefficiencies for the two different targets. A simple way of approximating the size of the correction to the cross section ratio (C) is to compare it to the absolute correction for deuterium events which is,

$$\frac{C \times s}{R_d \times s} = \frac{C}{R_d} = \frac{0.08B_{\text{dump}} + -0.53B_d}{-0.85B_{\text{dump}} - B_d}. \quad (5.13)$$

This equation shows that the rate dependence correction to the cross section ratio is considerably smaller than the absolute correction in the deuterium events.

The ratio of extra drift chamber hits in an average deuterium event compared to the same number in an average hydrogen event (F) can be determined from the data for each mass setting. This ratio should be the same as the ratio of the average number of background hits in a deuterium event to the average number of background hits in a hydrogen event. So

$$F = \frac{0.85B_{\text{dump}} + B_d}{0.93B_{\text{dump}} + B_h}. \quad (5.14)$$

Comparing equations 5.4 and 5.5 with equations 5.7 and 5.8, clearly indicates that

$$\frac{0.85B_{\text{dump}} + B_d}{0.93B_{\text{dump}} + B_h} = \frac{R_d}{R_h}. \quad (5.15)$$

This means that

$$F = \frac{R_d}{R_h}. \quad (5.16)$$

So the number of independent parameters introduced to fit $N_m(s)/s$, has been reduced again. The only difficulty that eliminating R_h from the fit introduces is the determination of F from the data. This is the subject of the next section.

5.6.3 Determination of F

The previous section explained why the determination of F was important. This section will expound on how F was determined. Start by defining F to be

$$F \equiv \frac{\text{extra drift chamber hits in an average deuterium event}}{\text{extra drift chamber hits in an average hydrogen event}}. \quad (5.17)$$

Here ‘extra’ means that the drift chamber hits produced by the reconstructed dimuon event will not be included. The numerator (denominator) is merely the average multiplicity of a drift chamber minus the number of hits from the reconstructed dimuon in a deuterium (hydrogen) event. The number of hits from the reconstructed dimuon is two times the chamber efficiency.

Since there are eighteen drift chambers, F can be determined eighteen times for each of the three mass settings. The six calculated values of F for each station of drift chambers for each mass setting are very similar. However, there are differences between stations and mass settings as shown in Table 5.4. The F values shown in Table 5.4 have been averaged over each station and the uncertainty is the standard deviation of these six measurements.

While the variation of F between mass settings is to be expected, the reason for the variation of F between stations is less clear. Monte Carlo generated events were used to determine which station’s extra hits affected the rate dependence the most. By turning off the noise in one station at a time,

Table 5.4: Calculated F values for each station and each mass setting.

mass setting	station		
	one	two	three
low	1.83 ± 0.023	1.65 ± 0.034	1.83 ± 0.013
intermediate	1.11 ± 0.014	1.07 ± 0.020	1.26 ± 0.011
high	1.49 ± 0.015	1.42 ± 0.017	1.56 ± 0.022

Table 5.5: Calculated F values for each mass setting obtained by taking a weighted average over all three stations.

mass setting	F
low	1.78 ± 0.10
intermediate	1.18 ± 0.10
high	1.51 ± 0.10

it was determined that station three contributed the most to the rate dependence while station one contributed the least. The relative magnitudes of the effect on the rate dependence from station one to station two to station three is 36:73:135. Based on this relationship, a weighted average over the stations produced the final F values shown in Table 5.5. The uncertainty on F is a conservative estimate based primarily on the magnitude of the variation of F between stations.

Once F was determined for each of the mass settings, the deuterium data were fit to

$$\frac{N_m^d(s)}{s} = D_i \times (1 + R_d s) \quad (5.18)$$

and the hydrogen data were fit to

$$\frac{N_m^h(s)}{s} = D_i E \times \left(1 + \frac{R_d}{F} s\right). \quad (5.19)$$

Table 5.6: Correction to $\sigma^{pd}/2\sigma^{pp}$ due to the rate dependence.

mass setting	percent correction to $\sigma^{pd}/2\sigma^{pp}$
low	$5.45\% \pm 0.82\%$
intermediate	$1.06\% \pm 0.89\%$
high	$1.76\% \pm 0.69\%$

These fits to the high, intermediate, and low mass data are shown in Fig. 5.5, 5.6, and 5.7 respectively. From these fits the data can be corrected for the rate dependence by weighting each deuterium event by

$$\frac{1}{e_d(s)} = \frac{1}{1 + R_d s} \quad (5.20)$$

and each hydrogen event by

$$\frac{1}{e_h(s)} = \frac{1}{1 + \frac{R_d}{F} s}. \quad (5.21)$$

The final correction to $\sigma^{pd}/2\sigma^{pp}$ due to the rate dependence is summarized in Table 5.6.

5.7 Target Composition, Density, and Attenuation

Since the data included in this analysis were taken over a period of five months, there were several small but important changes to the target composition and density. These changes and their effect on the calculation of the cross section ratio will be discussed in this section.

The deuterium target was filled twice during the acquisition of these data. Both of the deuterium mixtures that were used to fill the target were analyzed for contaminations. The analysis of the first fill indicated that the

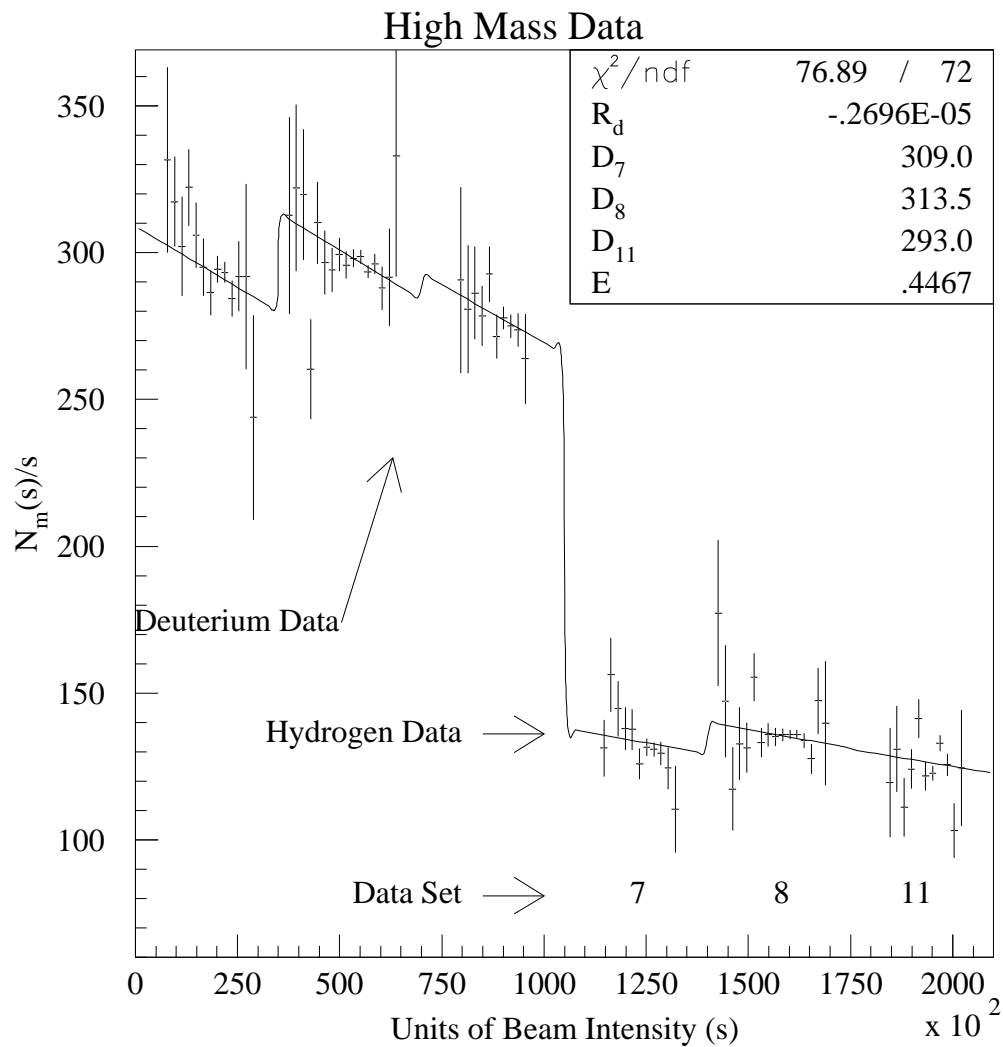


Figure 5.5: Number of deuterium (left) and hydrogen (right) events per unit of beam intensity as a function of the beam intensity. Both the deuterium and hydrogen data for all three of the high mass data sets are shown here. The hydrogen data are offset by 105,000 units of beam intensity. Within the deuterium and hydrogen data, data sets three, four and nine are offset by 0, 35,000 and 70,000 units of beam intensity respectively.

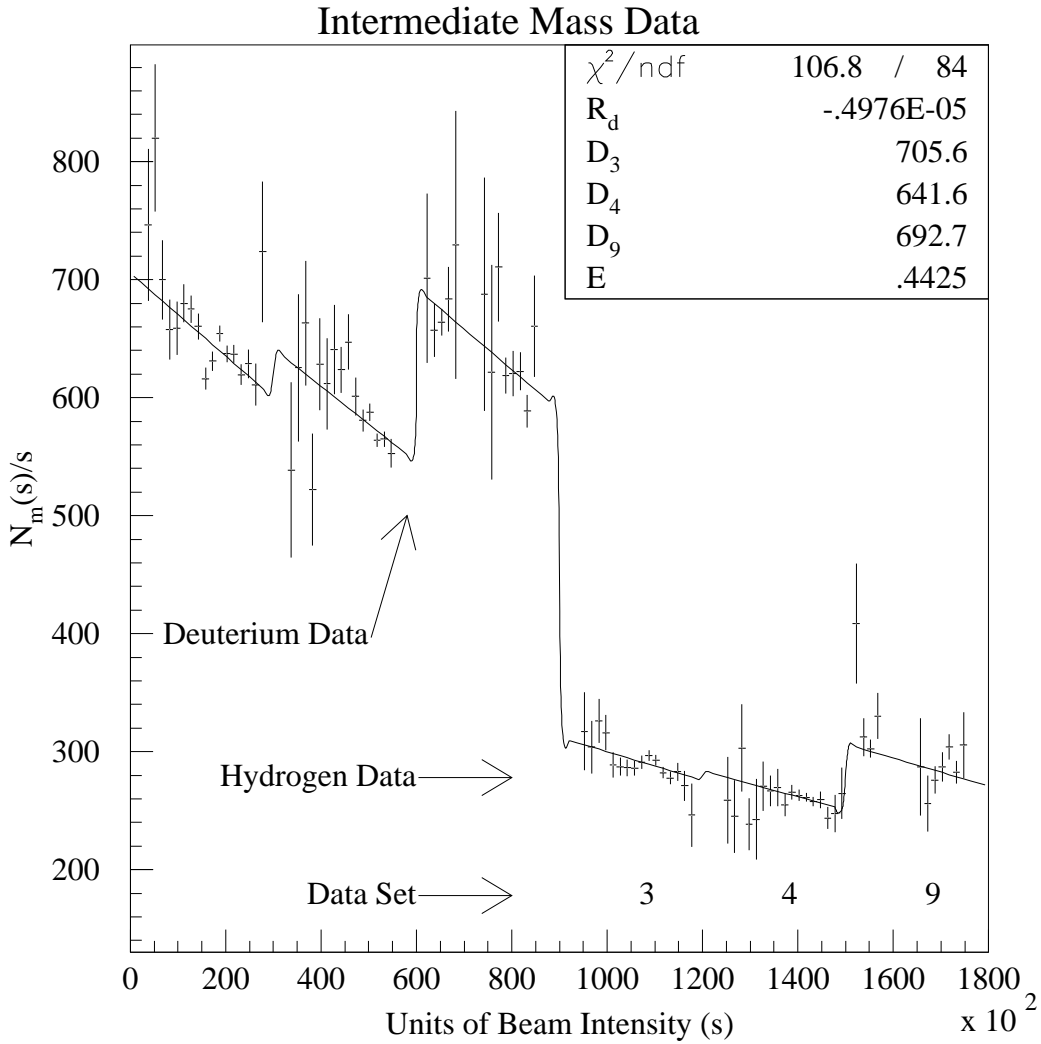


Figure 5.6: Number of deuterium (left) and hydrogen (right) events per unit of beam intensity as a function of the beam intensity. Both the deuterium and hydrogen data for all three of the intermediate mass data sets are shown here. The hydrogen data are offset by 90,000 units of beam intensity. Within the deuterium and hydrogen data, data sets three, four and nine are offset by 0, 30,000 and 60,000 units of beam intensity respectively.

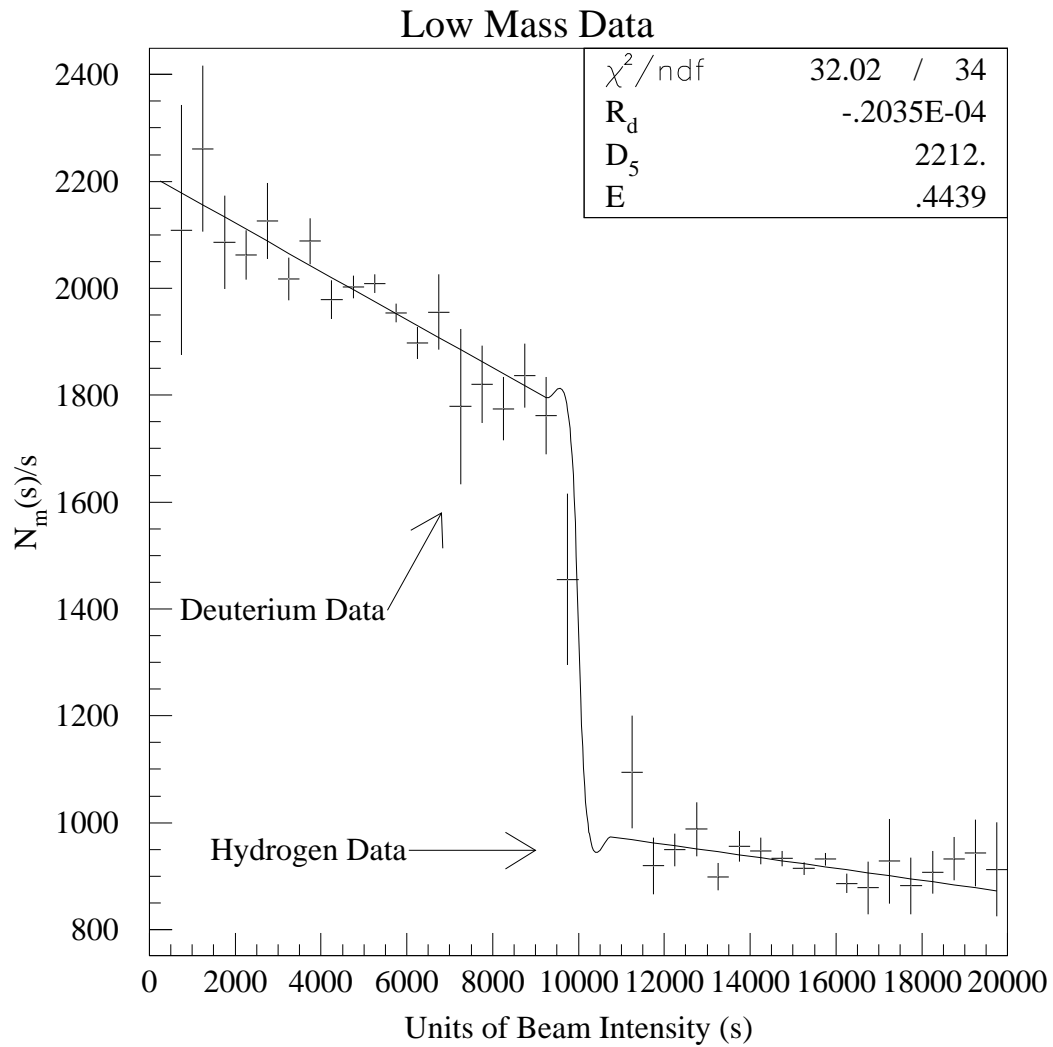


Figure 5.7: Number of deuterium (left) and hydrogen (right) events per unit of beam intensity as a function of the beam intensity. Both the deuterium and hydrogen data from the low mass data set are shown here. The hydrogen data are offset by 10,000 units of beam intensity.

Table 5.7: Results of the gas analyses of the second fill of the deuterium target. The results shown are in percent volume.

material	target sample	storage sample
D ₂	93.8% ± 0.7%	92.7% ± 0.8%
HD	5.80% ± 0.58%	6.89% ± 0.69%
H ₂	0.053% ± 0.011%	0.147% ± 0.015%
N ₂	0.327% ± 0.033%	0.245% ± 0.024%
Ar	0.003% ± 0.002%	—
CO ₂	0.006% ± 0.003%	0.0039% ± 0.0008%

deuterium was 99.99% pure. The second fill was of slightly lesser quality and was therefore analyzed twice. The first sample of the second fill was taken directly from the storage flask, while the second sample was taken half way through the process of emptying the target flask. The analyses of both samples of the second fill are shown in Table 5.7.

All samples were taken when the deuterium was in a gaseous state so the analyses are not a perfect indication of what was present in the target where the deuterium was in a liquid state. As the deuterium was cooled, the heavier components (Ar, CO₂, and N₂) should have frozen out of the liquid while the lighter components (H₂ and HD) should have been somewhat distilled out of the liquid into the gas above the liquid in the cryogenic system. Another concern when interpreting the information in Table 5.7 is which of the samples better represents what was in the target. Considering how and when the samples were taken, the sample taken while emptying the flask should be more accurate. Based on these considerations, Table 5.8 shows the best estimate of the second fill deuterium composition.

The density of the target material was determined from the vapor pres-

Table 5.8: Best estimate of the composition of the second fill deuterium. The results shown are in percent volume.

material	percent volume
D ₂	94.05% ± 0.6%
HD	5.90% ± 0.6%
H ₂	0.05% ± 0.01%
deuterium	97.0% ± 0.6%
hydrogen	3.0% ± 0.6%

Table 5.9: Average pressure in psi of each liquid target for each data set.

data set	hydrogen	deuterium
3	15.12 psi	15.06 psi
4	15.05 psi	14.92 psi
5	14.97 psi	14.92 psi
7	15.04 psi	14.96 psi
8	15.11 psi	15.17 psi
11	15.15 psi	15.21 psi

sure of the gas above the liquid in both cryogenic systems. These pressures were constantly monitored and recorded in a database. They were also manually checked at least twice a day and recorded during the standard shift check. Also recorded during the shift check was the temperature of each flask. From these shift checks, the average pressure was determined for each target and for each data set. These average pressures are shown in Table 5.9.

Cryogenic data Tables [25] for hydrogen and deuterium were used to convert vapor pressure to mass density. For liquid H₂, the relationship between vapor pressure (P in psi) and density (ρ_h in g/cm³) is

$$\frac{1}{\rho_h} = 62.473 \left(0.2115 + 1.171 \times 10^{-3}P - 1.109 \times 10^{-5}P^2 \right). \quad (5.22)$$

Table 5.10: Density in g/cm³ for each liquid target and for each data set.

data set	hydrogen	deuterium
3	0.07062 g/cm ³	0.16272 g/cm ³
4	0.07064 g/cm ³	0.16280 g/cm ³
5	0.07066 g/cm ³	0.16280 g/cm ³
7	0.07064 g/cm ³	0.16278 g/cm ³
8	0.07062 g/cm ³	0.16265 g/cm ³
11	0.07061 g/cm ³	0.16259 g/cm ³

The formula used to determine the density of deuterium (ρ_d) is

$$\rho_d = 4.028 \times 10^{-3} \left[43.291 - 3.4176 \frac{P}{14.6959} + 0.5783 \left(\frac{P}{14.6959} \right)^2 \right]. \quad (5.23)$$

From the pressures listed in Table 5.9 and the above equations, the densities shown in Table 5.10 were calculated.

As the beam interacted with the target material, the beam was attenuated. Because the hydrogen and deuterium targets had different densities, they also suffered from different amounts of attenuation. Because the deuterium target was more dense, the protons in the beam were more likely to interact as they traveled through the target. Therefore, the beam intensity decreased more rapidly as it passed through the deuterium target than when it passed through the hydrogen target. This means that there was a smaller fraction of the protons in the beam that reached the downstream end of the deuterium target than there was that reached the downstream end of the hydrogen target. Calculations based on the proton-proton and proton-deuteron cross sections [26] determined that the ratio of effective luminosity in the hydrogen target (A_h) compared to the effective luminosity in the deuterium target (A_d) is

$$\frac{A_h}{A_d} = 1.042 \pm 0.002. \quad (5.24)$$

The acceptance for the events from the hydrogen and deuterium targets was not identical. Although the target flask construction was identical, the attenuation of the beam through the targets meant that the average interaction point for the two targets was slightly different. The average interaction point in the deuterium target was almost 0.2 inches upstream of the average interaction point in the hydrogen target.

Monte Carlo studies were performed to study the effect of beam attenuation through the target on the acceptance. These studies showed a slight x_2 dependence to the acceptance correction, which was most important at the edges of the acceptance. The maximum size of this correction was about one percent at the highest x_2 data points in the low and intermediate mass data. The typical correction was an order of magnitude smaller.

5.8 Calculation of $\sigma^{pd}/2\sigma^{pp}$

This experiment counted the number of dimuon events from the hydrogen target (N_h), the deuterium target (N_d) and the empty target (N_e). To compare the yields from these different targets, the beam intensity for each spill was recorded and the integrated beam intensity (I_{target}) for each target was determined. Using the many small corrections already described in this chapter, the number of raw hydrogen dimuon events is

$$N_h = I_h A_h t_h \rho_h \frac{H}{g} \frac{d\sigma^{pp}}{d\Omega} \Delta\Omega_h e_h + N_h^{BG}, \quad (5.25)$$

and the number of raw deuterium events is

$$N_d = I_d A_d t_d \rho_d \frac{D}{g} \frac{d\sigma^{pd}}{d\Omega} \Delta\Omega_d e_d + N_d^{BG}. \quad (5.26)$$

In the previous two equations t_{target} is the target length, H/g (D/g) is the number of hydrogen (deuterium) atoms per gram, $\Delta\Omega_{\text{target}}$ is the spectrometer acceptance for a given target, and N_{target}^{BG} is the number of background events from a given target. Using these equations, it is easy to get

$$\frac{\sigma^{pd}}{2\sigma^{pp}} = \frac{1}{2} \frac{N_d - N_d^{BG}}{N_h - N_h^{BG}} \frac{I_h A_h t_h \rho_h H/g \Delta\Omega_h e_h}{I_d A_d t_d \rho_d D/g \Delta\Omega_d e_d}. \quad (5.27)$$

The number of background events is the sum of two separate production mechanisms. There were background Drell-Yan events produced when the beam interacted with the target flask windows or other non-target materials. The number of these events was determined by normalizing the yields off of the empty target. To properly normalize the number of empty target events from downstream of the center of the target, attenuation of the beam through the target must be included. The second source of background events are the randoms ($N_{\text{target}}^{\text{randoms}}$) that were described in Section 5.5. Combining these two sources of background events gives

$$N_h^{BG} = \left(N_e^{\text{upstream}} + 0.93 * N_e^{\text{downstream}} \right) \frac{I_h}{I_e} + N_h^{\text{randoms}} \quad (5.28)$$

for the hydrogen target background and

$$N_d^{BG} = \left(N_e^{\text{upstream}} + 0.85 * N_e^{\text{downstream}} \right) \frac{I_d}{I_e} + N_d^{\text{randoms}} \quad (5.29)$$

for the deuterium target background. In the previous two equations the superscript on N_e designates whether the empty target event originated from upstream or downstream of the center of the target.

The output of the second pass analysis was subjected to the final set of cuts described in Section 5.4. The events that passed this final set of cuts were

Table 5.11: The cross section ratio calculated for each data set of the high mass setting and the final high mass result for each x_2 bin. The uncertainty shown here is the statistical uncertainty.

x_2 range min-max	$\sigma^{pd}/2\sigma^{pp}$			
	data set 7	data set 8	data set 11	final result
0.020-0.045	1.044 ± 0.033	1.053 ± 0.022	1.045 ± 0.042	1.049 ± 0.017
0.045-0.070	1.061 ± 0.024	1.104 ± 0.018	1.086 ± 0.032	1.088 ± 0.013
0.070-0.095	1.123 ± 0.030	1.114 ± 0.020	1.149 ± 0.039	1.122 ± 0.016
0.095-0.120	1.114 ± 0.039	1.167 ± 0.028	1.113 ± 0.048	1.142 ± 0.021
0.120-0.145	1.182 ± 0.053	1.219 ± 0.040	1.203 ± 0.071	1.205 ± 0.029
0.145-0.170	1.143 ± 0.069	1.132 ± 0.047	1.128 ± 0.081	1.134 ± 0.035
0.170-0.195	1.117 ± 0.083	1.142 ± 0.060	0.981 ± 0.091	1.100 ± 0.043
0.195-0.220	1.090 ± 0.101	1.207 ± 0.083	0.954 ± 0.111	1.108 ± 0.056
0.220-0.245	0.980 ± 0.126	1.070 ± 0.087	1.241 ± 0.196	1.065 ± 0.067
0.245-0.295	0.826 ± 0.102	1.110 ± 0.104	1.022 ± 0.173	0.974 ± 0.067
0.295-0.345	0.843 ± 0.277	0.873 ± 0.179	1.251 ± 0.448	0.903 ± 0.143

used with the corrections discussed in this chapter and the above equations⁴ to determine $\sigma^{pd}/2\sigma^{pp}$ as a function of x of the target parton. These results are shown in Tables 5.11, 5.12, and 5.13. The results shown for the high mass data are slightly different than the results first published in reference [27] due to improvements made to the rate dependence and acceptance calculations. The average value of x_2 , x_F , p_T , and dimuon mass are shown for each x_2 bin for the high, intermediate, and low mass settings in Tables 5.14, 5.15, and 5.13 respectively.

The intermediate and high mass data were divided into different data sets. The cross section ratio ($r_i \pm \delta_i$) determined from each data set (i) within

⁴ Equation 5.27 was modified for data sets eight and eleven to include corrections needed to account for the small hydrogen content in the deuterium target. Details can be found in reference [21].

Table 5.12: The cross section ratio calculated for each data set of the intermediate mass setting and the final intermediate mass result for each x_2 bin. The uncertainty shown here is the statistical uncertainty.

x_2 range min-max	$\sigma^{pd}/2\sigma^{pp}$		
	data set 3	data set 4	final result
0.015-0.040	1.038 ± 0.031	1.047 ± 0.039	1.042 ± 0.024
0.040-0.065	1.080 ± 0.019	1.066 ± 0.023	1.074 ± 0.015
0.065-0.090	1.090 ± 0.020	1.068 ± 0.024	1.081 ± 0.015
0.090-0.115	1.095 ± 0.025	1.068 ± 0.029	1.084 ± 0.019
0.115-0.140	1.114 ± 0.034	1.161 ± 0.042	1.132 ± 0.026
0.140-0.190	1.118 ± 0.038	1.114 ± 0.045	1.116 ± 0.029
0.190-0.240	1.019 ± 0.072	1.109 ± 0.104	1.048 ± 0.059
0.240-0.290	1.267 ± 0.405	0.755 ± 0.196	0.852 ± 0.176

Table 5.13: The cross section ratio calculated from the low mass setting data for each x_2 bin. The uncertainty shown here is the statistical uncertainty. The average values for kinematic variables is also shown.

x_2 range min-max	$\langle x_2 \rangle$		$\langle p_T \rangle$	$\langle M_{\mu^+\mu^-} \rangle$	$\sigma^{pd}/2\sigma^{pp}$
	$\langle x_2 \rangle$	$\langle x_F \rangle$	(GeV/c)	(GeV/c ²)	
0.015-0.040	0.032	0.415	1.02	4.5	1.053 ± 0.018
0.040-0.065	0.052	0.280	1.07	5.0	1.107 ± 0.015
0.065-0.090	0.076	0.221	1.07	5.7	1.099 ± 0.020
0.090-0.115	0.100	0.174	1.05	6.3	1.148 ± 0.034
0.115-0.165	0.129	0.129	1.06	7.0	1.108 ± 0.055

Table 5.14: The average values for kinematic variables in the high mass data for each x_2 bin. The uncertainty shown here for the cross section ratio is the statistical uncertainty.

x_2 range min-max	$\langle x_2 \rangle$	$\langle x_F \rangle$	$\langle p_T \rangle$ (GeV/c)	$\langle M_{\mu^+\mu^-} \rangle$ (GeV/c ²)	$\sigma^{pd}/2\sigma^{pp}$
0.020-0.045	0.036	0.537	0.92	5.5	1.049 ± 0.017
0.045-0.070	0.057	0.441	1.03	6.5	1.088 ± 0.013
0.070-0.095	0.082	0.369	1.13	7.4	1.122 ± 0.016
0.095-0.120	0.106	0.294	1.18	7.9	1.142 ± 0.021
0.120-0.145	0.131	0.244	1.21	8.5	1.205 ± 0.029
0.145-0.170	0.156	0.220	1.21	9.3	1.134 ± 0.035
0.170-0.195	0.182	0.192	1.20	9.9	1.100 ± 0.043
0.195-0.220	0.207	0.166	1.19	10.6	1.108 ± 0.056
0.220-0.245	0.231	0.134	1.18	11.1	1.065 ± 0.067
0.245-0.295	0.264	0.097	1.18	11.8	0.974 ± 0.067
0.295-0.345	0.312	0.052	1.14	12.8	0.903 ± 0.142

Table 5.15: The average values for kinematic variables in the intermediate mass data for each x_2 bin. The uncertainty shown here for the cross section ratio is the statistical uncertainty.

x_2 range min-max	$\langle x_2 \rangle$	$\langle x_F \rangle$	$\langle p_T \rangle$ (GeV/c)	$\langle M_{\mu^+\mu^-} \rangle$ (GeV/c ²)	$\sigma^{pd}/2\sigma^{pp}$
0.015-0.040	0.034	0.427	1.21	4.8	1.042 ± 0.024
0.040-0.065	0.053	0.331	1.16	5.5	1.074 ± 0.015
0.065-0.090	0.077	0.277	1.14	6.3	1.081 ± 0.015
0.090-0.115	0.101	0.221	1.15	6.9	1.084 ± 0.019
0.115-0.140	0.126	0.163	1.15	7.4	1.132 ± 0.026
0.140-0.190	0.159	0.111	1.09	7.9	1.116 ± 0.029
0.190-0.240	0.207	0.071	1.06	9.1	1.048 ± 0.059
0.240-0.290	0.254	0.145	1.17	12.0	0.852 ± 0.176

a mass setting, were combined to give an average cross section ratio for the mass setting ($R \pm \Delta$) using

$$R \pm \Delta = \frac{\sum_i r_i / \delta_i^2}{\sum_i 1 / \delta_i^2} \pm \left[\frac{1}{\sum_i 1 / \delta_i^2} \right]^{1/2}. \quad (5.30)$$

The results obtained from this equation are shown in the ‘final result’ column of Table 5.11 and Table 5.12. The final cross section ratio as determined by each mass setting is shown in Fig. 5.8. Equation 5.30 can also be applied to the final results of each mass setting to produce a single cross section ratio for all data sets. This result is shown in Fig. 5.9. The average value of x_2 , x_1 , p_T , and dimuon mass are shown along with the cross section ratio for each x_2 bin for the combined result in Table 5.16.

The cross section ratio can also be determined as a function of other kinematic quantities. Figure 5.10 shows the cross section ratio as a function of the transverse momentum of the dileptons.

5.9 Systematic Uncertainty in $\sigma^{pd}/2\sigma^{pp}$

Many of the possible sources of systematic errors in calculating the cross section can be ignored when calculating the cross section ratio. So the only sources of systematic uncertainty that must be considered are sources that affect the two targets differently. Because the targets were changed every few minutes, effects such as changes in detector efficiency or beam quality will affect both groups of data equally.

The sources of systematic uncertainty that can not be neglected include the rate dependence, length of the target flask, target composition, beam atten-

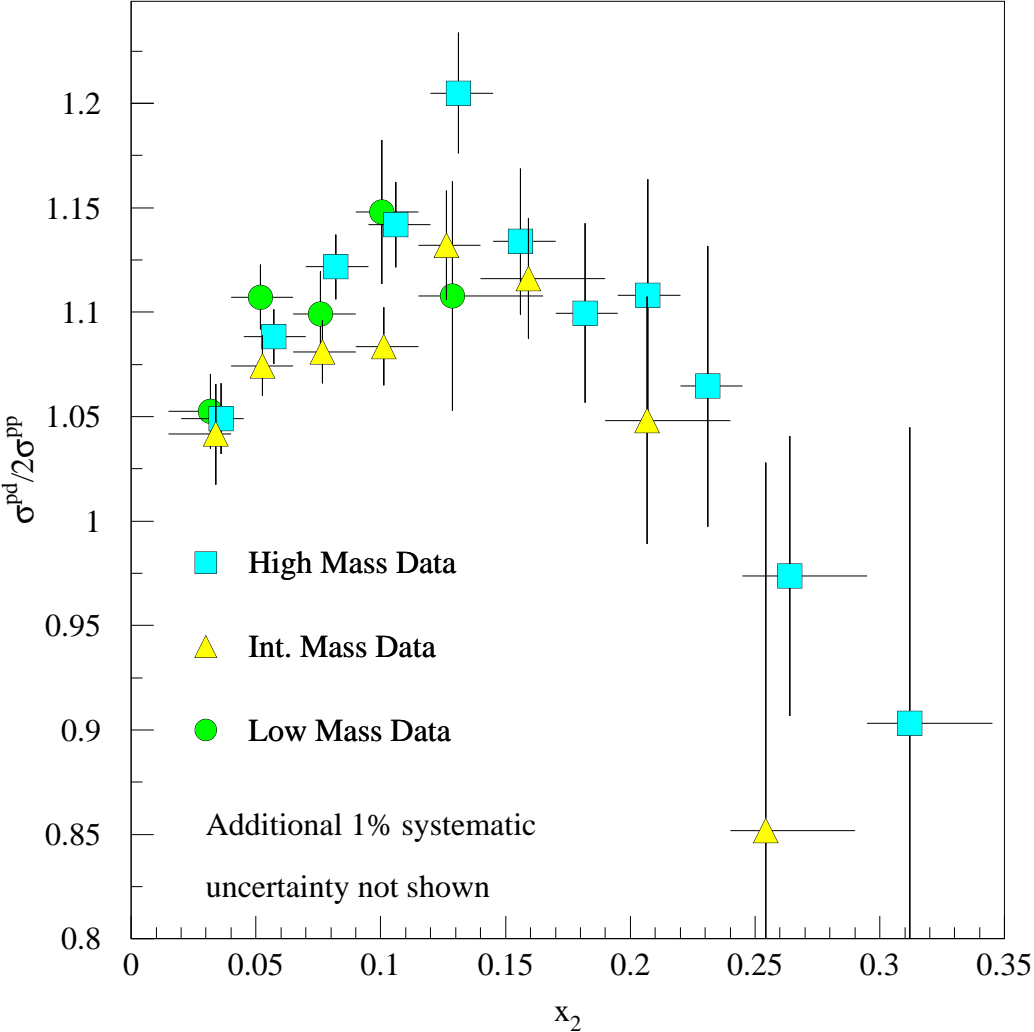


Figure 5.8: The Drell-Yan cross section ratio versus x of the target parton. The results from all three mass settings are shown. The error bars represent the statistical uncertainty. An additional one percent systematic uncertainty is common to all points within a mass setting.

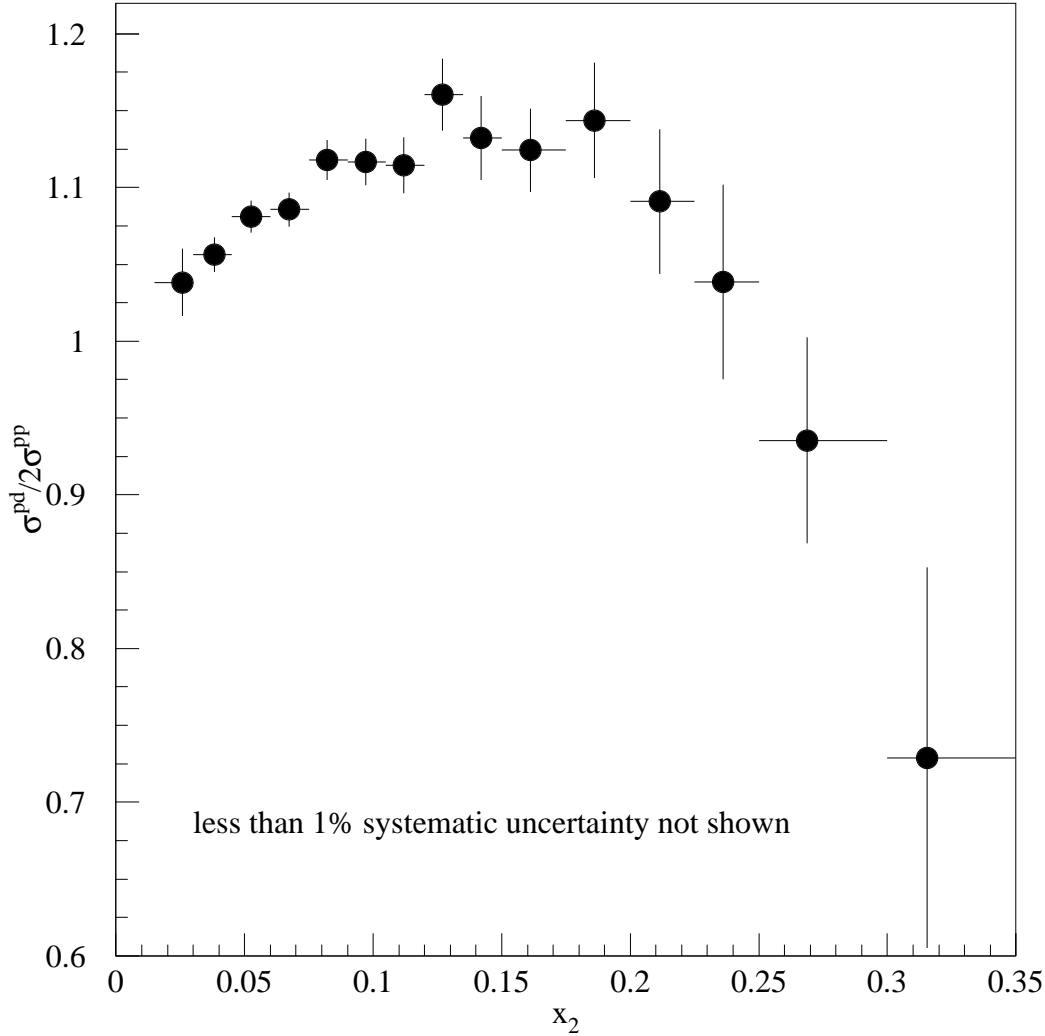


Figure 5.9: The Drell-Yan cross section ratio versus x of the target parton. The combined result from all data sets is shown. The error bars represent the statistical uncertainty. There is a less than one percent systematic uncertainty common to all points.

Table 5.16: The cross section ratio calculated from all data sets for each x_2 bin. The uncertainty shown here is the statistical uncertainty. The average values for kinematic variables is also shown.

x_2 range min-max	$\langle x_2 \rangle$	$\langle x_1 \rangle$	$\langle p_T \rangle$ (GeV/c)	$\langle M_{\mu^+\mu^-} \rangle$ (GeV/c ²)	$\sigma^{pd}/2\sigma^{pp}$
0.015-0.030	0.026	0.559	1.00	4.6	1.038 ± 0.022
0.030-0.045	0.038	0.454	1.05	5.1	1.056 ± 0.011
0.045-0.060	0.052	0.408	1.08	5.6	1.081 ± 0.010
0.060-0.075	0.067	0.393	1.10	6.2	1.086 ± 0.011
0.075-0.090	0.082	0.378	1.12	6.8	1.118 ± 0.013
0.090-0.105	0.097	0.358	1.14	7.2	1.116 ± 0.015
0.105-0.120	0.112	0.339	1.16	7.5	1.115 ± 0.018
0.120-0.135	0.127	0.326	1.17	7.8	1.161 ± 0.023
0.135-0.150	0.142	0.324	1.16	8.2	1.132 ± 0.027
0.150-0.175	0.161	0.325	1.16	8.7	1.124 ± 0.027
0.175-0.200	0.186	0.333	1.15	9.5	1.144 ± 0.038
0.200-0.225	0.211	0.345	1.15	10.3	1.091 ± 0.047
0.225-0.250	0.236	0.356	1.18	11.1	1.039 ± 0.063
0.250-0.300	0.269	0.366	1.18	12.0	0.935 ± 0.067
0.300-0.350	0.315	0.361	1.08	12.9	0.729 ± 0.124

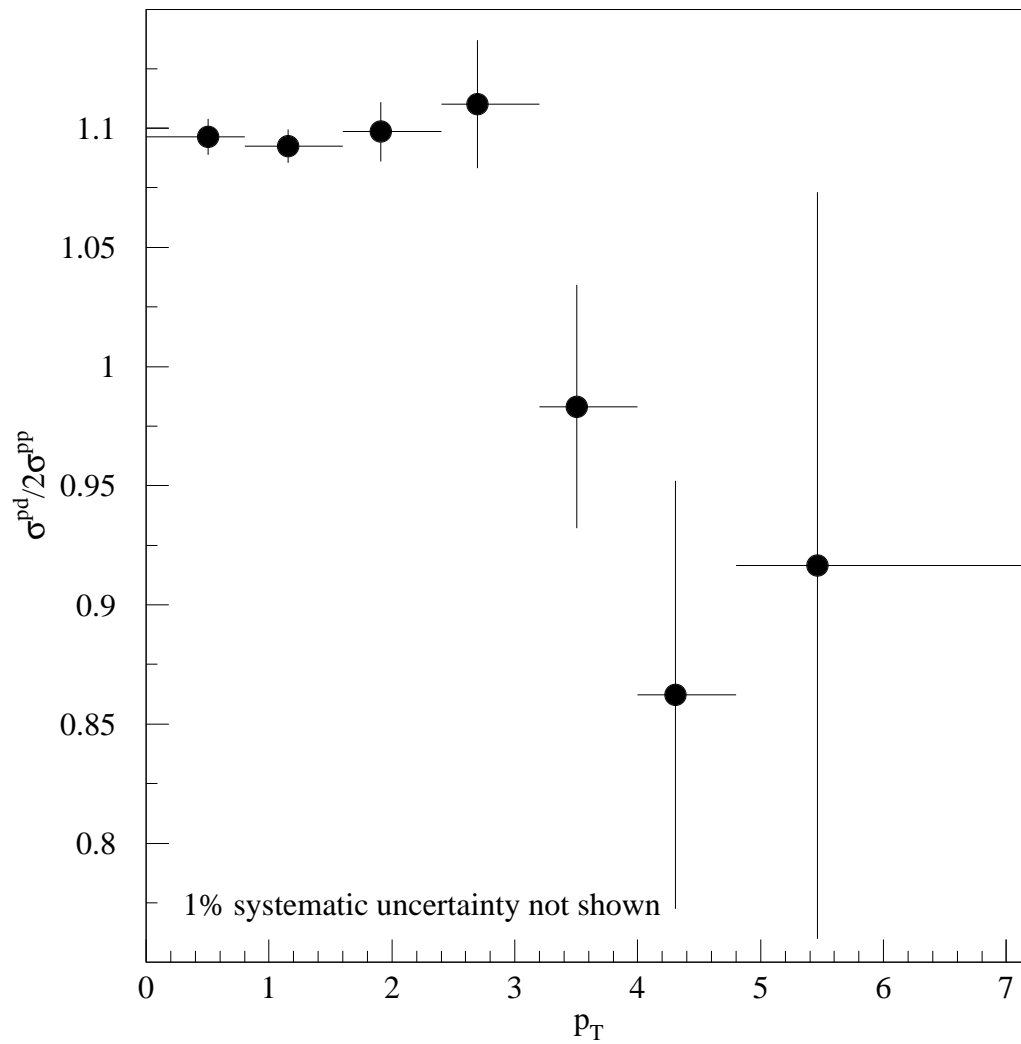


Figure 5.10: The Drell-Yan cross section ratio versus p_T . The combined result from all data sets is shown. The error bars represent the statistical uncertainty. There is a one percent systematic uncertainty common to all points.

Table 5.17: Systematic uncertainties in measurement of $\sigma^{pd}/2\sigma^{pp}$.

source of uncertainty	uncertainty in mass setting		
	high	intermediate	low
rate dependence	0.69 %	0.89 %	0.82 %
target length	0.2 %	0.2 %	0.2 %
beam intensity	0.1 %	0.1 %	0.1 %
attenuation/acceptance	0.2 %	0.2 %	0.2 %
deuterium composition	0.61 %	—	—

uation, and acceptance differences. Table 5.17 shows the sources of systematic uncertainty in the cross section ratio for each mass setting. Clearly the rate dependence is the dominant systematic uncertainty except in the data taken with a slight hydrogen contamination in the deuterium target. By adding all of the sources of systematic uncertainty in quadrature, the total systematic uncertainty in the measured cross section ratio is determined to be less than one percent.

The systematic uncertainty from the target length is due to a known slight difference between the length of the target flasks. What is unknown, is which flask is longer. The beam intensity systematic uncertainty is based on the difference between the ratio of the integrated beam intensity on the two targets as measured by the many different monitors. Since the low and intermediate mass data used to calculate the cross section ratio was all from the first fill of the deuterium target, they do not suffer from the systematic uncertainty due to the deuterium composition.

5.10 Extraction of $\bar{d}(x)/\bar{u}(x)$

From the discussion in Chapter 2 it is clear that $\sigma^{pd}/2\sigma^{pp}$ is closely related to \bar{d}/\bar{u} . However, the simple approximations that lead to equations 2.16 and 2.22 are based on mutually exclusive kinematic conditions. Since the data shown in Fig. 5.8 includes events that fall into both of these kinematic regions, as well as in between where neither approximation is valid, neither equation can be used to extract \bar{d}/\bar{u} . Therefore, an iterative process was used to extract \bar{d}/\bar{u} from the cross section ratio that did not make any assumptions about the kinematics of the data.

This iterative process calculated $\sigma^{pd}/2\sigma^{pp}$, compared this calculated quantity with the measured quantity, adjusted \bar{d}/\bar{u} that goes into the calculation of $\sigma^{pd}/2\sigma^{pp}$, and repeated. This process continued until the calculated $\sigma^{pd}/2\sigma^{pp}$ agreed with the measured ratio. The results of this method, for each mass setting treated independently, are shown in Fig. 5.11.

In the combined \bar{d}/\bar{u} ratio results shown in Fig. 5.12 and Table 5.18, convergence of the iterative process was determined by selecting the \bar{d}/\bar{u} which minimized

$$\chi^2 = \sum_i \left[\frac{r_i|_{(\text{meas})} - r_i|_{(\text{calc})}}{\delta_{(\text{meas})}} \right]^2 \quad (5.31)$$

for each data point, where r_i and δ_i are as defined in equation 5.30.

These extracted quantities have been scaled to a common Q^2 valued of 41 GeV². The details important to this iterative extraction process will be discussed in the remainder of this section.

From Eq. 2.10 it is obvious that to calculate $\sigma^{pd}/2\sigma^{pp}$ the PDF for each quark and antiquark present in the nucleon must be known. While calculating

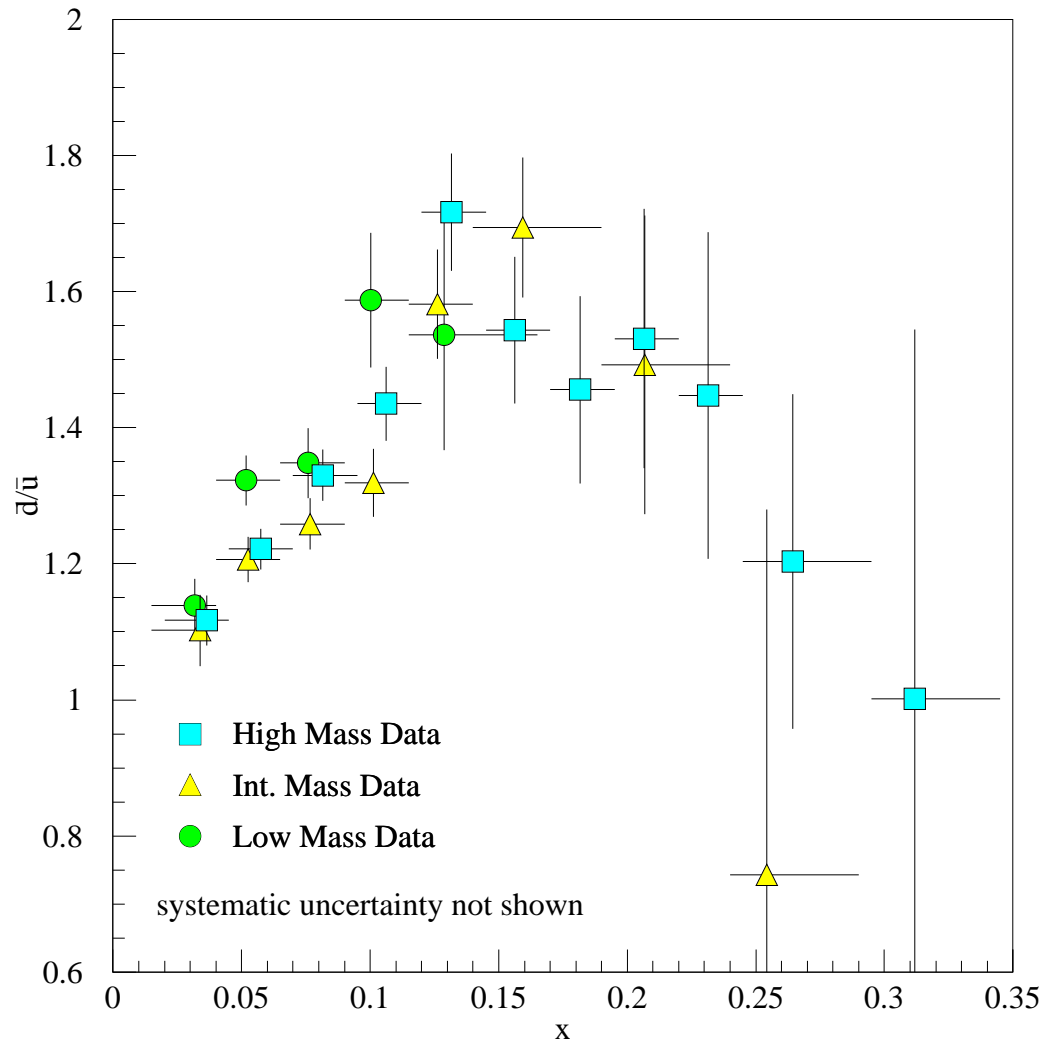


Figure 5.11: \bar{d}/\bar{u} versus x . The results from all three mass settings are shown. The error bars represent the statistical uncertainty. The systematic uncertainty, which varies from about 2% at low x to a maximum of 3.5% at high x , is not shown.

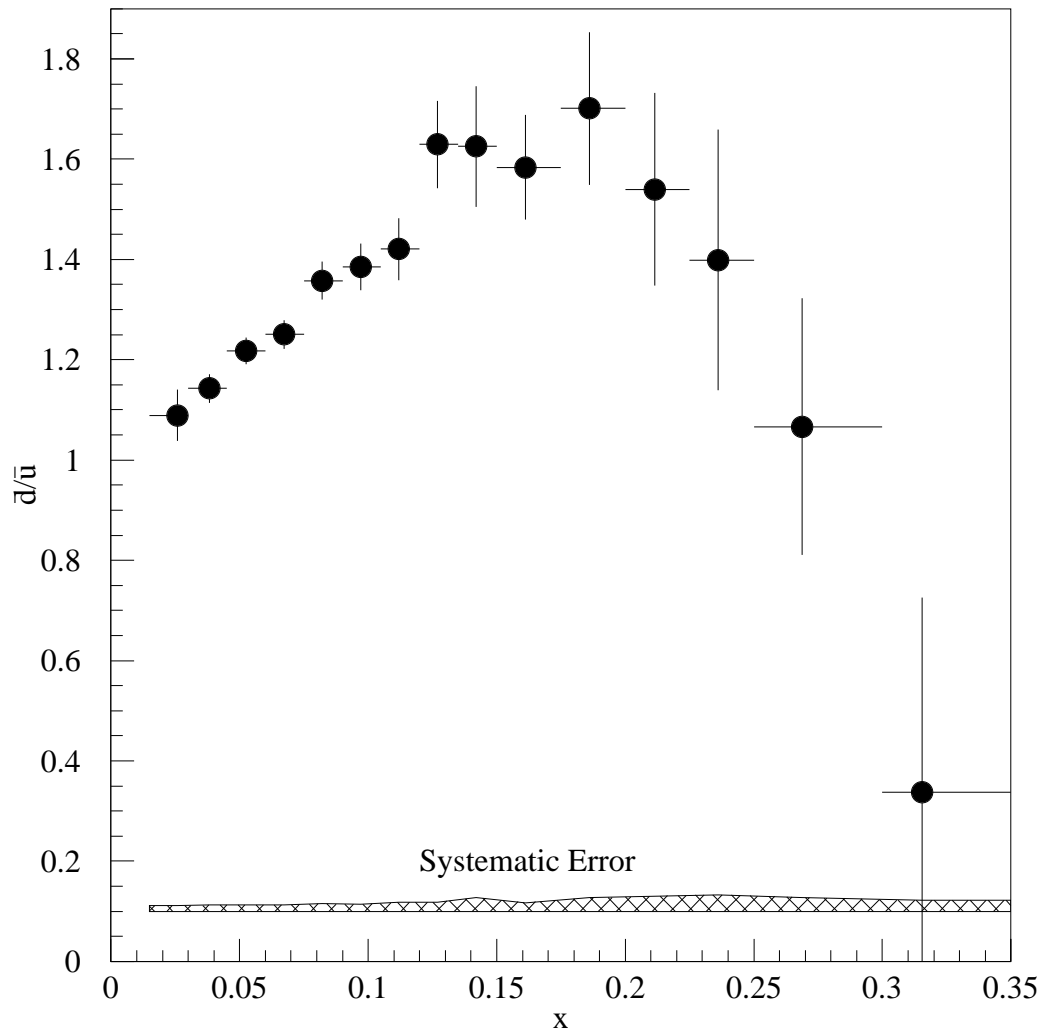


Figure 5.12: \bar{d}/\bar{u} versus x . The combined result from all three mass settings is shown.

Table 5.18: The value of $\bar{d}(x)/\bar{u}(x)$ and $\bar{d}(x) - \bar{u}(x)$ as determined from all data sets for each x_2 bin. The statistical uncertainty is listed first followed by the systematic uncertainty.

x_2 range min-max	\bar{d}/\bar{u}	$\bar{d}(x) - \bar{u}(x)$
0.015-0.030	1.089 \pm .051 \pm 0.011	0.882 \pm 0.486 \pm 0.104
0.030-0.045	1.143 \pm .028 \pm 0.012	0.780 \pm 0.145 \pm 0.063
0.045-0.060	1.217 \pm .026 \pm 0.012	0.715 \pm 0.078 \pm 0.037
0.060-0.075	1.250 \pm .028 \pm 0.013	0.543 \pm 0.055 \pm 0.025
0.075-0.090	1.358 \pm .038 \pm 0.015	0.523 \pm 0.047 \pm 0.019
0.090-0.105	1.385 \pm .047 \pm 0.014	0.409 \pm 0.042 \pm 0.012
0.105-0.120	1.421 \pm .062 \pm 0.018	0.332 \pm 0.040 \pm 0.012
0.120-0.135	1.629 \pm .087 \pm 0.018	0.350 \pm 0.037 \pm 0.008
0.135-0.150	1.625 \pm .120 \pm 0.028	0.271 \pm 0.040 \pm 0.009
0.150-0.175	1.584 \pm .105 \pm 0.017	0.189 \pm 0.026 \pm 0.004
0.175-0.200	1.701 \pm .152 \pm 0.027	0.148 \pm 0.024 \pm 0.004
0.200-0.225	1.540 \pm .193 \pm 0.030	0.083 \pm 0.023 \pm 0.004
0.225-0.250	1.399 \pm .260 \pm 0.033	0.045 \pm 0.025 \pm 0.003
0.250-0.300	1.067 \pm .256 \pm 0.028	0.005 \pm 0.020 \pm 0.002
0.300-0.350	.337 \pm .389 \pm 0.021	-0.042 \pm 0.037 \pm 0.002

$\sigma^{pd}/2\sigma^{pp}$ for the iterative process, it was assumed that an existing PDF parameterization accurately described the quark distributions and the quantity $\bar{d}(x) + \bar{u}(x)$ since these quantities have been constrained by previous measurements. The parameterizations used were CTEQ4M [15], MRS(R2) [16] and MRST [28]. While the ratio of $\bar{d}(x)$ to $\bar{u}(x)$ was very poorly constrained in these parameterizations and therefore was adjusted with each iteration, the sum of $\bar{d}(x)$ and $\bar{u}(x)$ was reasonably well known and it was held constant.

So that the calculated $\sigma^{pd}/2\sigma^{pp}$ could be compared to the measured $\sigma^{pd}/2\sigma^{pp}$, the acceptance of the spectrometer had to be included in the calculated quantity. To do this the cross section ratio was calculated for the x_1 , x_2 , and Q^2 values of every event that passed the analysis cuts. These calculated cross section ratios were then averaged over a given x_2 bin.

As $\sigma^{pd}/2\sigma^{pp}$ was calculated for each iteration, it was assumed that \bar{d}/\bar{u} for the beam proton was the same as \bar{d}/\bar{u} for the target proton over the x_2 range of the data. For many events however, x_1 was greater than the maximum x_2 in the data, so something had to be assumed for $\bar{d}(x_1)/\bar{u}(x_1)$ above $x_1 = 0.35$. The affects of several different assumptions were investigated. The extracted \bar{d}/\bar{u} was not noticeably affected by any of these assumptions except at the highest x values, which changed by less than five percent. The final assumption that was used was to assume that $\bar{d}(x_1)/\bar{u}(x_1) = 1.0$ in the proton for $x_1 > 0.35$.

Once the quantity $\bar{d}(x)/\bar{u}(x)$ is determined, the quantity $\bar{d}(x) - \bar{u}(x)$ can be calculated using

$$\bar{d}(x) - \bar{u}(x) = \frac{\left(\frac{\bar{d}}{\bar{u}} - 1\right)}{\left(\frac{\bar{d}}{\bar{u}} + 1\right)}(\bar{d} + \bar{u}). \quad (5.32)$$

Here again the quantity $\bar{d} + \bar{u}$ is assumed to be correctly described by one of the parameterizations. Figure 5.13 shows $\bar{d}(x) - \bar{u}(x)$ as a function of x for each of the mass settings while the combined result is shown in Fig. 5.14 and Table 5.18.

Once $\bar{d} - \bar{u}$ is determined, then the integral of $\bar{d} - \bar{u}$ can be calculated between x^{min} and 0.35. Figure 5.15 shows $\int_{x^{min}}^{0.35} (\bar{d}(x) - \bar{u}(x)) dx$. Over the measured region, the value of this integral has been determined to be

$$\int_{0.015}^{0.35} (\bar{d}(x) - \bar{u}(x)) dx = 0.0818 \pm 0.0082 \pm 0.0049. \quad (5.33)$$

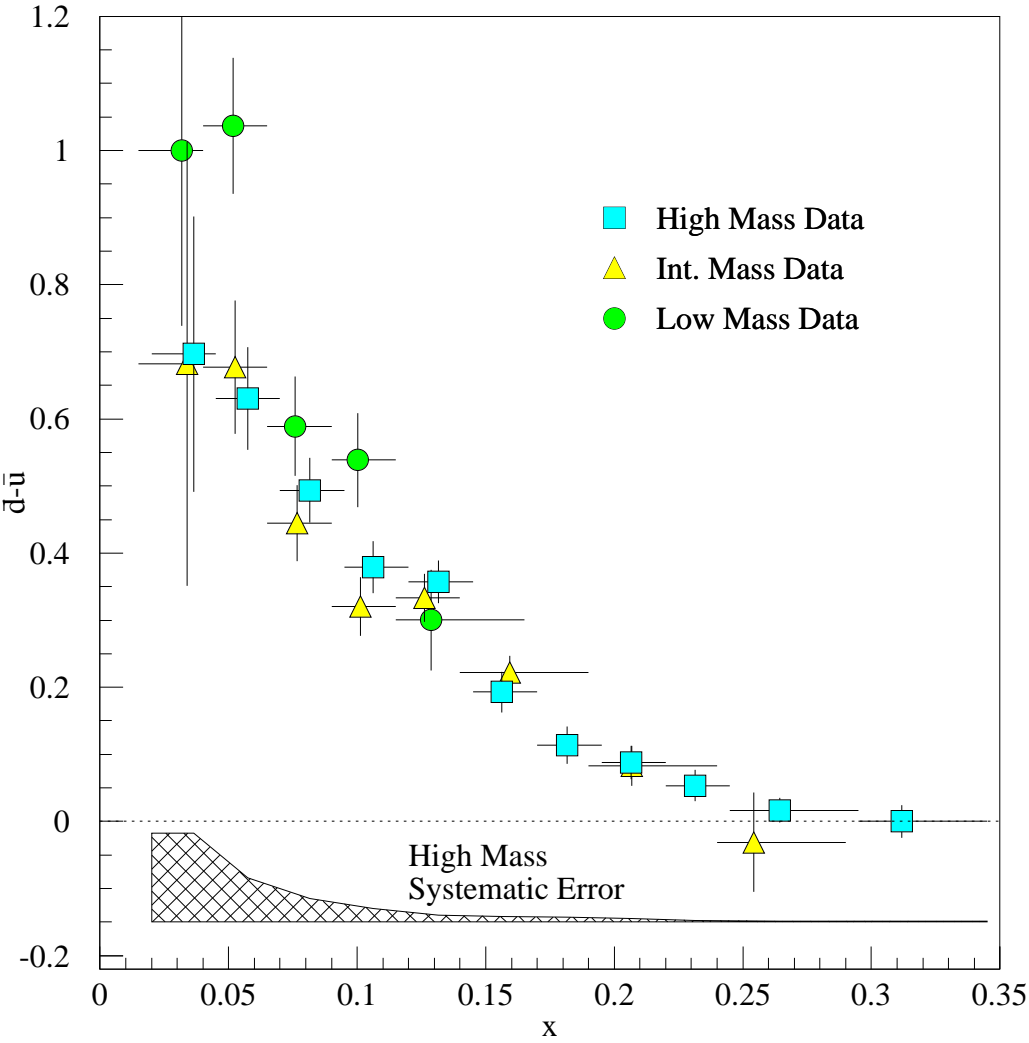


Figure 5.13: $\bar{d} - \bar{u}$ versus x . The results from all three mass settings are shown. The systematic uncertainty is shown for the high mass data. The systematic uncertainty for the other data sets are very similar.

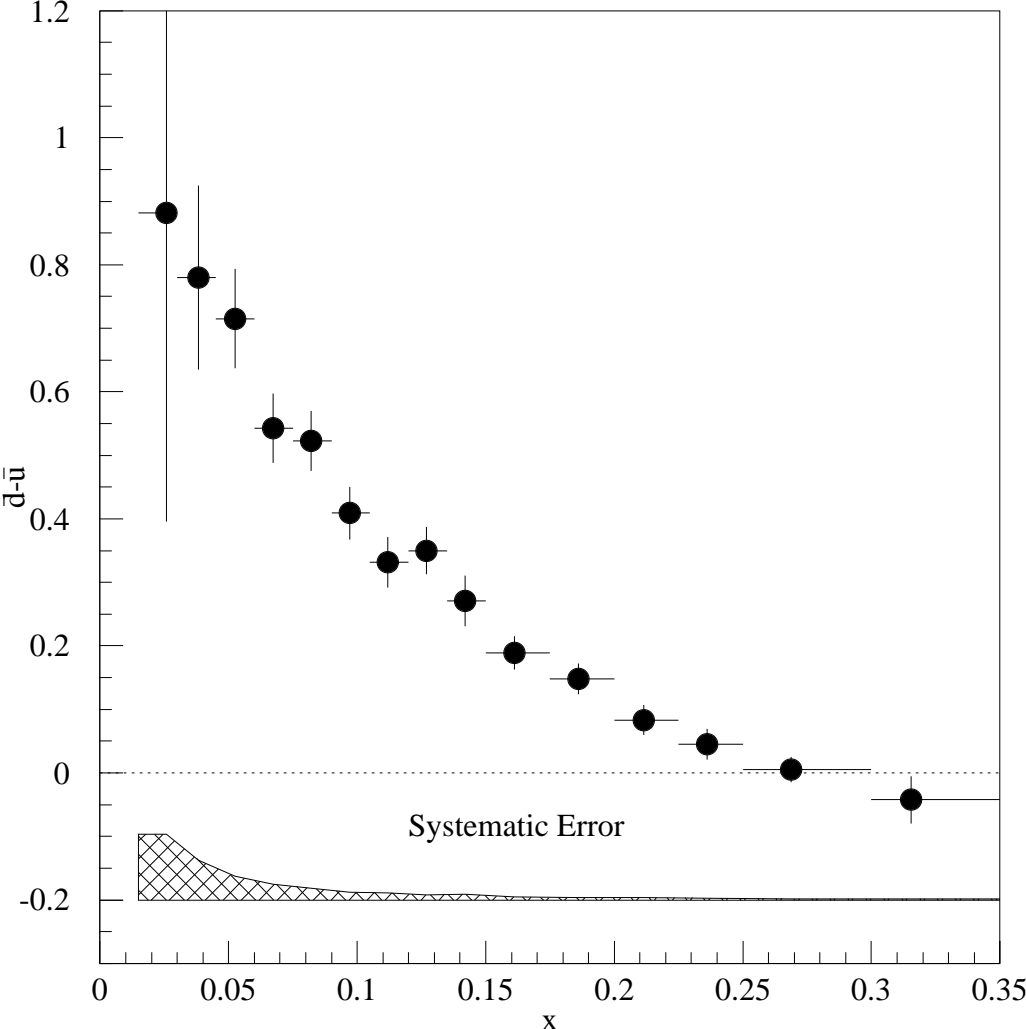


Figure 5.14: $\bar{d} - \bar{u}$ versus x . The combined result from all three mass settings is shown.

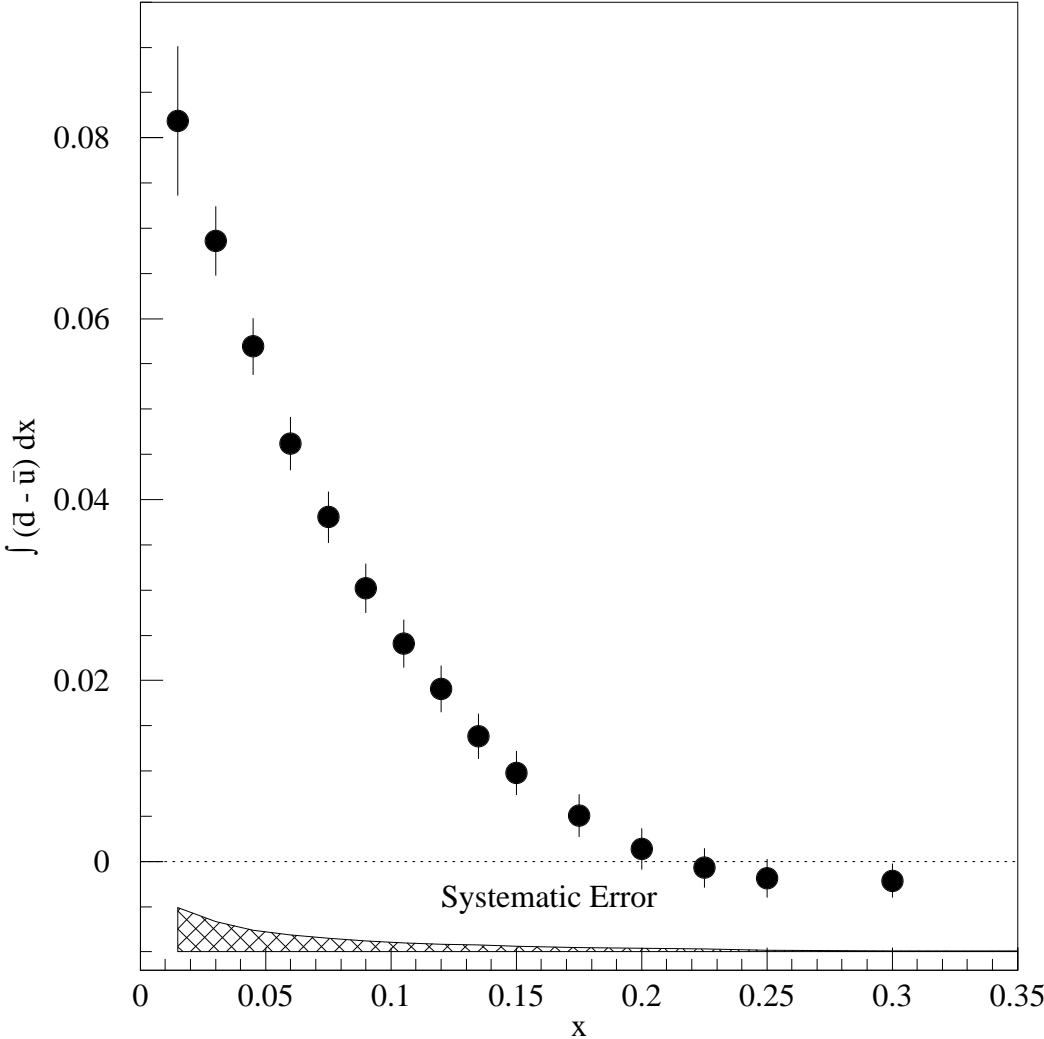


Figure 5.15: $\int_x^{0.35} (\bar{d}(x) - \bar{u}(x)) dx'$ in the proton versus x .

Chapter 6

Results and Conclusions

While previous experiments have indicated that $\bar{d} > \bar{u}$, FNAL E866/NuSea was the first measurement of the x dependence of the flavor asymmetry in the nucleon sea. This measurement has had an impact in several different areas. The global parameterizations of the nucleon sea will obviously change to fit these new data. Surprisingly, this measurement when used in conjunction with the NMC measurement, puts new and tighter constraints on the valence PDF's. This measurement has also provided a means of testing the predictions of several nonperturbative models. Finally, the unexpected sharp downturn in $\bar{d}(x)/\bar{u}(x)$ apparently back to unity at the large x limits of this measurement, has motivated a proposal to perform a similar experiment focused at higher x values.

6.1 E866 Results

The primary measurement of this experiment was the determination of $\sigma^{pd}/2\sigma^{pp}$ over a wide kinematic range. The combined result from all three mass settings is shown in Fig. 6.1 along with the curves from the calculated cross section ratio using various parameterizations. The CTEQ4M [15] and MRS(R2) [16] parameterizations do not include this measurement as a constraint and do not

reproduce the data. The MRST [28] parameterization does include the first published results [27] from this experiment which included the measurement of $\sigma^{pd}/2\sigma^{pp}$ as determined from the high mass data.

The main physics results of this experiment are $\bar{d}(x)/\bar{u}(x)$, $\bar{d}(x) - \bar{u}(x)$, and $\int(\bar{d}(x) - \bar{u}(x))dx$ of the proton. These results are shown in Figs. 6.2, 6.3, and 6.4 along with the curves from the various parameterizations. Again, parameterizations that do not include results from this measurement do not fit these results.

To illustrate how this measurement has tightened constraints on the valence quark PDF's, it is useful to decompose how the parameterizations fit the NMC [1] measurement discussed in Section 2.1. The quantity that NMC measured, $F_2^p - F_2^n$, can be expressed as the sum of the valence quark contribution and the sea quark contribution.

$$F_2^p - F_2^n = \underbrace{\frac{x}{3}(u - d)}_{\text{valence}} + \underbrace{\frac{2x}{3}(\bar{u} - \bar{d})}_{\text{sea}} \quad (6.1)$$

Since $u > d$ the valence contribution is positive while the sea contribution is negative because $\bar{d} > \bar{u}$.

Figure 6.5 shows the NMC measurement and the fit to the data according to the MRS(R2) parameterization. The NMC measurement provides a rigid constraint on the sum of the valence and the sea contributions, but does not constrain either contribution separately. Also shown in Fig. 6.5 is the MRS(R2) parameterization decomposed into the valence and sea contributions. The sea contribution can be compared with the new constraint provided by the high

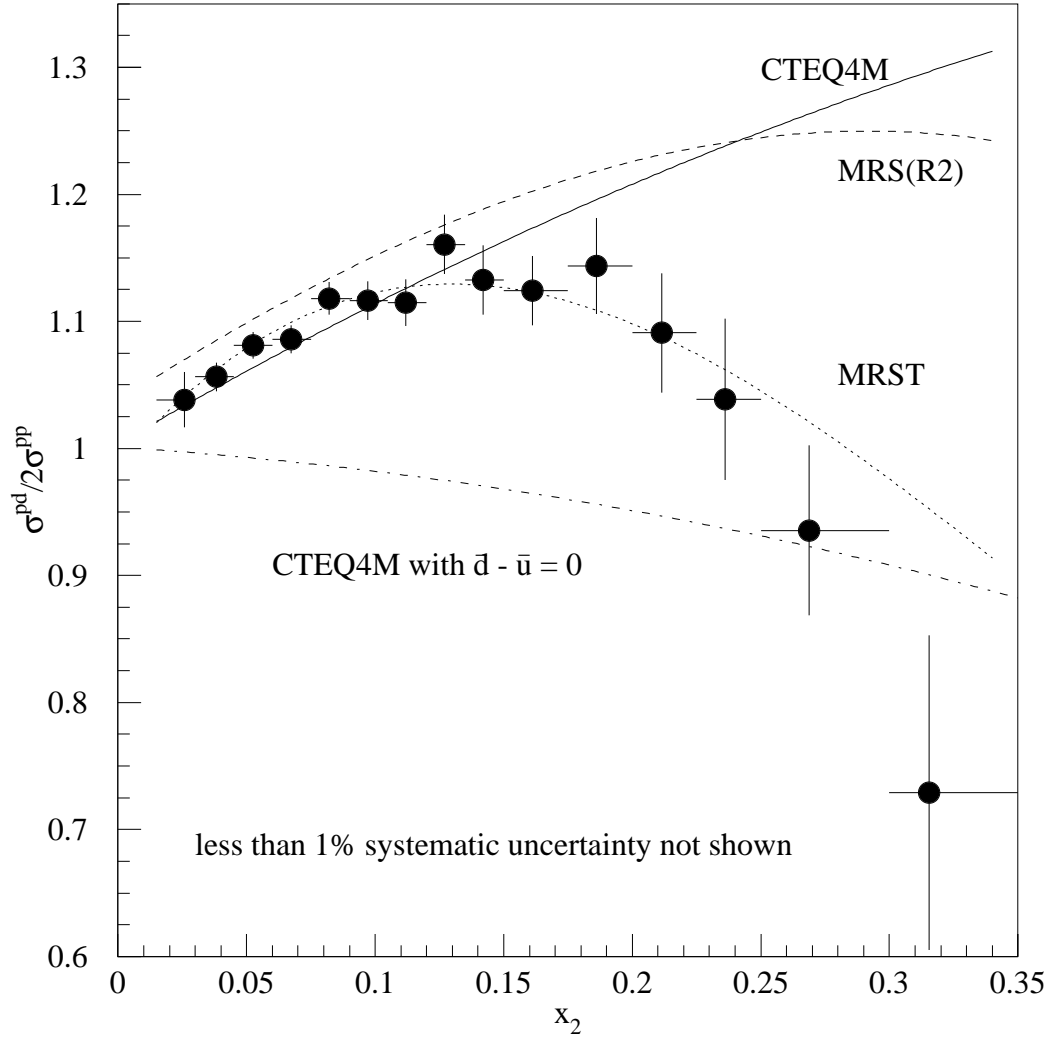


Figure 6.1: The Drell-Yan cross section ratio versus x of the target parton. The results from all three mass settings have been combined. The curves are the calculated cross section ratio using CTEQ4M [15], MRS(R2) [16], and MRST [28]. The bottom curve is calculated using CTEQ4M where $\bar{d} - \bar{u}$ has been set to zero.

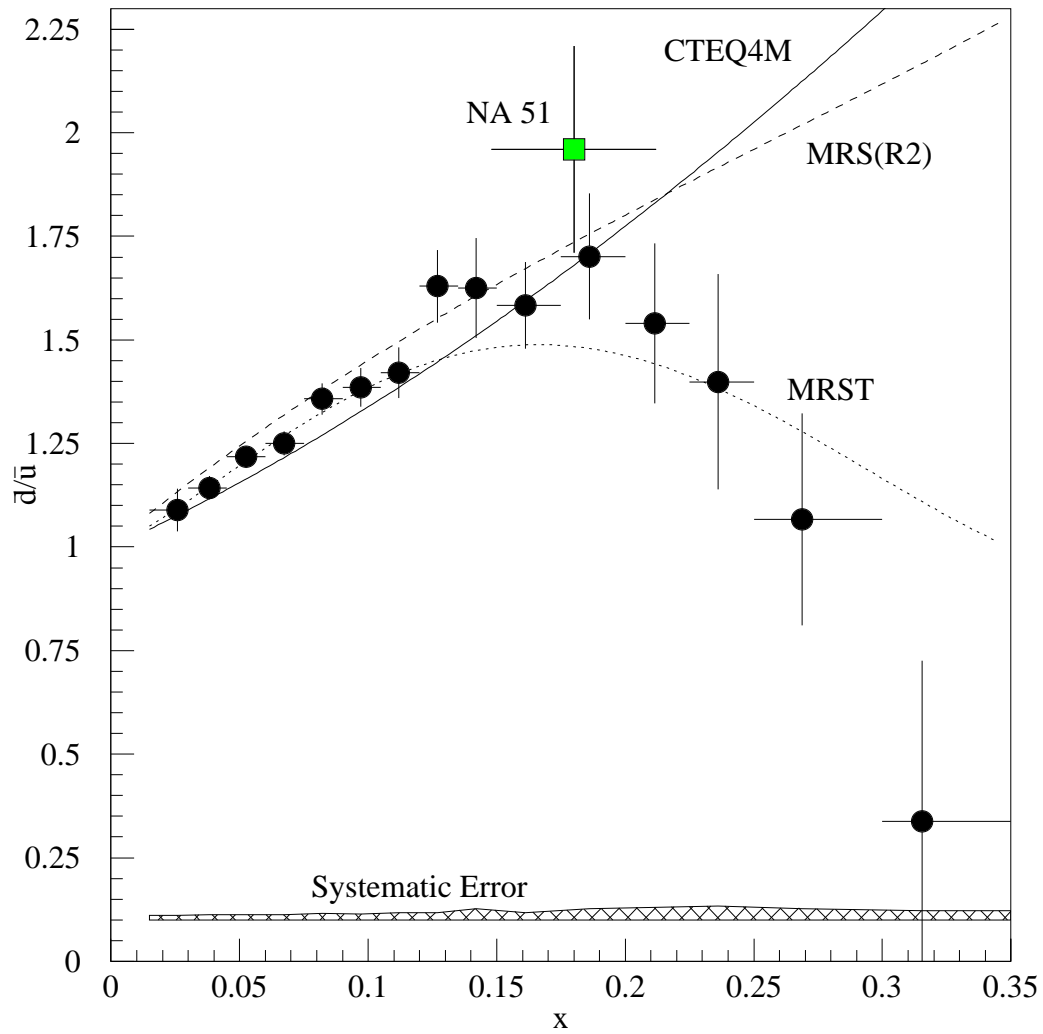


Figure 6.2: $\bar{d}(x)/\bar{u}(x)$ versus x . The combined result from all three mass settings is shown along with three parameterizations. The NA51 data point is also shown.

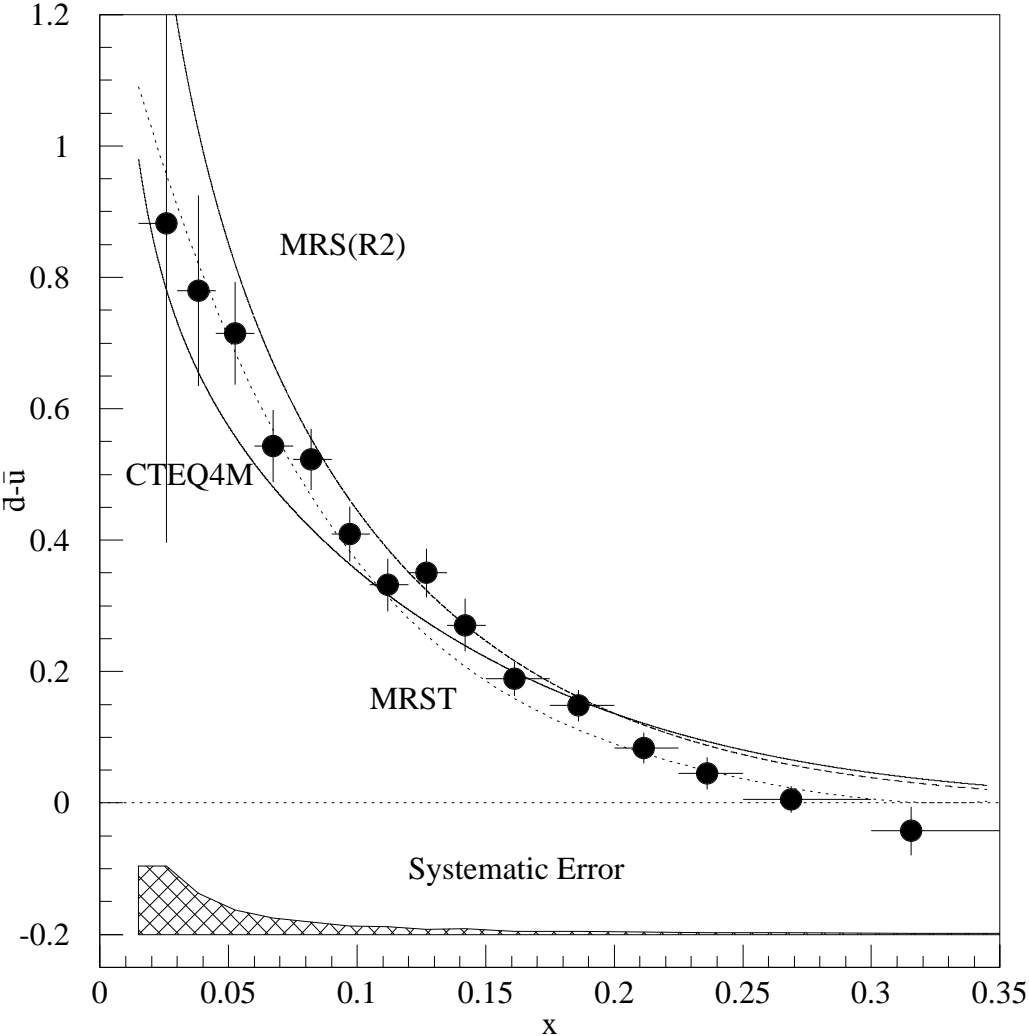


Figure 6.3: $\bar{d}(x) - \bar{u}(x)$ versus x . The combined result from all three mass settings is shown along with three parameterizations.

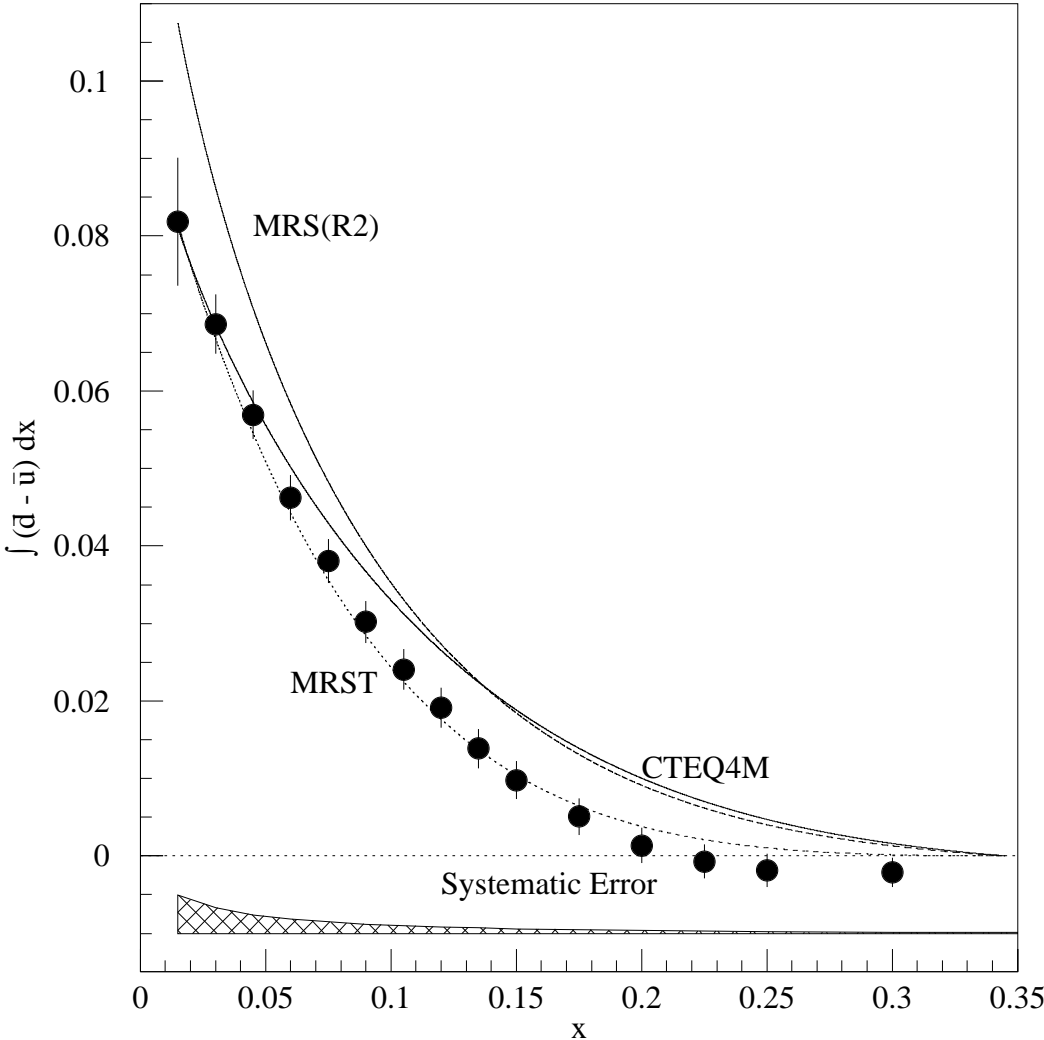


Figure 6.4: $\int_x^{0.35} (\bar{d}(x) - \bar{u}(x)) dx'$ versus x . The curves are from three different parameterizations.

mass data ¹ from E866. This comparison shows that the MRS(R2) parameterization of the sea contribution to $F_2^p - F_2^n$ over predicts the magnitude of the contribution.

The next generation global fit done by the MRS group, called MRST, does include ² the first published results from E866 [27]. As expected this new parameterization reproduces the E866 measured sea contribution to $F_2^p - F_2^n$. However, this was not the only change in the new global fit due to the E866 measurement. To maintain the fit to the NMC measurement while reducing the magnitude of the sea contribution required a corresponding decrease in the magnitude of the valence contribution over the same range in x . Finally, to maintain the proper number of valence up quarks,

$$\int_0^1 (u(x) - \bar{u}(x)) dx = 2, \quad (6.2)$$

and down quarks,

$$\int_0^1 (d(x) - \bar{d}(x)) dx = 1, \quad (6.3)$$

the magnitude of the valence contribution must increase over some other x range. All three of these changes can be seen in Fig. 6.6, which is identical to Fig. 6.5 except with the addition of the MRST parameterization.

6.2 Comparison to Other Experiments

The results of this experiment are much more extensive and precise than any other measurement of $\bar{d}(x)/\bar{u}(x)$. Other measurements of $\bar{d}(x)/\bar{u}(x)$ include

¹ Only the high mass data is shown in Fig. 6.5 and Fig. 6.6. This allows for a fair comparison with the MRST parameterization which only had the high mass data as a constraint.

²The MRST parameterization includes other new measurements which also affect the valence parameterization.

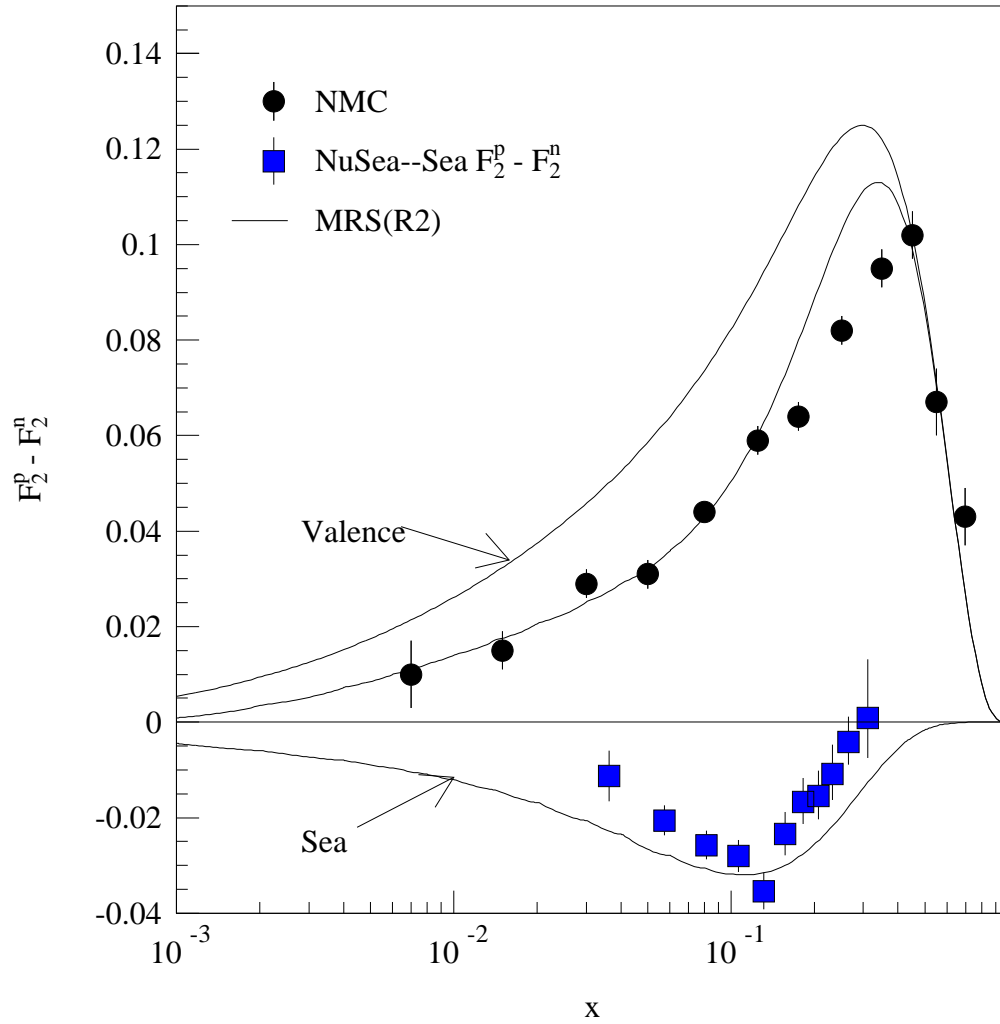


Figure 6.5: $F_2^p - F_2^n$ as measured by NMC at $Q = 2$ GeV compared with predictions based on the MRS(R2) parameterization. Also shown are the E866 high mass results, evolved to $Q = 2$ GeV, for the sea contribution to $F_2^p - F_2^n$. The top (bottom) curve is the valence (sea) contribution and the middle curve is the sum of the two.

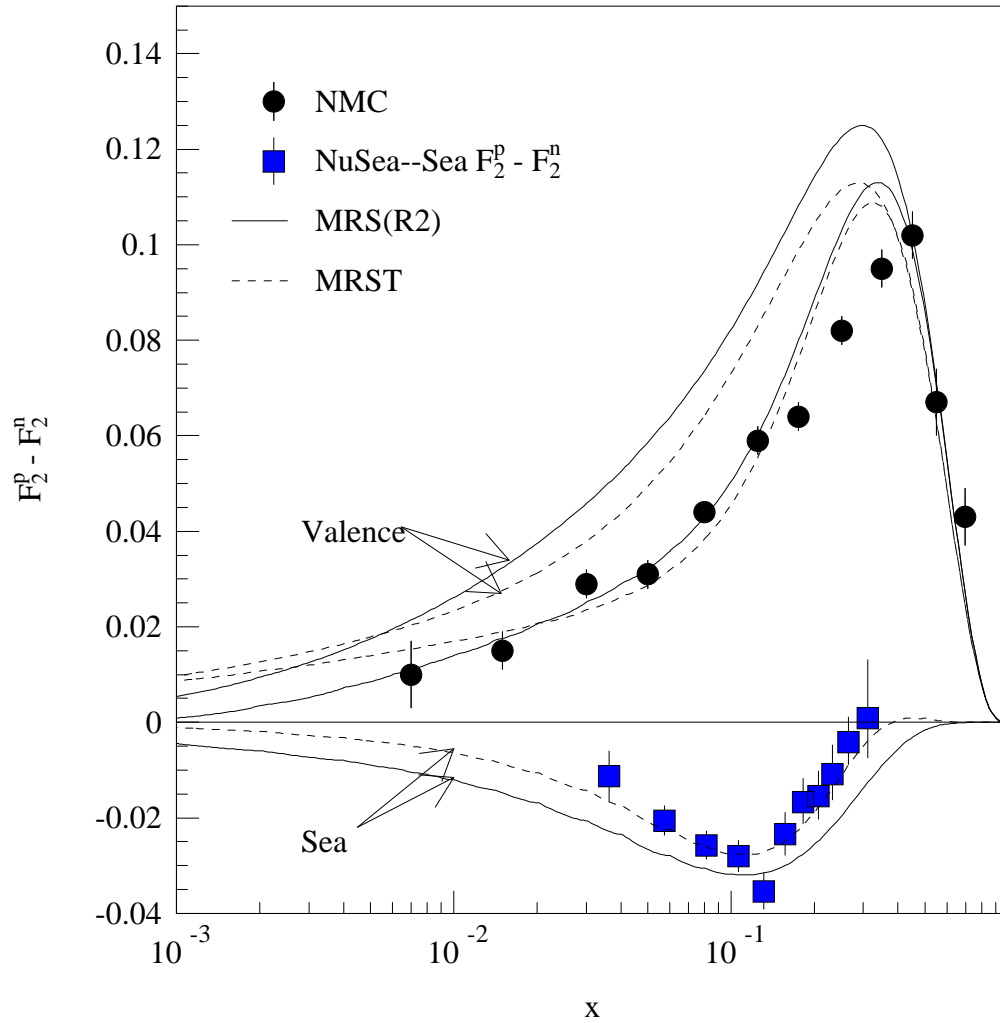


Figure 6.6: $F_2^p - F_2^n$ as measured by NMC at $Q = 2$ GeV compared with predictions based on the MRS(R2) (solid) and MRST (dashed) parameterizations. Also shown are the E866 high mass results, evolved to $Q = 2$ GeV, for the sea contribution to $F_2^p - F_2^n$. For each prediction, the top (bottom) curve is the valence (sea) contribution and the middle curve is the sum of the two.

the early measurement by NA51 which was discussed in Chapter 2 and the recent result from the HERMES collaboration [29] at DESY. Both of these measurements are in general agreement with the E866 results as seen in Fig. 6.2 and Fig. 6.7. Even though the average Q^2 of these measurements are different, comparisons can be made between them because the Q^2 dependence is small.

While the NA51 determination of $\bar{d}(x)/\bar{u}(x)$ was very similar to the method used by E866, the HERMES result was based on a measurement of semi-inclusive deep-inelastic scattering. While their measurement does not have either the coverage or the precision of E866, it does provide a truly independent confirmation of the results. Many of the systematic effects that are common to the NA51 and E866 Drell-Yan experiments do not affect the HERMES measurement.

These measurements of $\bar{d}(x)/\bar{u}(x)$ can be compared to the NMC DIS results by integrating $\bar{d}(x) - \bar{u}(x)$. Table 6.1 summarizes the value of this integral over different x ranges as parameterized by various global fits and as measured by E866. To extrapolate this integral from the measured region to the unmeasured region, MRST was used to estimate the contribution for $0 \leq x \leq 0.015$ and it was assumed that the contribution for $x \geq 0.35$ was negligible. To estimate the uncertainty from this extrapolation, it was assumed that the MRST contribution contained a 20% uncertainty. Table 6.2 summarizes three different experimental determinations of this integral over all x values.

6.3 Possible Origins of the Nucleon Sea

The possible production mechanisms that can account for the sea of quark-antiquark pairs in the nucleon can be categorized as either perturbative or

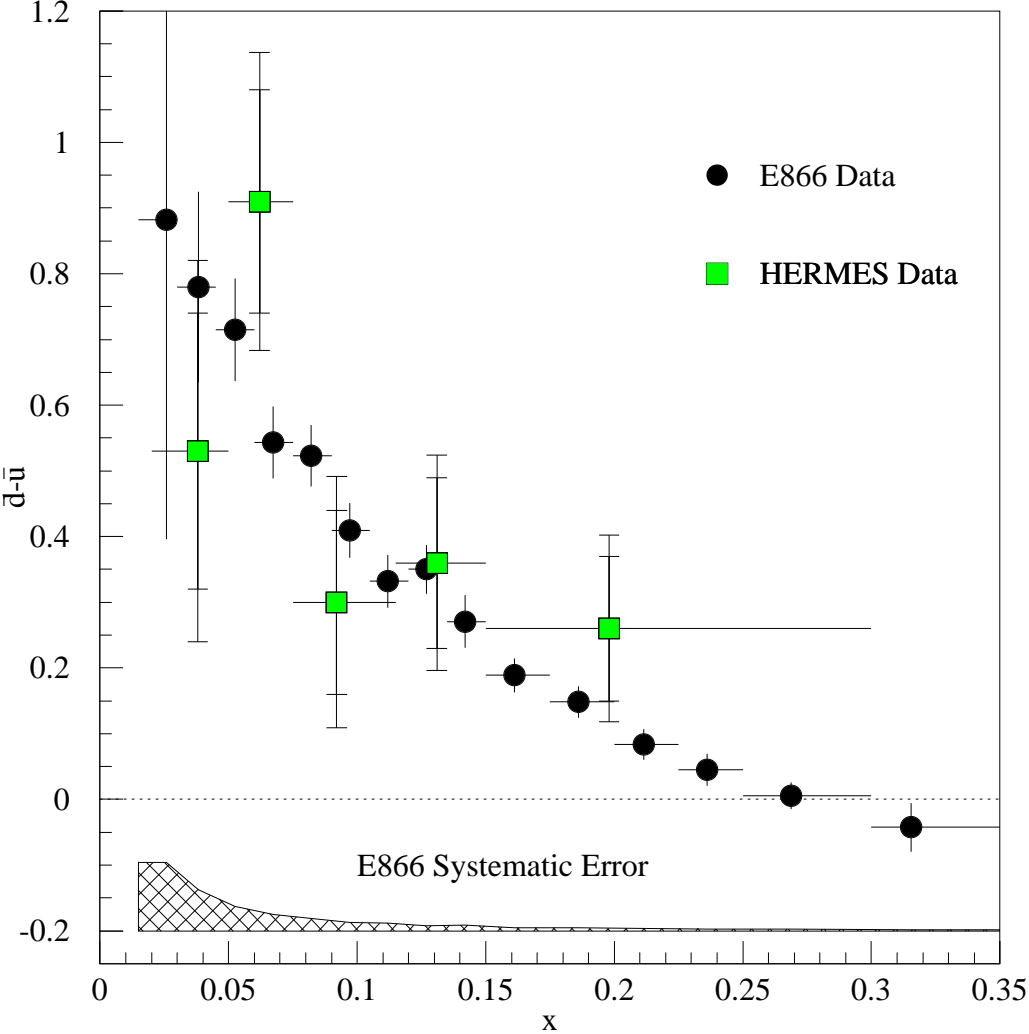


Figure 6.7: $\bar{d}-\bar{u}$ as a function of x . The E866 (HERMES) results are shown as round (square) data points. The error bars on the E866 data points represent the statistical uncertainty. The inner error bars on the HERMES data points represent the statistical uncertainty while the outer error bars represent the statistical and systematic uncertainty added in quadrature.

Table 6.1: $\int (\bar{d}(x) - \bar{u}(x))dx$ evaluated over different x ranges based on three different parameterizations and as measured by E866.

x range	CTEQ(4M)	MRS(R2)	MRST	E866
$0 < x < 1$	0.10941	0.16553	0.11482	
$0.35 < x < 1$	0.00186	0.00129	-0.00031	
$0.015 < x < 0.35$	0.08163	0.10845	0.08219	0.082 ± 0.010
$0 < x < 0.015$	0.02592	0.05578	0.03293	

Table 6.2: $\int (\bar{d}(x) - \bar{u}(x))dx$ as determined by three experiments. The range of the measurement is shown along with the value of the integral over all x .

Experiment	x range	$\int_0^1 (\bar{d}(x) - \bar{u}(x))dx$
E866	$0.015 < x < 0.35$	0.115 ± 0.012
NMC	$0.004 < x < 0.80$	0.147 ± 0.039
HERMES	$0.020 < x < 0.30$	0.16 ± 0.03

nonperturbative. The next two subsections will describe each of these categories. The primary focus of this section is to compare each possible production mechanism with the observed flavor asymmetry.

6.3.1 Perturbative Origins

The perturbative production mechanism is the production of a quark-antiquark pair from gluon splitting. This is the simplest method of producing the nucleon sea, but it can not produce a substantial asymmetry.

In 1977 Field and Feynman first suggested [30] a possible means by which gluon splitting may produce an asymmetric sea. They suggested that Pauli blocking in the proton would suppress a gluon splitting into an up-antiup quark pair compared to a gluon splitting into a down-antidown quark pair.

Since there are two valence up quarks and only one valence down quark in the proton, Pauli blocking could produce a flavor asymmetry.

Shortly after it was suggested that Pauli blocking could produce a flavor asymmetry in the nucleon, quantitative calculations [31] showed that this effect was less than one percent. More recently, additional calculations [32] have shown that while Pauli blocking does produce a small effect, it also produces an asymmetry opposite of what has been observed.

While gluon splitting is a source of quark-antiquark pairs in the nucleon, it can not be the source of the large observed flavor asymmetry. Additional production mechanisms must be considered. As these nonperturbative methods are discussed in the next subsection, it is important to remember that they must be considered in addition to the perturbative method, which produces a mostly symmetric sea.

6.3.2 Nonperturbative Origins

Meson cloud models [33, 34] describe the production of an asymmetric nucleon sea by expressing the physical proton as the combination of a proton with a symmetric sea and a series of virtual meson-baryon states. For example, the physical proton ($|p\rangle$) can be expressed as,

$$\begin{aligned}
 |p\rangle &= \sqrt{1 - |\alpha|^2 - |\beta|^2} |p_0\rangle \\
 &+ \alpha \left[\sqrt{2/3} |n, \pi^+\rangle - \sqrt{1/3} |p, \pi^0\rangle \right] \\
 &+ \beta \left[\sqrt{1/2} |\Delta^{++}, \pi^-\rangle - \sqrt{1/3} |\Delta^+, \pi^0\rangle + \sqrt{1/6} |\Delta^0, \pi^+\rangle \right]
 \end{aligned} \tag{6.4}$$

where $|p_0\rangle$ is a proton with a symmetric sea and $|\alpha|^2$ ($|\beta|^2$) is the probability that a proton is in a virtual $|N, \pi\rangle$ ($|\Delta, \pi\rangle$) state.

From Eq. 6.4 it is easy to show that

$$\int_0^1 [\bar{d}(x) - \bar{u}(x)] dx = (2a - b)/3, \quad (6.5)$$

where $a = |\alpha|^2$ and $b = |\beta|^2$. Calculations of the relative probability of these two configurations find $a \approx 2b$ [36]. Using the value for the integral in Eq. 6.5 extracted from E866 and assuming that $a = 2b$ yields $a = 2b = 0.230 \pm 0.024$. From this simple meson model, quark counting would indicate that

$$\frac{\bar{d}}{\bar{u}} = \frac{\frac{5}{6}a + \frac{1}{3}b}{\frac{1}{6}a + \frac{2}{3}b} = 2. \quad (6.6)$$

This simple determination of \bar{d}/\bar{u} does not include the x dependence of the ratio or any contribution from the perturbatively produced symmetric sea.

Figure 6.8 compares $\bar{d}(x) - \bar{u}(x)$ from E866 with a meson cloud model calculation. These calculations are based on the procedure described in reference [33]. The SMRS(P2) [35] parameterization was used for the pion structure functions at a Q value of 6.38 GeV since the E866 results are shown at this value of Q . The curve labeled “Meson Model A” uses a dipole form with $\Lambda = 1.0$ GeV for the πNN and $\pi N\Delta$ form factors. It has been suggested [36] that Δ production experiments [37] indicate that the $\pi N\Delta$ form factor is softer than the πNN form factor. This observation has motivated the calculation for the curve in Fig. 6.8 labeled “Meson Model B” which uses a reduced value for the $\pi N\Delta$ form factor of $\Lambda = 0.8$ GeV. This calculation fits the E866 measurement better than Meson Model A.

It is also useful to compare the model predictions of $\bar{d}(x)/\bar{u}(x)$ with the results from E866. When making this comparison it is important to remember that the pion models do not include the perturbative production process. This

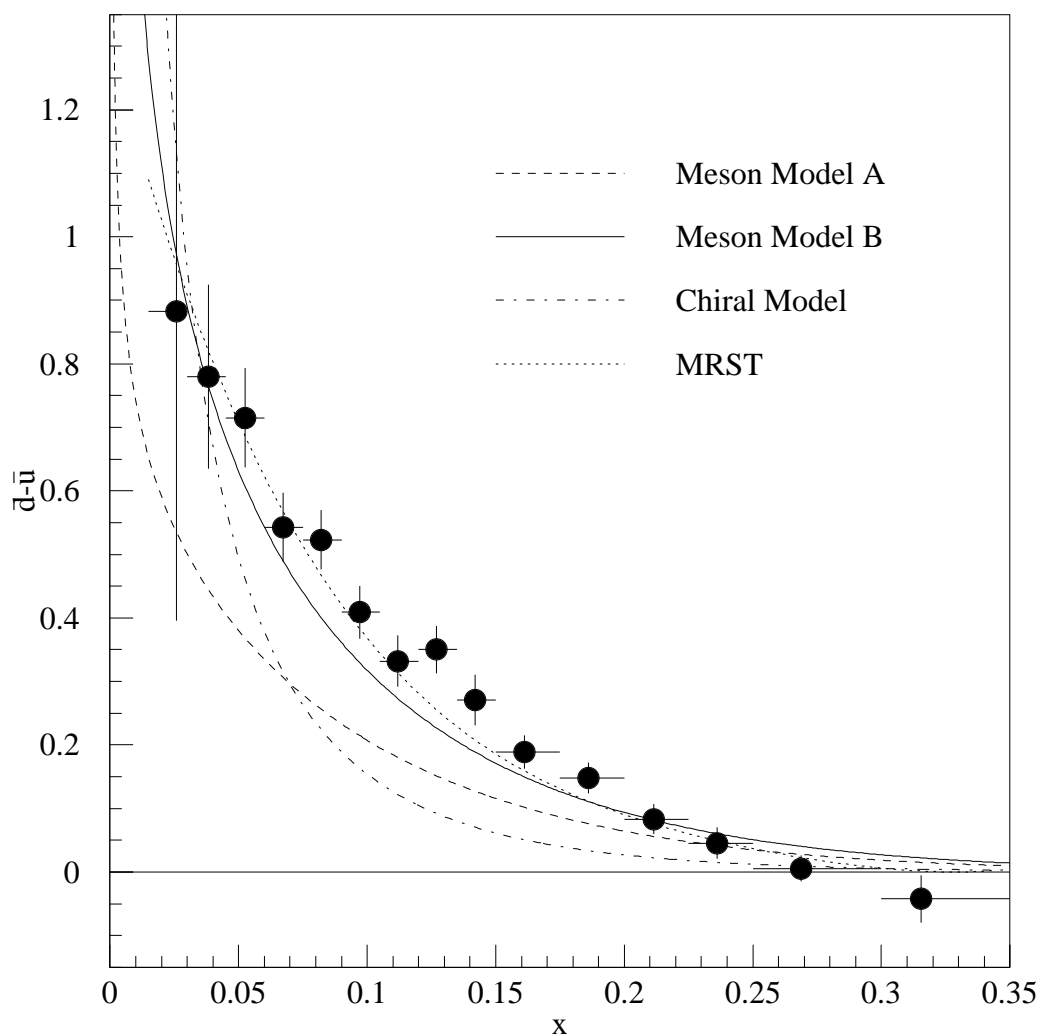


Figure 6.8: $\bar{d} - \bar{u}$ as a function of x . The E866 results are shown along with predictions of meson and chiral models. Both are shown for $Q = 6.38$ GeV.

did not affect the comparison of the meson models with $\bar{d}(x) - \bar{u}(x)$ because $\bar{d}(x) - \bar{u}(x)$ is only sensitive to the flavor asymmetry. However, $\bar{d}(x)/\bar{u}(x)$ is sensitive to both the asymmetric and the symmetric sea. Therefore, it is not surprising to see in Fig. 6.9 that the two meson models do not reproduce the E866 results. This comparison does show that meson model A can not accommodate an additional contribution from the perturbative production process for $0.1 < x < 0.2$. Figure 6.9 also provides information about the relative importance of the perturbative versus the non-perturbative sea.

Another class of models which produces a flavor asymmetry in the nucleon via the inclusion of virtual mesons are the chiral quark models [38, 39]. The chiral quark model is similar to the meson model, except the virtual meson couples directly to a quark, not the nucleon as a whole. So antiquarks are produced in processes such as $u \rightarrow d\pi^+$ and $d \rightarrow u\pi^-$. The excess of \bar{d} over \bar{u} in the proton is due to the additional up valence quark in the proton.

Figure 6.8 shows the chiral model prediction for $\bar{d}(x) - \bar{u}(x)$. This prediction was calculated following the formulation in reference [39]. The quantity $\bar{d}(x) - \bar{u}(x)$ was calculated at $Q = 0.5$ GeV and then evolved to $Q = 6.38$ GeV. As seen in Fig. 6.8, this model predicts a much smaller mean- x for $\bar{d}(x) - \bar{u}(x)$ than that predicted by the meson models. This is a result of the mesons in the chiral model coupling to the valence quarks which carry on average 1/3 of the nucleon momentum. The x dependence of the E866 data favor the meson model over the chiral model.

The last nonperturbative flavor asymmetry producing mechanism to be mentioned here is the coupling of instantons to the valence quarks. This model [40] does not seem to agree with any of the quantities measured by E866.

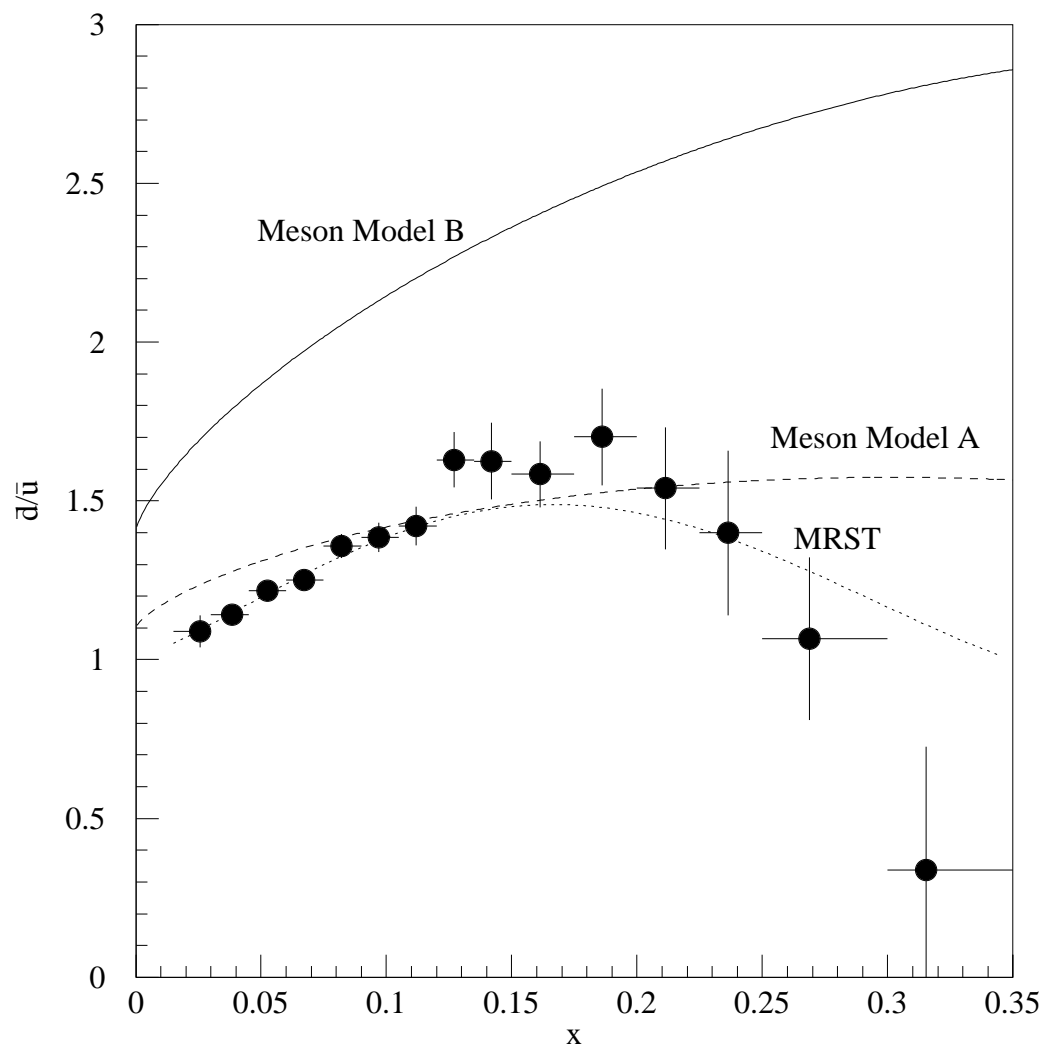


Figure 6.9: \bar{d}/\bar{u} as a function of x . The E866 results are shown along with predictions of meson models. Both are shown for $Q = 6.38$ GeV.

Specifically this model predicts that the cross section ratio would increase at high p_T , which is in total disagreement with Fig. 5.10. It is not known if better agreement with the data can be obtained by adjusting the parameters within the model.

6.4 Future Experiment

The sharp drop towards unity in $\bar{d}(x)/\bar{u}(x)$ above $x = 0.2$ was unexpected. This has prompted interest [41] in extending the measurement of $\sigma^{pd}/2\sigma^{pp}$ to higher values of x . A new experiment is currently being designed and proposed [42] to make this measurement using the 120 GeV proton beam from the new Main Injector at Fermilab.

The Drell-Yan cross section is inversely proportional to the incident beam energy. The Main Injector can provide protons at 120 GeV, which means that the Drell-Yan cross section will be about a factor of seven higher compared to the 800 GeV beam used for this measurement. The higher cross section means that the measurement of $\sigma^{pd}/2\sigma^{pp}$ could be extended to near $x = 0.5$.

6.5 Conclusion

FNAL E866/NuSea was an extremely successful experiment. The stated goal of measuring $\sigma^{pd}/2\sigma^{pp}$ with a systematic uncertainty of 1.5% over the kinematic range of $0.04 \leq x \leq 0.3$ was exceeded. By keeping the systematic uncertainty under 1% while measuring $\sigma^{pd}/2\sigma^{pp}$ from $x = 0.015$ to $x = 0.35$ allowed for the extraction of $\bar{d}(x)/\bar{u}(x)$ over this wide kinematic range. The surprising result of $\bar{d}(x)/\bar{u}(x)$ decreasing above $x = 0.2$ has instigated several new global fits.

Finally, as discussed in the previous section, this measurement has motivated plans for a further experiment to continue the study of this interaction. These results clearly demonstrate the importance of this measurement, which went well beyond initial expectations for this experiment.

Bibliography

- [1] The New Muon Collaboration, P. Amaudruz *et al.*, Phys. Rev. Lett. **66**, 2712 (1991); M. Arneodo *et al.*, Phys. Rev. D **50**, R1 (1994).
- [2] K. Gottfried, Phys. Rev. Lett. **18**, 1174 (1967).
- [3] The E665 Collaboration, M. R. Adams *et al.*, Phys. Rev. Lett. **75**, 1466 (1995).
- [4] W. Melnitchouk and A. W. Thomas, Phys. Rev. D **47**, 3783 (1993).
- [5] J. Zhao *et al.*, Phys. Rev. C **57**, 2126 (1998).
- [6] G. A. Miller, B. M. K. Nefkens, and I. Slaus, Phys. Rep. **194**, 1 (1990).
- [7] C. Boros, J. T. Londergan, and A. W. Thomas, Phys. Rev. Lett. **81**, 4075 (1998).
- [8] P. L. McGaughey, J. M. Moss, and J. C. Peng, Annu. Rev. Nucl. Part. Sci. **49** (1999).
- [9] S. D. Ellis and W. J. Stirling, Phys. Lett. B **256**, 258 (1991).
- [10] S. D. Drell and T. M. Yan, Phys. Rev. Lett. **25**, 316 (1970).
- [11] C. Grosso-Pilcher and M.J. Shochet, Ann. Rev. Nucl. Part. Sci. **36**, 1 (1986).

- [12] The NA51 Collaboration, A. Baldit *et al.*, Phys. Lett. B **332**, 244 (1994).
- [13] The E772 Collaboration, D. M. Alde *et al.*, Phys. Rev. Lett. **64**, 2479 (1990).
- [14] The E772 Collaboration, P. L. McGaughey *et al.*, Phys. Rev. Lett. **69**, 1726 (1992).
- [15] H. L. Lai, J. Huston, S. Kuhlmann, F. Olness, J. Owens, D. Soper, W. K. Tung, and H. Weerts, Phys. Rev. D **55**, 1280 (1997).
- [16] A. D. Martin, R. G. Roberts, and W. J. Stirling, Phys. Lett. B **387**, 419 (1996).
- [17] A. D. Martin, R. G. Roberts, and W. J. Stirling, Phys. Rev. D **47**, 867 (1993).
- [18] The E605 Collaboration, G. Moreno *et al.*, Phys. Rev. D **43**, 2815 (1991).
- [19] C. N. Brown, "SEM6 Calibration Memo", E866 Memorandum, 19 September 1997 (unpublished).
- [20] C. A. Gagliardi, E. A. Hawker, R. E. Tribble, D. D. Koetke, P. M. Nord, P. L. McGaughey, and C. N. Brown, Nucl. Instrum. Methods, A **418** 322 (1998).
- [21] E. A. Hawker, Ph.D. Thesis, Chapter 2, Texas A&M University, 1998.
- [22] D. M. Kaplan, "Introduction to the E605 Readout System", E605 Memorandum, 10 August 1982 (unpublished).
- [23] T. H. Chang, Ph.D. Thesis, Chapter 2, New Mexico State University, 1999.

- [24] CN/ASD Group. *PAW users guide, nProgram Library Q121*. CERN, 1995.
- [25] H. M. Roder, G. E. Childs, R. D. McCarty, and P. E. Angerhofer, *Survey of the Properties of the Hydrogen Isotopes Below their Critical Temperatures*, National Bureau of Standards Technical Note 641 (1973).
- [26] D. F. Geesaman, "Interaction Correction to Beam Flux", E866 Memorandum, 19 November 1997 (unpublished).
- [27] The FNAL E866/NuSea Collaboration, E. A. Hawker *et al.*, Phys. Rev. Lett. **80**, 3715 (1998).
- [28] A. D. Martin, R. G. Roberts, W. J. Stirling, and R. S. Thorne, Eur. Phys. J. C **4**, 463 (1998).
- [29] The HERMES Collaboration, K. Ackerstaff *et al.*, Phys. Rev. Lett. **81**, 5519 (1998).
- [30] R. D. Field and R. P. Feynman, Phys. Rev. D **15**, 2590 (1977).
- [31] D. A. Ross and C. T. Sachrajda, Nucl. Phys. B **149**, 497 (1979).
- [32] F. M. Steffens and A. W. Thomas, Phys. Rev. C **55**, 900 (1997).
- [33] S. Kumano, Phys. Rev. D **43**, 3067 (1991); **43**, 59 (1991); S. Kumano and J. T. Londergan, *ibid.* **44**, 717 (1991).
- [34] The FNAL E866/NuSea Collaboration, J. C. Peng *et al.*, Phys. Rev. D **58**, 092004 (1998).
- [35] P. J. Sutton, A. D. Martin, R. G. Roberts and W. J. Stirling, Phys. Rev. D **45**, 2349 (1992).

- [36] A. Szczurek, J. Speth and G. T. Garvey, Nucl. Phys. A **570**, 765 (1994).
- [37] P. Stoler, Phys. Rep. **226**, 103 (1993).
- [38] E. J. Eichten, I. Hinchliffe and C. Quigg, Phys. Rev. D **45**, 2269 (1992);
47, R747 (1993).
- [39] A. Szczurek, A. J. Buchmann, and A. Faessler, J. Phys. G: Nucl. Part.
Phys. **22**, 1741 (1996).
- [40] A. E. Dorokhov and N. I. Kochelev, Phys. Rev. Lett. B **259**, 335 (1991);
304, 167 (1993).
- [41] W. Melnitchouk, J. Speth, A. W. Thomas, Phys. Rev. D **59**, 014033
(1998).
- [42] The P906 Collaboration, D. F. Geesaman (spokesman) *et al.*, Fermi Na-
tional Accelerator Laboratory Proposal 906, 1999 (unpublished).

Vita

Rusty Shane Towell was born in Indio, California on April 1, 1969, the son of Delbert Clayton Towell and Helen Fay Towell. After graduating from Abilene High School in 1986, he entered Abilene Christian University in Abilene, Texas. He received the degree of Bachelor of Science from Abilene Christian University in May 1990. During the following years he was an officer in the United States Navy where he taught at the Naval Nuclear Power School in Orlando, Florida. In September 1994 he entered the Graduate School of The University of Texas at Austin.

Permanent address: Rt. 4 Box 155 A
Brownwood, TX 76801

This dissertation was typeset with L^AT_EX[†] by the author.

[†]L^AT_EX is a document preparation system developed by Leslie Lamport as a special version of Donald Knuth's T_EX Program.